Building a STIRAP Laser for Opposite Parity States in Dysprosium

A master's thesis submitted to the

Faculty of Mathematics, Computer Science and Physics

of the

Leopold-Franzens University of Innsbruck

in partial fulfilment of the requirements for the degree of

Master of Science
(MSc.)

presented by

Michael Obertegger

supervised by

Univ.-Prof. Dr. Rudolf Grimm
and Dr. Emil Kirilov

carried out at the

the Institute for Experimental Physics in the Ultracold
Quantum Matter group

October 2020

Eidesstattliche Erklärung

Ich erkläre hiermit an Eides statt durch meine eigenständige Unterschrift, dass ich die vorliegende Arbeit selbstständig verfasst und keine anderen als die angegebenen Quellen und Hilfsmittel verwendet habe. Alle Stellen, die wörtlich oder inhaltlich den angegebenen Quellen entnommen wurden, sind als solche kenntlich gemacht.

Die vorliegende Arbeit wurde bisher in gleicher oder ähnlicher Form noch nicht als Magister-/Master-/Diplomarbeit/Dissertation eingereicht.

Datum	Unterschrift

Abstract

This master thesis contains a description and a characterisation of a laser setup with a final wavelength of 418.6 nm and a pulse duration in the sub-hundred nanosecond range. The setup is part of a STIRAP laser setup which is used to populate opposite parity states in Dysprosium. This is a novel approach in producing an ultracold gas of Dysprosium atoms with both a strong magnetic and electric dipole moment. An external cavity diode laser in cat's eye design with a wavelength centered around 840 nm acts as a light source. The desired wavelength can be adjusted by means of an interference filter inside the external cavity. A tapered amplifier is used to amplify the optical power for optimizing the second harmonic generation process in an enhancement cavity of bow-tie geometry. An acousto optic modulator in a double pass configuration generates short pulses by switching a RF-driver on and off. The setup has proven to be able to produce a laser beam of approximately 3 mW which is almost twice the power needed. The rise time of the pulses has been measured to be about 30 ns and should be fast enough.

Kurzfassung

Diese Masterarbeit beinhaltet eine Beschreibung sowie eine Charakterisierung eines Laser Aufbaus mit einer Wellenlänge von 418.6 nm und einer Pulsdauer im Bereich von unter 100 ns. Der Erzeugte Laser ist Teil eines STIRAP Prozesses zur Besetzung von Zuständen mit entgegengesetzter Parität in Dysprosium. Dies ist eine neuartige Methode zur Herstellung eines ultrakalten dipolaren Quantengases aus Dysprosium-Atomen mit sowohl magnetischen als auch elektrischen dipolmoment. Als Lichtquelle dient ein Diodenlaser mit externem Resonator bei einer Wellenlänge von 840 nm. Mit Hilfe eines drehbaren Interferenzfilters, welcher sich im Resonator befindet kann die emittierte Wellenlänge angepasst werden. Ein Trapezverstärker wird eingesetzt um die optische Leistung zu verstärkten und den drauf folgenden Frequenzverdoppelungs Prozess zu optimieren. Die Frequenzverdoppelung wird mit Hilfe eines nichtlinearen Kristalls welcher sich in einem Ringresonator befindet durchgeführt. Ein Akusto-optischer Modulator in der sogenannten double-pass Konfiguration, erlaubt es durch Ein- und Aus-schalten des RF-Verstärkers kurze Laser-Pulse zu erzeugen. Der Aufbau zeigte sich geeignet zur Erzeugung eines Laserspulses mit einer Spitzenleistung von etwa 3 mW und einer Anstiegszeit von 30 ns. Die erzielte Leistung ist etwa doppelt so groß wie notwending und die Anstiegszeit reicht aus um Pulse von unter 100 ns zu erzeugen.

Contents

1. Introduction

1.1. Motivation

During the last 25 years, since the first realization of Bose Einstein condensates (BEC) and the following realization of degenerate Fermi gases, an increasing attention in the field of ultracold gases took place. These days, cold atoms in the tens of nanokelvin range can be realized by combined laser- and evaporative-cooling techniques. There is special interest in the production of so-called dipolar quantum gases, because such systems can be controlled by means of external fields and are excellent candidates for observing novel physics [1]. Of the 13 elements condensated to a BEC, there are Chromium (Cr), Erbium (Er) and Dysprosium (Dy) which are available for dipolar physics. The first BEC, where dipolar effects could be observed, was realized in 2005 [2]. This was followed by the first realizations of this type of quantum gases with Dysprosium [3] and Erbium [4]. However, dipolar effects can also be observed in systems which posses an electric dipole moment.
A possible approach to produce an ultracold gas of atoms, possessing both strong magnetic and electric dipole moments, can be realized with Dy atoms. This is possible because of the existence of almost degenerate opposite parity states (termed opposite parity doublet OPD). The nearly degeneracy of such states makes it possible to achieve strong mixing with moderate and experimentally accessible electric field strengths. Such a OPD is existing for Dy at $19\,797.96\,\mathrm{cm}^{-1}$ with lifetimes in the μs range and a reduced dipole moment on the order of $0.01\,\mathrm{a\,u}$. Two years ago, another OPD in Dy, positioned at $17\,513.33\,\mathrm{cm}^{-1}$ and $17\,514.50\,\mathrm{cm}^{-1}$ and with electronic angular momentum J = 10 and J = 9 respectively, was predicted theoretically [5]. The states, labelled with $|a\rangle$ and $|b\rangle$ have estimated decay rates of $\gamma_\mathrm{a} = 3.5 \times 10^{-2}\,\mathrm{s}^{-1}$ and $\gamma_\mathrm{b} = 3 \times 10^{4}\,\mathrm{s}^{-1}$ respectively, and a reduced dipole moment of $\langle a|\,|\hat{d}|\,|b\rangle \approx 3.2\,\mathrm{a\,u}$. Therefore, this OPD is a promising candidate for dipolar physics. For an experimentally accessible electric field of $5\,\mathrm{kV/cm}$ and an magnetic field of $100\,\mathrm{G}$, a permanent magnetic dipole moment (PMDM) of $\mu^* = 13\,\mu_\mathrm{B}$ and an induced electric dipole moment (IEDM) of $d^* = 0.22\,\mathrm{D}$ is predicted [5].

A promising way to populate the OPD is by using a Stimulated Raman Adiabatic Passage (STIRAP). The ground state in ^{164}Dy is of even parity and configuration [Xe]4f^{10}6s^2(5I) with total angular momentum of J = 8. In order to reach the $|b\rangle$ state, an intermediate state with good coupling to ground and final state is needed. Such an intermediate level could be the state at $23\,877.75\,\mathrm{cm}^{-1}$ with J = 8, and configuration [Xe]4f^{10}6s6p(8; 1)°. To address this specific state from the ground state a laser with a wavelength of $\lambda_1 = 418.6\,\text{nm}$ is needed which has to be developed first. For the second branch, which corresponds to the transition from the intermediate state to state $|a\rangle$ at $17\,513.33\,\text{cm}^{-1}$, a fiber laser system with an output wavelength of $\lambda_2 = 1571\,\text{nm}$ is used. The Once the STIRAP populates the state $|b\rangle$, which requires the two lasers to be in σ^+ and π configuration, a π-microwave-pulse is applied to mix the states with opposite parity. Figure 1.1 shows the energy level diagram of ^{164}Dy.

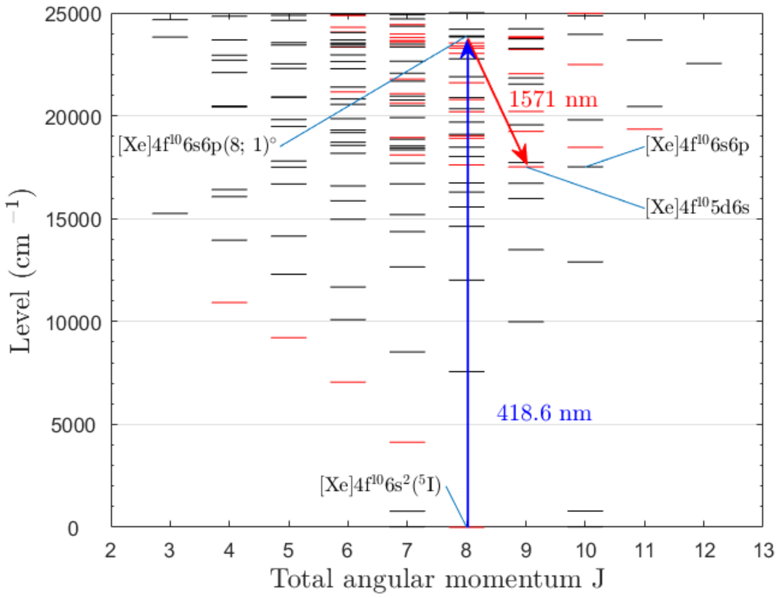

Figure 1.1.: Energy level diagram of ^{164}Dy up to $25\,000\,\text{cm}^{-1}$. Even (odd) parity levels are shown in red (black). Blue arrow indicates the transition from the ground state to the intermediate state and the red arrow from the intermediate state to the final state in a STIRAP process. Energy levels taken from [6] and [5].

1.2. Goals and how to achieve them

To address the $|b\rangle$ state at $17\,514.50\,\text{cm}^{-1}$ in a STIRAP process using the state at 23 877.75 as an intermediate state, a laser with a wavelength of $\lambda = 418.6\,\text{nm}$ is needed. The intermediate state has a lifetime of $\gamma = 7.9\,\text{ns}$ [7]. This requires that the laser pulses, which are needed for STIRAP, have to be very short in order to realize a high transfer efficiency. In this section here, it is tried to give a simple estimation of how much power is needed for the blue branch of the STIRAP transition.
To quantify how much power is needed, we need a quantity that describes how well an atom is able to absorb or emit electromagnetic radiation for a specific transition and then connect it to the laser intensity. This quantity is the so called transition dipole moment d which is incorporated in the Rabi frequency Ω which reads

$$\Omega = \frac{dE}{\hbar} \tag{1.1}$$

where E is the electric field amplitude and $\hbar$ the reduced Planck constant. In general d is a complex vector operator, but for the sake of simplicity we neglect both, the vector and operator aspect. By using the well known expression $I = \frac{1}{2}\epsilon_0 c E^2$, inserting it into (1.1) and rearranging for the intensity one obtains

$$I = \frac{\epsilon_0 c \hbar^2 \Omega^2}{2d^2}. \tag{1.2}$$

The constants ϵ_0 and c are the permittivity of free space and the speed of light, respectively. As explained in section 2.1.3, for an adiabatic evolution $\Omega_{\mathrm{max}} T > A_{\mathrm{min}}$ has to be fulfilled. Ω_{max} denotes the peak Rabi frequency, T the pulse duration and A_{min} some minimum pulse area. For most STIRAP applications $\mathcal{A}_{\mathrm{min}} \gtrsim 3\pi \approx 10$ has proved to be enough in order to achieve good transfer efficiencies. Therefore, the peak intensity becomes

$$I_{\mathrm{peak}} = \frac{100\epsilon_0 c \hbar}{2d^2 T^2}. \tag{1.3}$$

The next step is to determine the transition dipole moment d. From quantum optics, one finds that the radiative decay rate Γ is connected with d according to

$$\Gamma = \frac{d^2 \omega^3}{3\pi\epsilon_0 \hbar c^3}. \tag{1.4}$$

In equation (1.4) ω corresponds to the frequency associated with the transition. By using $\gamma = \frac{1}{\Gamma}$ and $c = \frac{\lambda\omega}{2\pi}$ equation (1.3) can be solved to obtain an expression for d^2

$$d^2 = \frac{3\epsilon_0 h \lambda^3}{2(2\pi)^3 \gamma}. \tag{1.5}$$

By inserting all the known values into equation (1.5), this gives $d^2 = 3.296 \times 10^{-58}\,\mathrm{C^2m^2}$. By plugging this value, and a pulse duration of $T = 50\,\mathrm{ns}$ into equation (1.3), a needed intensity of $I_{\mathrm{peak}} = 1791\,\mathrm{W/m^2}$ is obtained. Assuming a reasonable diameter of the laser beam of $D = 1\,\mathrm{mm}$, a peak power of $P_{\mathrm{peak}} = 1.407\,\mathrm{mW}$ is needed.
The aim of this master thesis is therefore, to build a laser with wavelength $\lambda = 418.6\,\mathrm{nm}$, a puls duration T in the sub-hundred nanosecond range and corresponding peak power of at least $P_{\mathrm{peak}} = 1.407\,\mathrm{mW}$. To achieve this, the setup consists of four main parts. An external cavity diode laser in cat's eye design with a wavelength centered around 840 nm is acting as a light source. A build in interference filter can be used to adjust the desired wavelength by tilting it. Next, a tapered amplifier is then used to amplify the optical power as much as possible. This is needed to achieve reasonable powers in a second harmonic generation process. A bow-tie cavity with a nonlinear crystal is the part of the setup where the blue light at $\lambda = 418.6\,\mathrm{nm}$ is produced. To generate a pulse from a continuous wave laser a double-pass AOM is realized as a last part of the setup. The design of the external cavity diode laser, the tapered amplifier setup and the doubling cavity is by Emil Kirilov.

2. Introduction to STIRAP

A Raman process typically involves a three-state quantum system and it's scope is to transfer population among two of these states. The initial population is changed via two-photon transitions into a final state that normally cannot be reached by electric dipole radiation. In the traditional Raman process, radiative excitation by a pump laser field is followed by spontaneous emission (Stokes field). Due to spontaneous emission many final states are addressed, and hence such a process is not very selective. By using a second laser field, and therefore replacing spontaneous by stimulated emission, the process can be made more selective. Due to the fact that in this situation both fields are under experimental control, such a process is often called stimulated Raman scattering (SRS). One might think that a intuitive pulse sequence, pump field before Stokes field is the right way to implement a successful population transfer. However, this kind of pulse ordering suffers from spontaneous emission due to the fact that a lossy intermediate state is populated. In a so called counterintuitive pulse sequence, it is possible to transfer all of the population from an initial to a target state, without never populating the intermediate state. Such a process is called stimulated Raman adiabatic passage (STIRAP) [8].

STIRAP was initially developed to study the chemical dynamics of molecules and the original paper [9] dates back to 1990. Within the last 30 years STIRAP found applications not only in chemistry and physics, but also in engineering and information processing. As an example in physics, STIRAP is used in the formation of ultracold molecules where they are "STIRAPed "into the rovibronic ground state. Another example arises in probing physics beyond the standard model. To measure the electrons electric dipole moment, STIRAP is used to transfer the population of thorium monoxide in a suitable molecular state [10]. In this experiment, STIRAP will be used to transfer the population from the ^{164}Dy ground state via an intermediate state into the opposite parity state at $17\,514.50\,\mathrm{cm}^{-1}$, and afterwards to produce simultaneously a magnetic and electric dipolar gas of ultracold dysprosium atoms.

This section gives a short introduction into the mechanism of STIRAP. An insight into the most important equations is given to illuminate the special features of the process. Therefore, the chapter relies mostly on papers written by N.V. Vitanov and K. Bergmann which are [10], [11], [12], and [13]. Additional information is taken from [14] and [15].

2.1. Basic Equations and Definitions

STIRAP provides a (nearly) complete and robust method to transfer population efficiently and selectively between two quantum states lying in a three-state quantum system. To transfer atoms, that are initially populated in a state $|\Psi_1\rangle$, to a (not populated) target state $|\Psi_3\rangle$, two pulsed electromagnetic fields are needed. The pump pulse and the Stokes pulse couple an intermediate state $|\Psi_2\rangle$ with $|\Psi_1\rangle$ and $|\Psi_3\rangle$, respectively. This situation is shown in figure 2.1

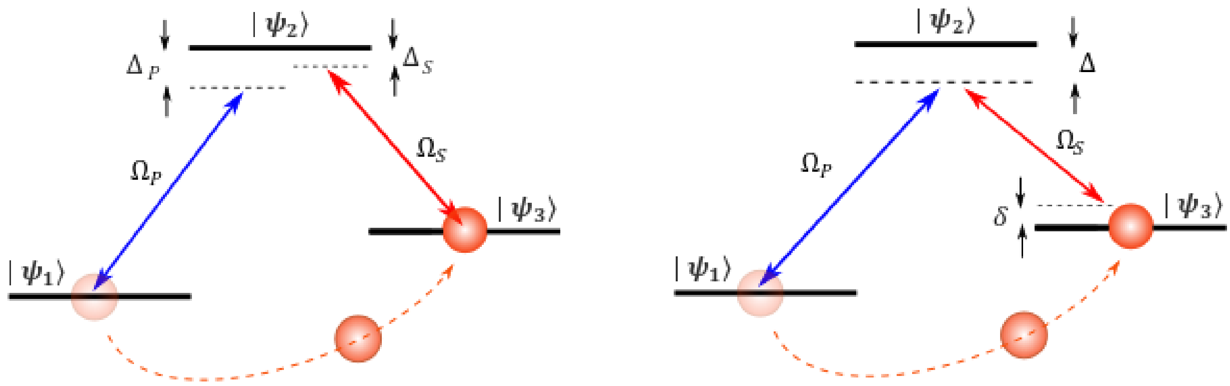

Figure 2.1.: STIRAP coupling scheme. The pump pulse with Rabi frequency $\Omega_P(t)$ couples the states $|\Psi_1\rangle$ and $|\Psi_2\rangle$. The Stokes pulse with Rabi frequency $\Omega_S(t)$ couples the states $|\Psi_3\rangle$ and $|\Psi_2\rangle$. Left plot: Δ_P and Δ_S are the Rabi frequencies of the corresponding pulses. Right plot: both pulses are detuned by Δ from resonance and δ is called the two-photon detuning. After the STIRAP process is completed, the atom is transferred from state $|\Psi_1\rangle$ to the state $|\Psi_3\rangle$, never populating state $|\Psi_2\rangle$.

Figure 2.1 shows the so called Λ system. Other three state systems like a $V-$ or a ladder-system are possible, but not needed here. The time evolution of a laser driven three-level system is given by the time dependent Schrödinger equation

$$i\hbar\frac{d}{dt}\mathbf{c}(t) = \mathbf{H}(t)\mathbf{c}(t) \tag{2.1}$$

where $\mathbf{c}(t) = [c_1(t), c_2(t), c_3(t)]^T$ is a column vector containing the probability amplitudes of the bare (or diabatic states) $|\Psi_1\rangle$, $|\Psi_2\rangle$ and $|\Psi_3\rangle$. Within the rotating wave approximation (RWA) the STIRAP Hamiltonian reads [14]

$$\mathbf{H}(t) = \hbar \begin{bmatrix} 0 & \frac{1}{2}\Omega_P(t) & 0 \\ \frac{1}{2}\Omega_P(t) & \Delta_P - i\Gamma/2 & \frac{1}{2}\Omega_S(t) \\ 0 & \frac{1}{2}\Omega_S(t) & \Delta_P - \Delta_S \end{bmatrix}, \tag{2.2}$$

where $\Omega_P(t) = -\mathbf{d}_{12}\cdot\mathbf{E}_P/\hbar$ and $\Omega_S(t) = -\mathbf{d}_{32}\cdot\mathbf{E}_S/\hbar$ correspond to the Rabi frequencies of the pump and Stokes pulse, respectively. The Rabi frequencies represent the coupling strengths. The detunings Δ_P and Δ_S correspond to the detunings of the pump and Stoke pulse to the intermediate state. This situation corresponds to the left plot of figure 2.1. The parameter Γ is the spontaneous decay rate from the intermediate state $|\Psi_2\rangle$ to other states than $|\Psi_1\rangle$ and $|\Psi_3\rangle$. By defining the single photon detuning $\Delta \equiv \Delta_P$ and the two-photon detuning $\delta = \Delta_P - \Delta_S$ the situation can be transformed to that corresponding to the right plot of figure 2.1. In the following, $\Gamma = 0$ and $\delta = 0$. The requirement of $\delta = 0$ is known as **two-photon resonance** and is crucial to achieve high efficiencies.

2.1.1. Eigenstates and Adiabatic Basis

The instantaneous eigenstates of the Hamiltonian of $\mathbf{H}(\mathrm{t})$ are linear superpositions of the unperturbed (bare) states $|\Psi_1\rangle$, $|\Psi_2\rangle$ and $|\Psi_3\rangle$ and read

$$\begin{aligned}
|\Phi_+(t)\rangle &= \sin\theta(t)\sin\phi(t)\,|\Psi_1\rangle + \cos\theta(t)\,|\Psi_2\rangle + \cos\theta(t)\sin\phi(t)\,|\Psi_3\rangle \\
|\Phi_0(t)\rangle &= \cos\theta(t)\,|\Psi_1\rangle - \sin\theta(t)\,|\Psi_3\rangle \\
|\Phi_-(t)\rangle &= \sin\theta(t)\cos\phi(t)\,|\Psi_1\rangle - \sin\theta(t)\,|\Psi_2\rangle + \cos\theta(t)\cos\phi(t)\,|\Psi_3\rangle
\end{aligned} \tag{2.3}$$

where we have defined the mixing angles $\theta(t)$ and $\phi(t)$ which are giving the ratio of the coupling strengths and of the coupling strength and detuning. They are defined as

$$\tan\theta(t) = \frac{\Omega_P(t)}{\Omega_S(t)} \quad \text{and} \quad \tan 2\phi(t) = \frac{\Omega(t)}{\Delta(t)} \tag{2.4}$$

where $\Omega(t) = \sqrt{\Omega_P(t)^2 + \Omega_S(t)^2}$, sometimes also denoted as $\Omega_{\mathrm{rms}}(t)$ (root mean square Rabi frequency) [15]. The eigenvalues of the STIRAP Hamiltonian (2.2), also called adiabatic energies, are

$$\begin{aligned}
\hbar\epsilon_+ &= \frac{\hbar}{2}\Omega(t)\cot\phi(t) \\
\hbar\epsilon_0 &= 0 \\
\hbar\epsilon_- &= \frac{\hbar}{2}\Omega(t)\tan\phi(t)
\end{aligned} \tag{2.5}$$

STIRAP relies on the so called dark (or population trapping) state $|\Phi_0(t)\rangle$ of equation (2.3). This state is a coherent superposition of states $|\Psi_1\rangle$ and $|\Psi_3\rangle$ and does not depend on state $|\Psi_2\rangle$. If it is possible to stay in this state during the whole transfer process, then all the population can be transferred from $|\Psi_1\rangle$ to $|\Psi_3\rangle$ [11].

2.1.2. Schrödinger Equation in the Adiabatic representation

The eigenvectors (2.3) form an orthogonal ($\mathbf{W}^{-1} = \mathbf{W}^T$) rotation matrix

$$\mathbf{W} = \begin{bmatrix} \sin\theta\sin\phi & \cos\theta & \sin\theta\cos\phi \\ \cos\phi & 0 & -\sin\phi \\ \cos\phi\sin\phi & -\sin\phi & \cos\theta\cos\phi \end{bmatrix} \tag{2.6}$$

which connects the probability amplitudes of the adiabatic states $\mathbf{a}(t) = [a_1(t), a_2(t), a_3(t)]^T$ to the bare (or diabatic) amplitudes $\mathbf{c}(t)$ by the orthogonal transformation

$$\mathbf{c}(t) = \mathbf{W}\mathbf{a}(t) \tag{2.7}$$

where the time dependence of $\mathbf{W}$ was omitted. By inserting equation (2.7) into equation (2.1), one obtains

$$i\hbar\frac{d}{dt}\mathbf{a}(t) = \mathbf{H}_a(t)\mathbf{a}(t) \tag{2.8}$$

where the Hamiltonian is given by $\mathbf{H}_a(t) = \mathbf{W}^{-1}\mathbf{H}\mathbf{W} - i\hbar\mathbf{W}^{-1}\dot{\mathbf{W}}$. Equation (2.8) is the Schrödinger equation in the adiabatic basis. The explicit form of $\mathbf{H}_a(t)$ reads

$$\mathbf{H}_a = \hbar \begin{bmatrix} \frac{1}{2}\Omega\cot\phi & i\dot{\theta}\sin\phi & i\dot{\phi} \\ -i\dot{\theta}\sin\phi & 0 & -i\dot{\theta}\cos\phi \\ -i\dot{\phi} & i\dot{\theta}\cos\phi & -\frac{1}{2}\Omega\tan\phi \end{bmatrix}. \tag{2.9}$$

The diagonal elements of the above matrix correspond exactly to the eigenvalues of the STIRAP Hamiltonian given by (2.5). The off-diagonal elements correspond to non-adiabatic couplings which will induce transitions between the adiabatic eigenstates given by (2.3). To achieve a (nearly) complete population transfer, these off-diagonal elements have to be reduced to very small values. In this case, the system can be forced to stay approximately in the dark state for all times.

2.1.3. Local and Global Adiabatic Condition

To guarantee nearly complete population transfere from state $|\Psi_1\rangle$ to state $|\Psi_3\rangle$ the off-diagonal elements of the Hamiltonian given by (2.9) have to be small compared to the separation of the diagonal elements (differences of the eigenvalues). The derivatives of the mixing angles (2.4) are given by

$$\begin{aligned} \dot{\phi} &= \frac{\Omega(t)\dot{\Delta}(t) - \Delta(t)\dot{\Omega}(t)}{\Omega^2(t) + \Delta^2(t)} \\ \dot{\theta} &= \frac{\Omega_S(t)\dot{\Omega}_P(t) - \Omega_P(t)\dot{\Omega}_S(t)}{\Omega_S(t)^2 + \Omega_P^2(t)} \end{aligned}. \tag{2.10}$$

The single photon detuning Δ is usually very small and ideally equal to zero. Therefore, $\dot{\phi}$ is typically a small number. Hence, the crucial derivative for high transfer efficiencies is $\dot{\theta}$. Dividing the eigenenergies (2.3) by $\hbar$ one obtaines the corresponding eigenfrequencies.

The differences between the eigenfrequencies has to be much larger than $\dot{\theta}$ which gives the following condition

$$|\omega_{\pm} - \omega_0| = \frac{1}{2}\sqrt{\Omega_S(t)^2 + \Omega_P^2(t)} \gg |\dot{\theta}|. \tag{2.11}$$

The above expression is exactly true for $\Delta = 0$. This condition quantifies the smoothness of the laser pulses and must hold for any time during the transfer process. Hence, it is called **local adiabatic condition**. If the condition (2.11) is fulfilled, then nonadiabatic couplings between the state $|\Phi_0(t)\rangle$ and states $|\Phi_+(t)\rangle$ and $|\Phi_-(t)\rangle$ are small. As a consequence, the STIRAP process is insensitive to small variations in laser intensity, pulse duration and pulse delay [16].
A global criterion can be derived by integrating equation (2.11) over time. The pulse root mean square area is then given by

$$\mathcal{A} = \int_{-\infty}^{\infty} \Omega_{rms}(t)dt = \int_{-\infty}^{\infty} \sqrt{\Omega_P(t)^2 + \Omega_S(t)^2}dt. \tag{2.12}$$

The integral over $\dot{\theta}$ from equation (2.10) gives exactly $\pi/2$, and therefore the inequality

$$\mathcal{A} \gg \pi/2 \tag{2.13}$$

holds. Equation (2.13) can be viewed as a global condition for adiabatic population transfer. Due to the fact that $\mathcal{A} \propto \Omega_{\max}T$, where $\Omega_{\max}$ is the peak Rabi frequency and T the pulse duration, equation (2.13) can be rewritten as

$$\Omega_{\max}T > \mathcal{A}_{\min} \tag{2.14}$$

where $\mathcal{A}_{\min}$ is some minimum pulse area which depends on pulse shape and required transfer efficiency. For most STIRAP applications, pulse areas of $\mathcal{A}_{\min} \gtrsim 3\pi$ have provided sufficient population transfer [13].

2.2. STIRAP Mechanism

In this section the STIRAP mechanism is explained in a more illustrative way. For this purpose, the process is divided in three steps. For a successful population transfer a counterintuitive pulse ordering is needed. To guarantee adabatic evolution, a suitable overlap of the pulses must be present. Furthermore, we require that the detuning $\Delta = 0$ remains constant for the whole transfer. Figure 2.2 shows the most important characteristics of a STIRAP process. For the STIRAP pulses we assume a Gaussian shape

$$\Omega_P(t) = \Omega_0 e^{-(t-\tau/2)^2/T^2} \text{ and } \Omega_S(t) = \Omega_0 e^{-(t+\tau/2)^2/T^2}, \tag{2.15}$$

with characteristic width T, peak Rabi frequency Ω_0 and pulse delay τ. In the following, the different stages of the STIRAP mechanism are discussed.

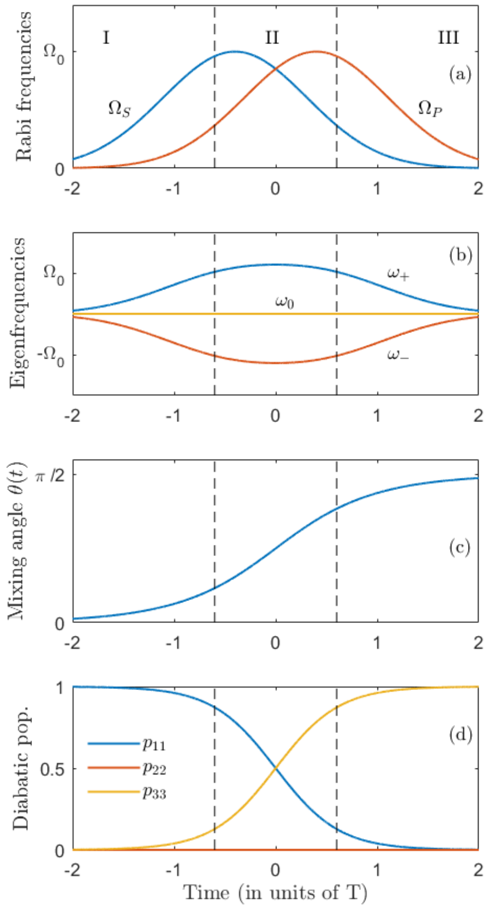

Figure 2.2.: Example of STIRAP induced by Gaussian pulses: (a) time evolution of the pulses, (b) adiabatic eigenvalues ,(c) mixing angle and (e) the diabatic populations. The following parameters are used for plotting: $\gamma_{13} = 2T^{-}1$, $\Omega_0 = 50T^{-}1$, and $\tau = 0.8T$. Figure adapted from [13].

Plot (a) shows the Gaussian pulses of equation (2.15) in an counterintuitive order.
Stage I: Over a great range only of this first step, only the Stokes pulse is present which couples the states Ψ_2 and Ψ_3. Plot (b) shows the so called Autler-Townes splitting of the adiabatic energy levels. The dark eigenvector Φ_0 of equation (2.3) is equal to Ψ_1 and the population remains unchanged as can be seen in plot (d).
Stage II: In this second step both pulses are present. The pump pulse is decreasing while the Stokes pulse increases. According to equation (2.4) this causes the mixing angle θ approaching $\pi/2$ as indicated in plot c. State Φ_0 departs from Ψ_1 to $-\Psi_3$ and a population transfer starts taking place.
Stage III: During the last stage the Stokes pulse vanishes and only the pump pulse is present. The mixing angle θ is now equal to $\pi/2$ and all of the population has been transferred from the initial state Ψ_1 to the target state Ψ_3 [13] [11].
It should be noted, that in this very simplified picture of STIRAP, is only valid if dephasing processes are completely neglected. For more detailed explanations consider [8], [13] or [15].
Another important condition for a successive population transfer should be briefly mentioned. As already explained in section 2.1.2, the off-diagonal matrix elements of (2.9) have to be small compared to the differences of the diagonal matrix elements. These diagonal matrix elements correspond exactly to the eigenvalues in plot (b) of figure 2.2. It happens that these off-diagonal elements take only considerable values when the splitting of the eigenfrequencies is biggest. Therefore, this splitting is one of the striking characteristics of STIRAP that enables a successful population transfer.

2.3. STIRAP with Spontaneous Emission

Real physical systems are never perfect and various decoherence effects, such as phase relaxation dephasing and population losses due to spontaneous emission will decrease the transfer efficiency in a STIRAP process. In the Λ system exploit in this experiment, the decay rate of the used intermediate state at $23\,877.75\,\mathrm{cm}^{-1}$ to the Dysprosium ground state is much larger than two the opposite parity state at $17\,514.50\,\mathrm{cm}^{-1}$. Therefore, the effect of unequal spontaneous decay rates from the intermediate state to the initial and target state has to be considered. Because the derivations are very lengthy, only the most important results for this thesis are summarized in this section. For more detailed information consider [11] and [12].

2.3.1. Bright-Excited-Dark Basis

To treat the problem of spontaneous decay within the system it is convenient to work in a basis composed of the dark state $|d(t)\rangle$, the bright state $|b(t)\rangle$ and the excited state $|e\rangle$,

$$\begin{aligned} |b(t)\rangle &= \sin\theta(t)\,|\Psi_1\rangle + \cos\theta(t)\,|\Psi_3\rangle \\ |e\rangle &= |\Psi_2\rangle \\ |d(t)\rangle &= \cos\theta(t)\,|\Psi_1\rangle - \sin\theta(t)\,|\Psi_3\rangle \end{aligned} \tag{2.16}$$

where $\theta(t)$ is the mixing angle defined in equation (2.4). The presence of the dark state $|d(t)\rangle$ is justified by the fact that it is the state where the population resides for the whole process in the adiabatic limit. For this particular problem, the special role of state $|e\rangle$ is that it's the only decaying state. The adiabatic basis states on the other hand are superpositions of all three basis states (beside the dark state) and hence they involve decaying and stable states which makes the problem more complicated. The bright state $|b(t)\rangle$ is determined by the two other states uniquely. The vectors (2.16) form a similar rotation matrix like the one obtained from the adiabatic basis vectors. For the bright-excited-dark basis the rotation matrix $\mathbf{R}$ reads [12]

$$\mathbf{R} = \begin{bmatrix} \sin\theta(t) & 0 & \cos\theta(t) \\ 0 & 1 & 0 \\ \cos\theta(t) & 0 & -\sin\theta(t) \end{bmatrix}. \tag{2.17}$$

2.3.2. Effect of Unequal Decay Rates

In the adiabatic limit the intermediate state $|\Psi_2\rangle$ remains unpopulated during the whole STIRAP process and the transfer efficiency reaches unity. In the case of a non adiabatic evolution, $|\Psi_2\rangle$ can acquire some population and spontaneous emission will lower the transfer efficiency. The dephasing process can no longer be treated by the time dependant Schrödinger equation. Such processes are treated by introducing phenomenological decay terms into the Liouville equation

$$i\hbar\frac{d\rho}{dt} = [\mathbf{H}, \rho] + \mathbf{D}, \tag{2.18}$$

where the dissipator $\mathbf{D}$ describes spontaneous emission within the system [11]. In matrix form $\mathbf{D}$ can be written as

$$\mathbf{D} = -i\frac{\hbar}{2}\begin{bmatrix} -2\Gamma_1\rho_{22} & (\Gamma_1+\Gamma_3)\rho_{12} & 0 \\ (\Gamma_1+\Gamma_3)\rho_{21} & 2(\Gamma_1+\Gamma_3)\rho_{22} & (\Gamma_1+\Gamma_3)\rho_{23} \\ 0 & (\Gamma_1+\Gamma_3)\rho_{32} & -2\Gamma_3\rho_{22} \end{bmatrix}. \tag{2.19}$$

Here $\rho_{mn} = \langle\Psi_m|\hat{\rho}|\Psi_n\rangle$, where $\hat{\rho}$ is the density operator. The decay rates Γ_1 and Γ_3 describe spontaneous emission from state $|\Psi_2\rangle$ to states $|\Psi_1\rangle$ and $|\Psi_3\rangle$, respectively. Initially, the system is in state $|\Psi_1\rangle$ and hence equation (2.18) is solved for $\rho_{11}(-\infty)$ $= 1$ and $\rho_{mn}(-\infty) = 0$ for mn $\neq 11$. The rotation matrix from (2.17) transforms the Liouville equation (2.18) into the bright-excited-dark basis

$$i\hbar\frac{d\tilde{\mathbf{D}}}{dt} = [\tilde{\mathbf{H}}, \tilde{\mathbf{D}}] - i\hbar[\mathbf{R}\dot{\mathbf{R}}, \tilde{\rho}] + \tilde{\mathbf{D}} \tag{2.20}$$

where $\tilde{\rho} = \mathbf{R}\rho\mathbf{R}$, $\tilde{\mathbf{H}} = \mathbf{RHR}$ and $\tilde{\mathbf{D}} = \mathbf{RDR}$. By defining the parameters $\Gamma = \Gamma_1 + \Gamma_3$ and $\gamma = \Gamma_1 - \Gamma_3$ one can derive the following two differential equations

$$\begin{aligned} \dot{v} &= -\frac{\Omega^2}{2\Gamma}v - 2\dot{\theta}w + \frac{\Omega^2\gamma\sin 2\theta}{2\Gamma^2}(w+1) \\ \dot{w} &= 2\dot{\theta}v - \frac{\Omega^2}{2\Gamma}(1 + \frac{\gamma\cos 2\theta}{\Gamma})(w+1) \end{aligned} \tag{2.21}$$

where Ω is the root mean square Rabi frequency and time dependencies have been omitted. The variables v and w are connected to the density matrix elements in the bright-excited-dark basis by $v = 2\mathrm{Re}\{\rho_{\mathrm{bd}}\}$ and $w = \rho_{bb} - \rho_{dd}$. With the additional requirement that $\rho_{bb}(t) + \rho_{dd}(t) \approx 1$, equations (2.21) can be solved numerically. In order to transform from the bright-excited-dark basis back to the original basis the relation $\tilde{\rho} = R\rho R$. For the initial and final state populations one gets [12]

$$\begin{aligned} \rho_{11}(t) &= \rho_{bb}(t)\sin^2\theta(t) + \rho_{dd}(t)\cos^2\theta(t) + \mathrm{Re}\{\rho_{\mathrm{bd}}\}\sin 2\theta \\ \rho_{33}(t) &= \rho_{bb}(t)\cos^2\theta(t) + \rho_{dd}(t)\sin^2\theta(t) - \mathrm{Re}\{\rho_{\mathrm{bd}}\}\sin 2\theta. \end{aligned} \tag{2.22}$$

Numerical integration of (2.21) leads to figure 2.3 which shows the effect of unequal decay rates. Due to the fact that the difference of the decay rates γ can be positive ($\Gamma_1 > \Gamma_3$) or negative ($\Gamma_3 > \Gamma_1$), the solution of (2.21) is not symmetric with respect to γ. The left plot of figure 2.3 shows an example of how the populations evolve as a function of time. The right plot shows that the population of the target state ρ_{33} decreases as γ goes from negative to positive values. The limits in this plot correspond to $\gamma = \Gamma$ and $\gamma = -\Gamma$. One can clearly see that the latter limit is favourable in a STIRAP process, because due to $\Gamma_1 = 0$ and $\Gamma_3 = \Gamma$ spontaneous emission only occurs in the direction to the target state $|\Psi_3\rangle$. The other limit where $\Gamma_1 = \Gamma$ and $\Gamma_3 = 0$ least favourable for STIRAP. Spontaneous emission is returning the population back to state $|\Psi_1\rangle$ and hence keeping the values for ρ_{11} high and for ρ_{33} low [12].

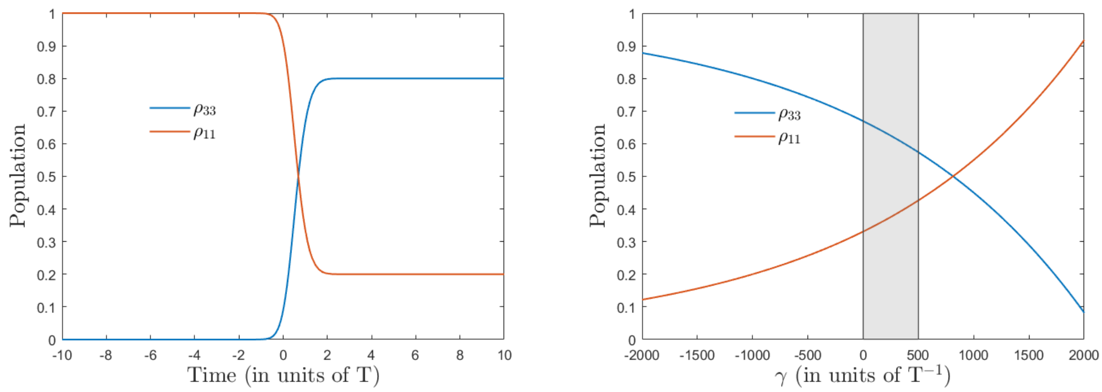

Figure 2.3.: Effect of unequal decay rates. Left plot: Evolution of the populations as a function of time for Gaussian pulses (2.15) with a pulse delay $\tau = 1.5T^{-1}$, peak Rabi frequency $\Omega_0 = 60T^{-1}$ and decay rates of $\Gamma_1 = 500T^{-1}$ and $\Gamma_3 = 1500T^{-1}$. Right plot: Final populations as a function of difference of decay rates γ. The same parameters for the pulses are used and the total decay rate is fixed to $\Gamma = 2000T^{-1}$. The grey area indicates the operation regime for this experiment, depending on pulse duration and pulse delay.

3. Physics of Optical Resonators

A simple optical resonator can be constructed by placing two mirrors at two different locations z_1 and z_2 on the optical axis. The radii of the mirrors, R_1 and R_2, must correspond to the radii of the beam wavefronts at the two locations. The beam in between the two mirrors is then reflected back an forth without a change of its transverse profile. Due to the fact that the reflection of a Gaussian beam from a mirror with a radius of curvature R is formally equivalent to its transmission through a lens with focal lens $f = \frac{R}{2}$, the following simple confinement condition can be derived

$$0 \leq (1 - g_1)\,(1 - g_2) \leq 1. \tag{3.1}$$

In this simple equation g_1 and g_2 are equal to $\frac{l}{R_1}$ and $\frac{l}{R_2}$, respectively. Thereby, R_1 and R_2 are the radii of curvature of the mirrors and l is the separation between them. Figure 3.1 shows the confinement diagram for optical resonators.

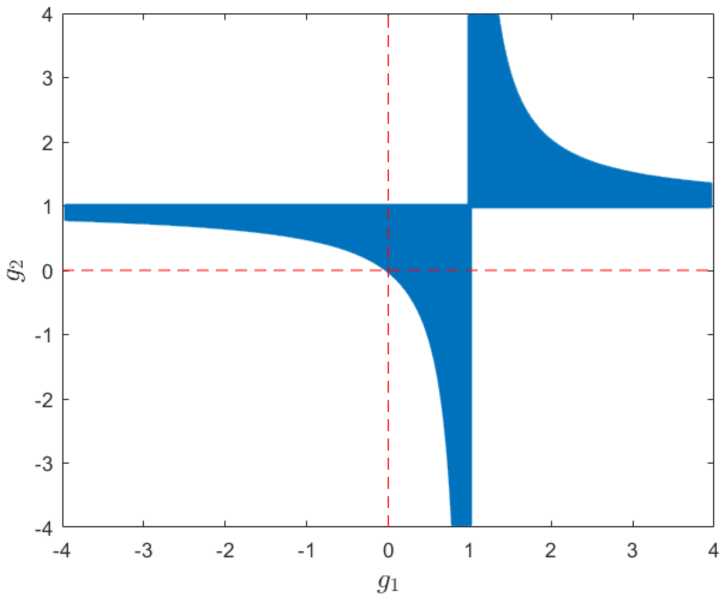

Figure 3.1.: Confinement diagram for optical resonators. Blue area shows the region where equation (3.1) is fulfilled and therefore the resonator is stable. Outside the blue area the resonator is unstable. For better orientation $g_1 = 0$ and $g_2 = 0$ are plotted as red dashed lines.

This section will give a short introduction how to describe the propagation of Gaussian beams through an arbitrary optical system, using the so called ABCD-Matrix method.

This allows us to construct more complicated optical resonators consisting of several optical elements instead of just two mirrors. The special case of a Bow-Tie Cavity will be discussed in one of the following sections. More detailed information can be found in [17], [18], [19], [20] and [21].

3.1. Gaussian Beams

Waves that exhibit the characteristics of an optical beam must satisfy the paraxial Helmholtz equation

$$\nabla_T^2 A - 2ik\frac{\partial A}{\partial z} = 0 \tag{3.2}$$

where $A = A(\vec{r})$ is the complex envelope, $\nabla_T^2 = \frac{\partial^2}{\partial x^2} + \frac{\partial^2}{\partial y^2}$ is the transverse part of the Laplace operator and k is the wavenumber. A special solution of the paraxial Helmholtz equation is the Gaussian beam. A general expression for the complex amplitude $U(\vec{r})$ of the Gaussian beam reads

$$U(\vec{r}) = A_0\frac{w_0}{w(z)}\exp\{-\frac{\rho^2}{w(z)^2}\}\exp\{-jkz - jk\frac{\rho^2}{2R(z)} + j\zeta(z)\} \tag{3.3}$$

with $\rho^2 = x^2 + y^2$. The other parameters appearing in equation (3.3) are briefly mentioned below. The beams spot size $w(z)$, also called the $1/e$-radius of the beam, is given by

$$w(z) = w_0\left[1 + \left(\frac{z}{z_0}\right)^2\right]^{1/2} \tag{3.4}$$

where z is the coordinate along which the beam is propagating. The radius of curvature $R(z)$ of the Gaussian beam is given by

$$R(z) = z\left[1 + \left(\frac{z}{z_0}\right)^2\right]. \tag{3.5}$$

The phase factor η

$$\eta = \arctan\left(\frac{z}{z_0}\right) \tag{3.6}$$

is called the Gouy phase. The minimum spot size w_0 characterizing the beam is given by

$$w_0 = \left(\frac{\lambda z_0}{\pi}\right)^{1/2} \tag{3.7}$$

where λ is wavelength of the beam and $z_0 = \frac{\pi w_0^2}{\lambda}$ is called the Rayleigh range. Sometimes, a Gaussian beam is characterized by it's confocal parameter, which is defined as $b = 2z_0$. The beam divergence in the far field is given by $\theta_0 = \frac{\lambda}{\pi \omega_0}$. A connection between the radius of curvature $R(z)$ and the spot size $w(z)$ is given by the complex beam parameter $q(z)$

$$\frac{1}{q} = \frac{1}{R} - i\frac{\lambda}{\pi W^2} \tag{3.8}$$

where the dependence of z is omitted in equation 3.8 [17, 20].

3.2. ABCD-Matrix Method

To develop the $ABCD$-Matrix method, we start considering light rays instead of Gaussian beams. A light ray is completely characterized by its hight y above the optical axis and its slope θ. In the paraxial approximation, where θ is small, the relation between an incoming ray (y_1, θ_1) and an outgoing ray (y_2, θ_2) is linear and can be written as

$$\begin{bmatrix} y_2 \\ \theta_2 \end{bmatrix} = \begin{bmatrix} A & B \\ C & D \end{bmatrix} \begin{bmatrix} y_1 \\ \theta_1 \end{bmatrix} \tag{3.9}$$

where A, B, C and D are characterizing the corresponding optical element through which the ray is passing or being reflected. The ABCD-Matrix of a system of optical components can be obtained by multiplication of the corresponding matrices. Table 3.1 presents a few important ABCD-Matrices.

A very useful property of all the $ABCD$-matrices (and systems composed of a number of optical elements) is that they are unimodular, i.e.

$$\det \begin{bmatrix} A & B \\ C & D \end{bmatrix} = AD - BC = 1. \tag{3.10}$$

The effect of different optical components on a Gaussian beam is described by the ABCD-law. The q parameters of an incident Gaussian beam q_1 and a transmitted/reflected Gaussian beam q_2 at the input and output planes of a paraxial optical system are related in the following way

$$q_2 = \frac{Aq_1 + B}{Cq_1 + D} \tag{3.11}$$

where A, B, C and D are again the components of the corresponding $ABCD$-matrices (or composite system). As it can be seen from equation (3.8), the beam parameter q connects the spot size $w(z)$ and the radius of curvature $R(z)$ of a Gaussian beam and therefore describes the effect of an arbitrary optical system on the Gaussian beam [17].

Table 3.1.: Summary of a number of important $ABCD$-Matrices. The parameter d describes a distance in free space, f is the focal length of a lens and R is the radius of curvature of a mirror ($R > 0$ for a concave and $R < 0$ for a convex mirror). $ABCD$-Matrices for other optical components can be found in [17], [19], [20] and [21].

Optical element	Sketch	ABCD-Matrix
Free space	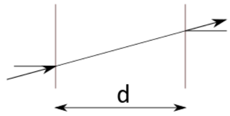	$\begin{bmatrix} 1 & d \\ 0 & 1 \end{bmatrix}$
Reflection from a planar mirror	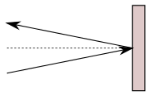	$\begin{bmatrix} 1 & 0 \\ 0 & 1 \end{bmatrix}$
Reflection from a spherical mirror	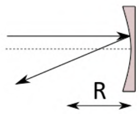	$\begin{bmatrix} 1 & 0 \\ \frac{-2}{R} & 1 \end{bmatrix}$
Transmission through a thin lens	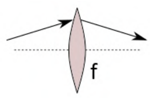	$\begin{bmatrix} 1 & 0 \\ \frac{-1}{f} & 1 \end{bmatrix}$

3.3. The Self-Consisted Method

To have a stable resonator, we require that the resonating mode reproduces it self after a complete round trip. Therefore one can choose an arbitrary reference plane inside the resonator and denote the complex beam parameter at this plane q. Using equating (3.11) the self-consistency condition reads

$$q = \frac{Aq + B}{Cq + D} \tag{3.12}$$

where A, B, C and D are the components of the transfer matrix of the whole resonator setup. Equation (3.12) can be transformed in a quadratic equation for $\frac{1}{q}$. Using the unimodularity of $ABCD$-matrices and comparing with equation (3.8) one gets

$$\frac{1}{q} = \frac{D - A}{2B} \pm i \frac{\sqrt{1 - \left(\frac{D+A}{2}\right)^2}}{B} = \frac{1}{R} - i \frac{\lambda}{\pi W^2} \tag{3.13}$$

For a confined Gaussian beam it is therefore necessary that

$$\left| \frac{D + A}{2} \right| \leq 1 \tag{3.14}$$

is fulfilled. Equation (3.14) can be viewed as a generalized confinement condition for an arbitrary optical resonator [20]. From equation (3.14) it is possible to derive expressions for the radius of curvature R and the beam spot size W at a chosen reference point

$$R = \frac{2B}{D - A} \tag{3.15}$$

$$w = \sqrt{\frac{2\lambda|B|}{\pi\sqrt{4 - (A + D)^2}}}. \tag{3.16}$$

Values at other points in the cavity can be obtained by using equations (3.5) and (3.4) [21].

3.4. Ring Cavities and Intensity Enhancement

Now, some of the key ideas concerning passive optical cavities are presented. Therefore, a plane wave model is used, which is applicable for both standing wave resonators (two mirror resonators) and travelling wave resonators (ring cavities).

In the following, we denote E_{inc} and E_{refl} as the incident and reflected complex signal amplitudes, respectively. E_{circ} denotes the circulating signal amplitude. The relation between the circulating and incoming field amplitudes is given by [18] [21]

$$\frac{E_{\text{circ}}}{E_{\text{inc}}} = \frac{t_1}{1 - r_1 r_m e^{-i\delta}} \tag{3.17}$$

where δ corresponds to a phase shift associated with one round trip. The parameters r_1 and t_1 are reflection and transmission coefficients of the mirror where the incoming signal is coupled in to the cavity. The parameter r_m combines the reflection (and eventually transmission) coefficients of the other elements. In the case of a cavity with four mirrors (like in a Bow-Tie configuration) and a lossy medium inside with transmission coefficient t, r_m reads

$$r_m = r_2 r_3 r_4 t. \tag{3.18}$$

In other words, r_m can be considered as the fraction of the electric field that remains inside the cavity after one round trip, excluding the transmission through the input mirror t_1. Using the quadratic dependence of the intensity upon the electric field amplitude, it is easy to calculate from equation (3.17) the fraction between incoming intensity I_{circ} and the circulating intensity I_{inc} [21]

$$\frac{I_{\text{circ}}}{I_{\text{inc}}} = \frac{t_1^2}{(1 - r_1 r_m)^2 + 4 r_1 r_m \sin^2(\delta/2)}. \tag{3.19}$$

For the reflected field E_{refl} and intensity I_{refl} similar expressions can be obtained [21]

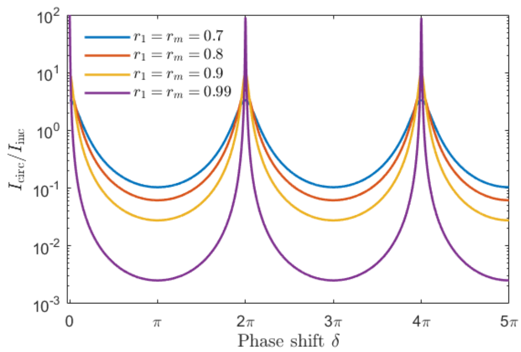

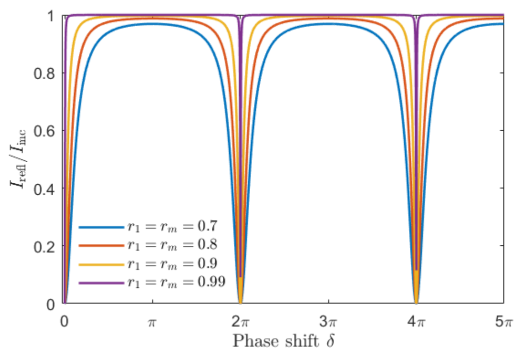

Figure 3.2.: Resonant behaviour of a ring cavity: Circulating intensity (left) and reflected intensity (right) as a function of phase shift δ according to equations (3.20) and (3.20). The values for reflection coefficients are chosen such that $r_m = r_1$.

$$\begin{aligned} E_{\mathrm{refl}} =& E_{\mathrm{inc}} \frac{r_m e^{-i\delta} - r_1}{1 - r_1 r_m e^{-i\delta}} \\ \frac{I_{\mathrm{refl}}}{I_{\mathrm{inc}}} =& \frac{(r_1 - r_m)^2 + 4 r_1 r_m \sin^2(\delta/2)}{(1 - r_1 r_m)^2 + 4 r_1 r_m \sin^2(\delta/2)}. \end{aligned} \tag{3.20}$$

Figure 3.2 shows the circulating intensity and the reflected intensity as a function of phase shift δ according to equations (3.20) and (3.20). One can see that for specific values of δ there is almost no circulating intensity and no reflected intensity. For a total round trip phase shift of $\delta = 2\pi q$, where q is a integer number, the circulating intensity inside the cavity is highest and almost no intensity is reflected. This confirms also the very customary result for the axial resonance frequencies of $\nu_q = q\frac{c}{Ln}$, where L is the path of a total cavity round trip ($L = 2\times$ mirror separation for standing wave resonators) and $\frac{c}{n}$ is the speed of light in a medium with refrative index n [21].
It is easy to see, that equation (3.19) is a periodic function in δ with a period of 2π. This is equivalent as to say that the free spectral range in terms of δ is 2π. The circulating intensity has a maximum for $\delta = 2\pi n$ where n is a integer number. A graphical representation of equation (3.19) shows figure 3.3.
Figure 3.3 shows that it is essential to minimize round trip losses in order to have r_m close to unity which implies high circulating field intensities. For $r_m = 0.99$ a circulating field intensity can be obtained that is ~ 100 times larger than the incident field intensity. Furthermore, one can see that the maximum circulating intensity is obtained for

$$r_1 = r_m. \tag{3.21}$$

Equation (3.21) is the so called **impedance-matching condition** [22]. This result can also be obtained by differentiating equation (3.19) (at resonance) with respect to r_1 and setting the result to zero. Equation (3.20) indicates that in this case (at resonance)

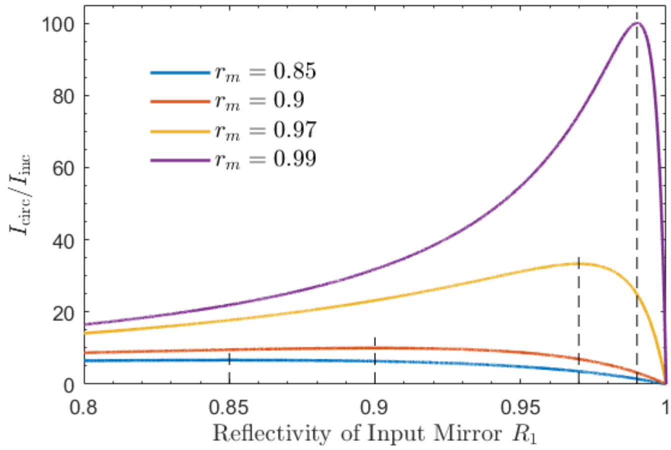

Figure 3.3.: Representation of equation (3.19) for $\delta = 2\pi n$ and different values of r_m. Figure adapted from [22].

there is zero reflected power. The half maximum intensity which occurs at a phase $\delta_{1/2}$ equal to

$$\delta_{1/2} \approx \frac{1 - r_1 r_m}{\sqrt{r_1 r_m}} \tag{3.22}$$

where we have assumed $\delta_{1/2} \ll 1$. The full width at half maximum (FWHM), denoted with $\Delta\nu_{1/2}$, of the circulating field at resonance, is therefore given by

$$\Delta\nu_{1/2} = 2\delta_{1/2} = \frac{2(1 - r_1 r_m)}{\sqrt{r_1 r_m}}. \tag{3.23}$$

A common definition for the finesse $\mathcal{F}$, is the free spectral range of the cavity divided by the FWHM of the circulating intensity resonances. Considering that the free spectral range in terms of phase shift is equal to 2π, the finesse reads

$$\mathcal{F} = \frac{FSR}{\Delta\nu_{1/2}} = \frac{\pi\sqrt{r_1 r_m}}{1 - r_1 r_m} = \frac{\pi}{\delta_{1/2}}. \tag{3.24}$$

Considering equation (3.24), a justification for the approximation ($\delta_{1/2} \ll 1$) for deriving equation (3.22) can be given: most useful cavities have a finesse $\mathcal{F} \gg 1$ which implies $\delta_{1/2} \ll \pi$. The results reported here can be found in greater detail in [17] and [21].

3.5. Bow-Tie Cavity

In this section a special typ of ring-cavity, the so called bow-tie cavity, is described. This cavity consists of four mirrors, two curved and two flat, which are aligned in such a way that the beam follows a zig-zag path. The curved mirrors have the same radii

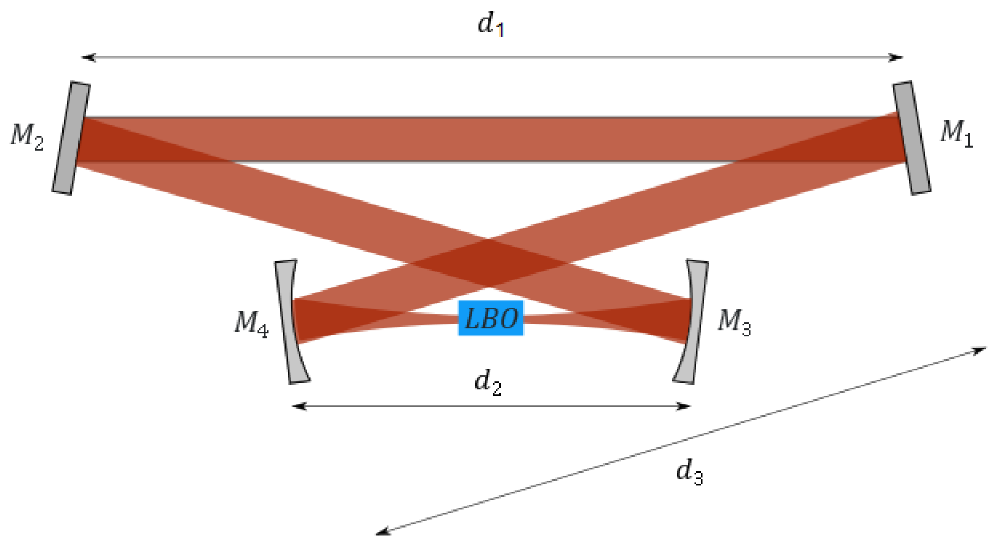

Figure 3.4.: Schematic representation of the symmetric bow-tie configuration. The cavity consists of two flat mirrors (M_1 and M_2) and two curved mirrors (M_3 and M_4). To perform second harmonic generation, a nonlinear crystal (*LBO*) lies in between the two curved mirrors. Figure adapted from [21].

and the configuration is symmetrical about a vertival line halfway between the mirrors (symmetric bow-tie configuration). A schematic representation of the bow-tie cavity is shown in figure 3.4.

To describe this kind of resonator we will use the $ABCD$-matrix method from section 3.2. Taking the corresponding matrices from table 3.1 and using equation (3.16) one can easily calculate the waist between the flat and between the curved mirrors. By choosing the reference planes lying exactly between the curvend mirrors and the flat mirrors, figure 3.5 results.

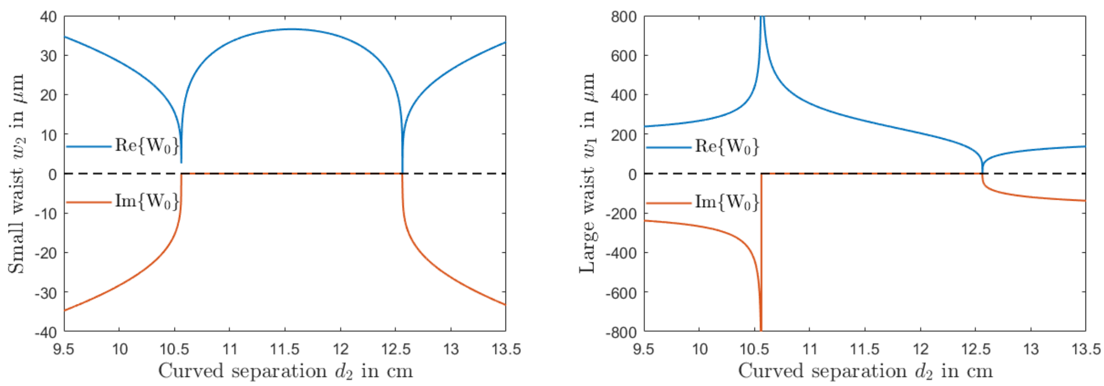

Figure 3.5.: Small waist (between curved mirrors) and large waist (between flat mirrors) calculated using equation 3.16 as a function of d_2. The following values for the calculation are used: $d_1 = d_3 = 20\,\mathrm{cm}$, $R = 10\,\mathrm{cm}$, $L_{\mathrm{crystal}} = 1.5\,\mathrm{cm}$, $n = 1.61$ and $\lambda = 840\,\mathrm{nm}$.

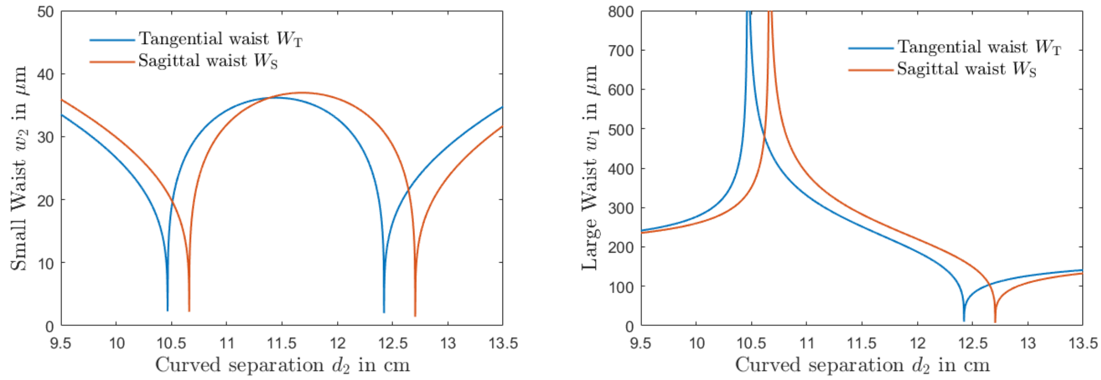

Figure 3.6.: Real part of tangential waist W_T and sagittal waist W_S between curved mirrors (left) and between flat mirrors (right) as a function of d_2. For the calculation the same parameters as in figure 3.5 are used.

Figure 3.5 shows the real part and the imaginary part of the small and large waist using equation (3.16). The resonator is stable if the imaginary part of both waists is zero. The resonator starts to be unstable in the regions where the small waist (left plot) is shrinking rapidly. As one can clearly see, the waist between the curved mirrors is roughly a factor of 10 smaller and therefore suitable as location for a nonlinear crystal. Figure 3.5 describes the behaviour of the waists qualitatively correct. Due to fact, that the curved mirrors are tilted by an angle θ the configuration is no longer cylindrical symmetric. The off axis reflection from the curved mirrors is responsible for the geometrical aberration, called **astigmatism**. In order to describe this problem it is helpful to define two planes: the tangential plane (parallel to the plane of incidence) and the sagittal plane (perpendicular to the tangential plane). Tangential rays will experience a different geometry than sagittal rays. It can be shown that off-axis reflection of a tilted mirror at angle θ leads to two individual focal lengths

$$\begin{aligned} f_T &= \frac{R\cos\theta}{2}, \\ f_S &= \frac{R}{2\cos\theta} \end{aligned} \tag{3.25}$$

for the tangential and sagittal plane, respectively [23]. This means that each plane has it's own $ABCD$ matrix and focus has to be replaced by (3.25). An analog calculation for the waists like before leads to figure 3.6.

Figure 3.6 shows the astigmatic behaviour of a bow-tie cavity. For the waists between the curved mirrors there is a special mirror d_2 separation where both waits are equal. For the chosen parameters here, this happens for a curved mirror separation of $d_2 \approx 11.4\,\mathrm{cm}$.

4. Second Harmonic Generation

The theory of linear optics was completely sufficient at that time where only classical light sources were available. With the invention of the laser, it was possible to interact with matter so strongly, that beside linear effects also nonlinear ones became noticeable. Second Harmonic Generation (SHG) is a subarea of this field, called nonlinear optics. By the interaction with materials, which show strong nonlinear behaviour, light with frequency ω is converted into light with frequency 2ω. First experiments of SHG had a conversion efficiency of the order 10^{-8}. To make this process more successful, more efficient materials, high laser frequencies and index matching techniques are needed. This chapter is intended to show the most important steps on the way to frequency-doubled light [21, 24].

4.1. Basic Optics in Crystals

Before starting with the theory of nonlinear optics the physical concepts of dispersion, birefringence and uniaxial crystals should be briefly reviewed. These terms are then needed for the following discussion of the SHG process. For a deeper explanation of these topics please [17], [25] and/or [26].

Dispersion

The role of dispersion in nonlinear optics is hard to overestimate. A very important property of the index of refraction is it's dependence on frequency. This variation of the index of refraction with frequency is called dispersion. Two different types of dispersion have to be distinguished: materials where the refractive index rises with increasing frequency (decreasing wavelength) are said to have normal dispersion and materials where the refractive index falls as the frequency increases are said to have anomalous dispersion [25].

Birefringence

The refractive index of a specific material is the factor by which the speed of light is reduced (relative to vacuum) inside the material. If the index of refraction is equal in all directions, then this special kind of material is called optically isotropic. Anisotropic materials have crystallographically distinct axes which lead to different refractive indices for different directions. In an anisotropic media, there is at least one direction of propagation of the incident wave in which the refractive index is independent of polarization. This direction is known as the **optic axis**. In the case of only one optic

axis, the material is called uniaxial crystal. If there are two optic axes, the material is called biaxial. Most of the crystals which occur in nature are biaxial crystals. These are much more difficult in their crystals geometry, but fortunately many electro optical devices and the effect of SHG deal with uniaxial crystals. Therefore, in the following we will concentrate only on the case of uniaxial crystals.
The wavefronts of the incident wave and refracted wave must match at the boundary. The anisotropic medium supports two modes of distinctly different phase velocities and therefore in an uniaxial crystal, two types of waves can propagate [17, 26]:

(i) **Ordinary waves**: waves linearly polarized and perpendicular to the plane formed by the optic axis and the direction of incidence. For ordinary waves, the wave passes through the crytsal satisfying Snell's law.

(ii) **Extraordinary waves**: waves linearly polarized and parallel to the plane formed by the optic axis and the direction of incidence. The refractive index for this type of wave depends on the direction of propagation inside the medium.

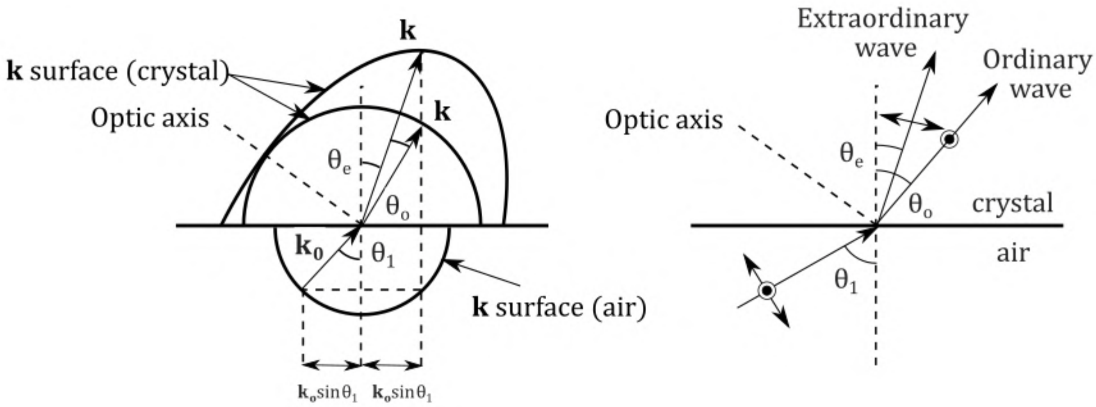

Figure 4.1.: Intersection of the **k**-surfaces of a nonlinear crystal and air (left) and ray corresponding picture (right). θ_1 is the angle of incidence. θ_o and θ_e are the angles of refraction of the ordinary and extraordinary wave, respectively. Figure adapted from [17].

Uniaxial Crystals

As already mentioned we limit our discussion to uniaxial crystals. These kind of crystals only posses one optical axis and their index surfaces are shown in figure 4.2.

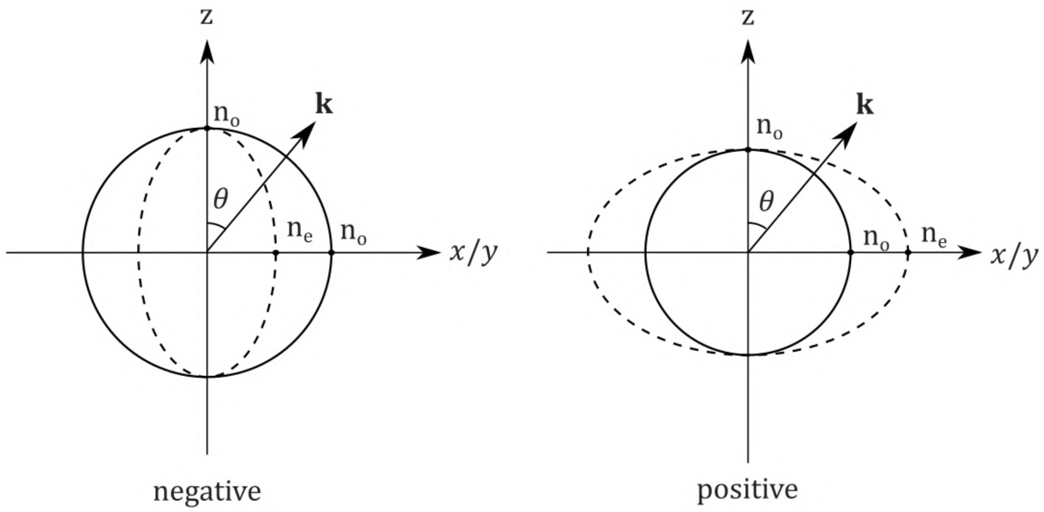

Figure 4.2.: Index surfaces for a negative (left) and a positiv (right) uniaxial crystal. θ is the angle between the z-axis (optic axis) and the **k**-vector of an electromagnetic wave travelling inside the crystal. n_o and n_e are called principal values of the ordinary and extraordinary refractive index.

The left plot of figure 4.2 shows a negative ($n_\mathrm{e} < n_\mathrm{o}$) uniaxial crystal and the right plot shows a positive ($n_\mathrm{o} < n_\mathrm{e}$) uniaxial crystal. The ordinary wave experience always the same index of refraction n_o, regardless of their direction of propagation. The extraordinary wave experience a angle dependant index of refraction $n_\mathrm{e} = n_\mathrm{e}(\theta)$. This is true for both, negative and positive uniaxial crystals. Some examples for positive uniaxial crystals are quarz (SiO_2) and lithium tantalate ($LiTaO_3$). Lithium niobate ($LiNbO_3$), potassium dihydrogen phosphate (KH_2PO_4) or KDP and lithium triborate (LiB_3O_5) or LBO are examples that exhibit negative birefringence [25].

4.2. Introduction to Nonlinear Optics

All linear dielectric media are related by the well known linear relation $P = \epsilon_0 \chi E$. The polarisation density P connects the permeability of free space ϵ_0, the dielectric susceptibility χ and the electric field E. This scalar equation neglects anisotropy, dispersion and inhomogenity. Non linear dielectric media are characterized by a more complicated relation between P and E. Typically, the relation between P and E is linear for small values of E, but becomes nonlinear as E increases. Even for very strong optical fields the nonlinear contribution of the electric field to polarisation density is small and hence P can be expanded in a Taylor series around E =0:

$$P = a_1 E + \frac{1}{2} a_2 E^2 + \frac{1}{6} a_3 E^3 + ..., \tag{4.1}$$

where the a_i are the i^{th} derivatives of P with respect to E evaluated at E =0. The a_i parameters are characteristic constants of the medium. It is often convenient to replace the a_i parameters by $a_1 = \epsilon_0\chi$, $\frac{1}{2}a_2 = 2d$ and $\frac{1}{6}a_3 = 4\chi^{(3)}$. To consider that the medium can be anisotropic, each of the components of the polarization vector $\vec{P} = (P_1, P_2, P_3)$ is a function of the three components of the electric field $\vec{E} = (E_1, E_2, E_3)$. Then a more general formula reads

$$P_i = \epsilon_0\chi_{ij}E_j + 2d_{ijk}E_jE_k + 4\chi^{(3)}_{jkl}E_jE_kE_l \tag{4.2}$$

with $i, j, k, l = (x, y, z)$ and we assume summation over repeated indices. The coefficients arising in this formula are tensor elements of χ, d and $\chi^{(3)}$ for the scalar case. The third term on the right hand side of equation (4.1) and 4.2 is only important for third order nonlinear optics and is therefore neglected throughout the whole chapter [17]. It should be noted, that P_i is the instantaneous polarization density and E_i is the instantaneous electric field, both of the i^{th} component. Considering the coupling of two optical fields given by

$$\begin{aligned} E^{\omega_1}_j(t) &= Re\{E^{\omega_1}_j e^{i\omega_1 t}\} = \frac{1}{2}(E^{\omega_1}_j e^{i\omega_1 t} + c.c) \\ E^{\omega_2}_k(t) &= Re\{E^{\omega_2}_k e^{i\omega_2 t}\} = \frac{1}{2}(E^{\omega_1}_k e^{i\omega_2 t} + c.c) \end{aligned} \tag{4.3}$$

where $k, j = (x, y, z)$. In a nonlinear medium, these field components are responsible for polarization densities at frequencies $n\omega_1 + m\omega_2$, where n and m can take any integer values. As an example we take the polarization density component at $\omega_3 = \omega_1 + \omega_2$ along the i-direction which is given by

$$P^{\omega_3=\omega_1+\omega_2}_i(t) = Re\{P^{\omega_3}_i e^{i\omega_3 t}\}. \tag{4.4}$$

By limiting our attention only to the second term of equation (4.2) and considering only the sum frequency term we obtain

$$P^{\omega_3=\omega_1+\omega_2}_i(t) = d_{ijk}E^{\omega_1}_j E^{\omega_2}_k e^{i(\omega_1+\omega_2)t} + c.c. \tag{4.5}$$

where we have assumed, that our system is lossless (instantaneous response) and therefore $d_{ikj} = d_{ijk}$. This assumption is justified because in many nonlinear experiments the used material is transparent over a region that includes the involved frequencies [27].

4.3. Coupled Amplitude equations

In this section we denote the arbitrary direction of propagation through a nonlinear crystal as z. Furthermore, we are considering only three frequencies ω_1, ω_2 and ω_3 and assuming travelling plane waves. With this prerequisites we will introduce a set of coupled amplitude equations which are then applied to the special case of SHG (frequency doubling). A more detailed derivation can be found in [20].
When considering Maxwell's equation in dielectric materials, the electric field $\vec{E}$ has

to be replaced by the electric displacement $\vec{D} = \epsilon_0 \vec{E} + \vec{P}$. This allows us to bring the equations in a form which includes the polarization density $\vec{P}$ explicitly. The polarisation density consists of a linear and a nonlinear term

$$\vec{P} = \epsilon_0 \chi_L \vec{E} + \vec{P}_{NL} \tag{4.6}$$

where the tensor aspect of the linear susceptibility χ_L is completely ignored. The nonlinear part of the polarisation density is given by

$$(P_{NL})_i = 2d'_{ijk} E_j E_k \tag{4.7}$$

where the tensor d'_{ijk} is second order susceptibility tensor of equation 4.2 transformed from the crystal coordinate system to a Cartesian system, used to describe the propagation. Then the coupled amplitude equations can be written as

$$\begin{aligned}
\frac{dE_{1i}}{dz} &= -\frac{\sigma_1}{2}\sqrt{\frac{\mu_0}{\epsilon_1}} E_{1i} - i\omega_1 \sqrt{\frac{\mu_0}{\epsilon_1}} d'_{ijk} E_{3j} E^*_{2k} e^{-i(k_3-k_2-k_1)z} \\
\frac{dE^*_{2k}}{dz} &= -\frac{\sigma_2}{2}\sqrt{\frac{\mu_0}{\epsilon_2}} E^*_{2k} + i\omega_2 \sqrt{\frac{\mu_0}{\epsilon_2}} d'_{kij} E_{1i} E^*_{3j} e^{-i(k_1-k_3+k_2)z} \\
\frac{dE_{3j}}{dz} &= -\frac{\sigma_3}{2}\sqrt{\frac{\mu_0}{\epsilon_3}} E_{3j} - i\omega_3 \sqrt{\frac{\mu_0}{\epsilon_3}} d'_{jik} E_{1i} E_{2k} e^{-i(k_1+k_2-k_3)z}.
\end{aligned} \tag{4.8}$$

4.3.1. SHG without Depleted Input

In the following we will work with equations (4.8). In the case of SHG $\omega_1 = \omega_2$ and $\omega_3 = 2\omega_1$. If we assume, that the amount of power lost form the input beam (ω_1) due to conversion is negligible ($\frac{dE_{1i}}{dz} \approx 0$), then we only have to consider the last equation of (4.8). For a transparent medium at frequency ω_3 the conductivity $\sigma_3 = 0$ and we have

$$\frac{dE_{3j}}{dz} = -i\omega \sqrt{\frac{\mu_0}{\epsilon}} d'_{jik} E_{1i} E_{2k} e^{-i\Delta k z} \tag{4.9}$$

where we set $\omega = \omega_1 = \frac{1}{2}\omega_3$, $\epsilon = \epsilon_3$ and $\Delta k = k_3^{(j)} - k_1^{(i)} - k_1^{(k)}$. The propagation constant at ω_1 and along direction i is denoted by $k_1^{(i)}$. If we solve equation (4.9) for $E_{3j}(0) = 0$ and a crystal length of L and express the result in terms of power [1] we end up with

$$\frac{P^{(2\omega)}}{P^{(\omega)}} = 2\left(\frac{\mu_0}{\epsilon_0}\right)^{3/2} \frac{\omega^2 L^2 d'^2_{ijk}}{n^3} \left(\frac{P^{(\omega)}}{A}\right) \frac{\sin^2(\frac{1}{2}\Delta k L)}{(\frac{1}{2}\Delta k L)^2} \tag{4.10}$$

where we have taken $\epsilon_1 \simeq \epsilon_3 = \epsilon_0 n^2$.
The conversion efficiency, given by equation (4.10) is proportional to the sinc($\frac{1}{2}\Delta$kL)

[1] $\frac{P^{(2\omega)}}{A} = \frac{1}{2}\sqrt{\frac{\epsilon}{\mu_0}} E_{3j} E^*_{3j}$

function. For a $\Delta k = 0$ the conversion efficiency is highest as can be seen in figure 4.3 (left). If $\Delta k \neq 0$ then the conversion efficiency drops dramatically. Furthermore, it imposes an oscillating behaviour on the second-harmonic generated output power (see figure 4.3, right). Two adjacent maxima of equation (4.10) are separated by the so called coherence length

$$L_C = \frac{2\pi}{\Delta k} = \frac{2\pi}{k^{(2\omega)} - 2k^{(\omega)}} \tag{4.11}$$

where $\omega_1 = \omega_2 = \omega$ and $\omega_3 = 2\omega$. Equation 4.11 gives a measure for the maximum useful length of the crystal in SHG [20] [27].

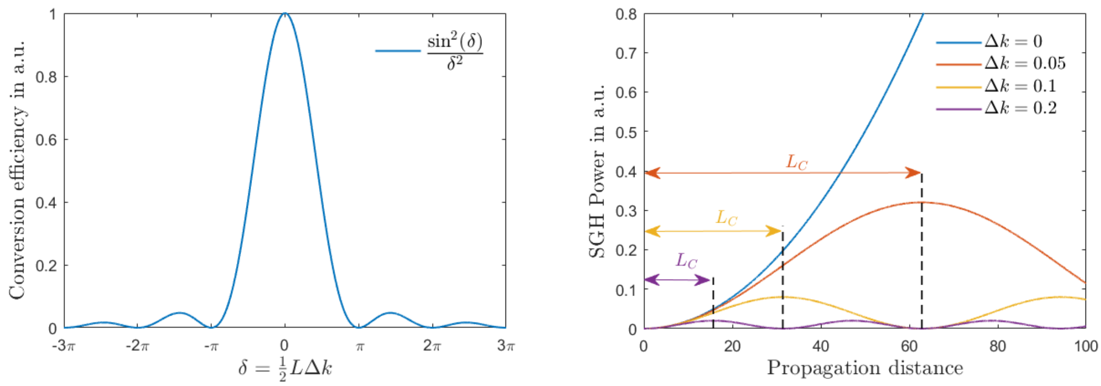

Figure 4.3.: Effects of phase mismatch on SHG efficiency. Left plot: normalized SHG conversion efficiency as a function of phase mismatch according to equation (4.10). Right plot: SHG power as a function of propagation distance for different values of Δk.

4.3.2. Phase Matching Techniques

According to equation (4.10), $\Delta k = 0$ or equivalently for SHG $k^{(2\omega)} = 2k^{(\omega)}$, has to be fulfilled to achieve high conversion efficiencies. By using the relation $k^{(\omega)} = \omega\sqrt{\mu\epsilon_0}n^{(\omega)}$, this **phase-matching requirement** can be written as

$$n^{(2\omega)} = n^{(\omega)}. \tag{4.12}$$

This means that the indices of refraction of the fundamental and the second-harmonic frequencies must be equal. Alternatively, one can say that the fundamental and the second harmonic wave must have the same phase velocity. If this is not the case, destructive interference between the second harmonic waves generated at different locations takes place. To achieve high conversion efficiencies a variety of methods have been developed to perform phase matching. The two most common phase matching techniques are birefringent phase matching and quasi phase matching. In the following, we concentrate on birefringent phase matching only since this is the used method in this thesis. .

Type I and Type II Phase Matching

As already mentioned, if the refractive index depends on the polarization direction of the optical radiation, then the material is birefringent. Here we concentrate our discussion on uniaxial crystals. In the case of SHG, both input fields can be of the same or of orthogonal polarizations. The special case of phase matching, where both polarizations are the same, is called **type-I** phase-matching. Two photons with the same polarization and frequency ω are transformed in one photon with orthogonal polarization and frequency 2ω:

$$\begin{gathered} k_{\mathrm{w,o}} + k_{\mathrm{w,o}} \rightarrow 2k_{\mathrm{2w,e}} \\ \text{or} \\ k_{\mathrm{w,e}} + k_{\mathrm{w,e}} \rightarrow 2k_{\mathrm{2w,o}} \end{gathered} \tag{4.13}$$

Under normal dispersion, the second harmonic generated wave experiences a higher index of refraction. Therefore, for a negative uniaxial crystal, the fundamental wave has to be ordinary polarized and the second harmonic generated wave has to be extraordinary polarized. For a positive uniaxial crystal the vice versa is the case.
When the input fields have orthogonal polarizations, the process is called **type-II** phase-matching. Two photons with orthogonal polarizations and frequency ω are transformed in one photon with frequency 2ω:

$$\begin{gathered} k_{\mathrm{w,o}} + k_{\mathrm{w,e}} \rightarrow 2k_{\mathrm{2w,o}} \\ \text{or} \\ k_{\mathrm{w,o}} + k_{\mathrm{w,e}} \rightarrow 2k_{\mathrm{2w,e}} \end{gathered} \tag{4.14}$$

The latter is less tunable since only one field's refractive index can be used for compensation of the index difference between ω and 2ω [21, 28].

Birefringent Phase Matching

A very common method to achieve phase matching is by using birefringence, an effect displayed by many crystals. In an uniaxial crystal the index of refraction of the extraordinary wave is a function of the angle θ between the propagation direction of the fundamental wave and the crystal optic axis. This relationship reads

$$\frac{1}{n_e^2(\theta)} = \frac{\cos^2\theta}{n_o^2} + \frac{\sin^2\theta}{n_e^2}. \tag{4.15}$$

In equation (4.15) n_o and n_e are the principal values of the ordinary and extraordinary refractive index. By changing the propagation direction of the fundamental wave, one can change the extraordinary index of refraction, but not the ordinary. This makes phase matching possible over a wide range of wavelengths. The second-harmonic wave has to be polarized along the direction of the lower refraction index. In a negative uniaxial crystal this corresponds to the extraordinary index of refraction. In the case of a negative uniaxial crystal, where $n_e^{(\omega)} < n_o^{(\omega)}$, equation (4.15) can be solved by setting $n_o^{(\omega)} = n_e^{(2\omega)}$

$$\sin^2\theta = \frac{(n_o^{(\omega)})^{-2} - (n_o^{(2\omega)})^{-2}}{(n_e^{(2\omega)})^{-2} - (n_o^{(2\omega)})^{-2}}. \tag{4.16}$$

This process is shown in the right plot of figure 4.4. Phase matching takes place where the solid blue line and the dotted orange line intersect.

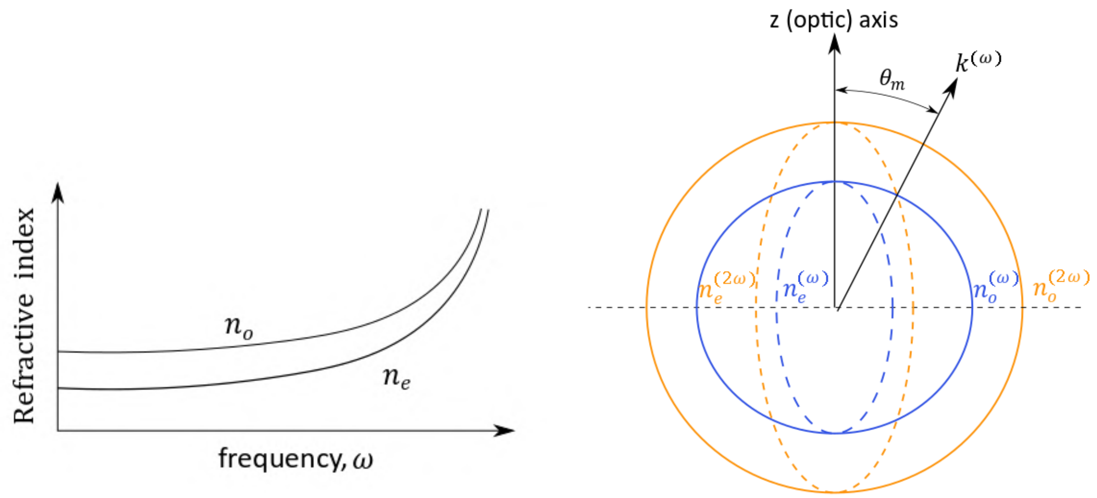

Figure 4.4.: Birefringent phase matching. Left plot: refractive indices for ordinary and extraordinary direction of propagation. Right plot: index surfaces for a negative uniaxial crystal for the fundamental frequency ω and the second harmonic generated frequency 2ω.

The method discussed above to achieve phase matching is also known as angle tuning. Another method which makes use of the birefringence of the crytsal is called temperature tuning. Due to the fact the the refractive indices depend on temperature, it is possible to make he values for the ordinary and extraordinary refractive index equal. This method often requires high temperatures and is more difficult to perform.

4.3.3. SHG with Depleted Input

Equation (4.10) assumes that during the interaction with the nonlinear crystal no power of the fundamental wave gets lost. Therefore, theses results are valid only for situations where the fraction of the converted input power is very small. This sections gives the results which lift this restriction. More detailed information can be found in [20] and/or [27].

By defining new field variables $A_l = \sqrt{\frac{n_l}{\omega_l}} E_l$ where $l = 1, 2, 3$, the coupled amplitude equations 4.8 can be written in a more convenient way

$$
\begin{aligned}
\frac{dA_1}{dz} &= -\frac{1}{2}\alpha_1 A_1 - i\kappa A_2^* A_3 e^{-i\Delta k z} \\
\frac{dA_2^*}{dz} &= -\frac{1}{2}\alpha_2 A_2^* + i\kappa A_1 A_3^* e^{i\Delta k z} \\
\frac{dA_3}{dz} &= -\frac{1}{2}\alpha_3 A_3 - i\kappa A_1 A_2 e^{i\Delta k z}.
\end{aligned}
\tag{4.17}
$$

The subscripts 1,2,3 correspond to the polarization directions of the electric fields $\mathbf{E}_1, \mathbf{E}_2, \mathbf{E}_3$. The new appearing parameters are

$$
\begin{aligned}
\kappa &\equiv d'_{123}\sqrt{\frac{\mu_0}{\epsilon_0}\frac{\omega_1\omega_2\omega_3}{n_1 n_2 n_3}} \\
\alpha_l &\equiv \sigma_l\sqrt{\frac{\mu_0}{\epsilon_0}} \qquad l = 1, 2, 3.
\end{aligned}
\tag{4.18}
$$

The advantage of equations (4.17) over equations (4.8) is that the former ones contain only one single coupling parameter κ. In the case of SHG $A_1 = A_2$ and under phase matched conditions $\Delta k = 0$, the coupled amplitude equations (4.17) can be solved

$$
A_3(z) = iA_1(0)\tanh[\kappa A_1(0)z] \tag{4.19}
$$

and the conversion efficiency therefore reads

$$
\frac{P^{(2\omega)}}{P^{(\omega)}} = \frac{|A_3(z)|^2}{|A_1(0)|^2} = \tanh^2[\kappa A_1(0)z]. \tag{4.20}
$$

In the last equation $P^{(\omega)} \equiv P(\omega, z = 0)$ is the input power and $P^{(2\omega)} \equiv P(2\omega, z)$ is the second harmonic generated power after an interaction distance of z. By means of energy conservation $P(\omega, 0) = P(\omega, z) + P(2\omega, z)$ it follows from (4.20) that

$$
\frac{P(\omega, z)}{P(\omega, 0)} = \frac{1}{\cosh^2[\kappa A_1(0)z]}. \tag{4.21}
$$

Figure 4.5 plots equations (4.20) and (4.21). Since $A_1 = A_2$, for $\kappa A_1(0)z \to \infty$ all the input photons can be converted into half as many output photons at twice the frequency [20].

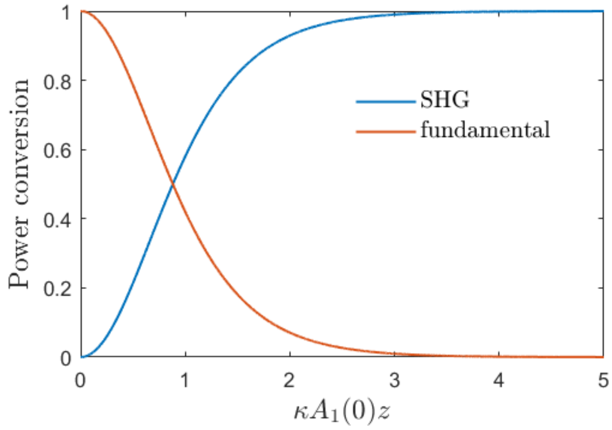

Figure 4.5.: Power conversion of the input power $P(\omega, 0)$ to SHG power $P(2\omega, z)$ according to equations 4.5 and (4.20) and (4.21), respectively.

4.4. Boyd-Kleinman analysis for SHG

So far, all the presented results in this chapter are based on a plane wave model. Boyd and Kleinman were able to think one step further and examined SHG using a focused, circular Gaussian beam in a material exhibiting walk-off. For the chosen parameters like in figure 3.6 this situation occurs in a bow-tie cavity. For the case of type I phase matching, the second harmonic generated wave underlies the influence of birefringence and hence propagates at an angle ρ relative to the fundamental wave. Due to this lateral spatial displacement, the output second harmonic generated beam has no longer a Gaussian distribution. A clean derivation of the Boyd-Kleinman approach is rather complicated and long. For the sake of brevity, only the key result is shown here. The power of the second harmonic generated wave is given by the following expression

$$P^{(2\omega)} = \frac{16\pi d_{\text{eff}}^2}{\epsilon_0 c \lambda^{(\omega)} n^{(\omega)} n^{(2\omega)}} e^{-\alpha' l} h(\sigma, \beta, \kappa, \xi, \mu)(P^{(\omega)})^2 := K(P^{(\omega)})^2. \tag{4.22}$$

In the above expression, $P^{(2\omega)}$ and $P^{(2\omega)}$ are the power of the second harmonic and fundamental wave and $n^{(2\omega)}$ and $n^{(\omega)}$ their corresponding refractive indices. The fundamental wavelength is given by $\lambda^{(\omega)}$ and d_{eff} is the effective second order susceptibility. The parameter $\alpha' = \alpha^{(\omega)} + \frac{\alpha^{(2\omega)}}{2}$ is a loss parameter for both wavelengths and $h(\sigma, \beta, \kappa, \xi, \mu)$ is the Boyd-Kleinman factor. The length of the crystal is denoted by l and c and ϵ_0 are the well known constants for the speed of light and the vacuum permittivity [29]. The crucial parameter to determine the second harmonic generated power is the Boyd-Kleinman factor $h(\sigma, \beta, \kappa, \xi, \mu)$ because it contains all the optimizable parameters. Now, a brief explanation of the involved parameters is given. The parameters are given by $\sigma = b\Delta k/2$, $\beta = \rho/\theta_0$, $\kappa = ab/2$, $\xi = l/b$ and $\mu = 1 - 2f/l$:

- σ: phase mismatch parameter that describes the phase mismatch between fundamental and second harmonic wave, in which $b = \frac{2\pi\omega_0^2}{\lambda}$ is the confocal parameter already introduced in section 3 and Δk is given by equation (4.11).

- β: walk-off parameter that describes the influence of the walk-off ρ in contrast to the Gaussian beam divergence $\theta_0 = \frac{\lambda}{\pi \omega_0}$.

- κ: absorption parameter that describes the absorption inside the crystal.

- ξ: foscusing parameter that gives simply the length of the crystal in units of the confocal parameter.

- μ: displacement parameter which measures the displacement of the focus from the center of the crystal.

The scope of this section is to show the influence of the birefringence and the focusing for the SHG process. This is done by varying the confocal parameter b. If losses ($\kappa = 0$) are neglected and we assume that the Gaussian beam is focused at the center ($\mu = 0$) of the crystal we only need to evaluate $h(\sigma, \beta, \xi)$. With the definition of $B = \beta\sqrt{\xi}$, the Boyd-Kleinman factor $h(\sigma, B, \xi)$ has to maximized by varying only the confocal parameter b. This is done by using analytical functions for the Boyd-Kleinman factor provided by [30] where an optimum phase mismatch parameter σ is used.

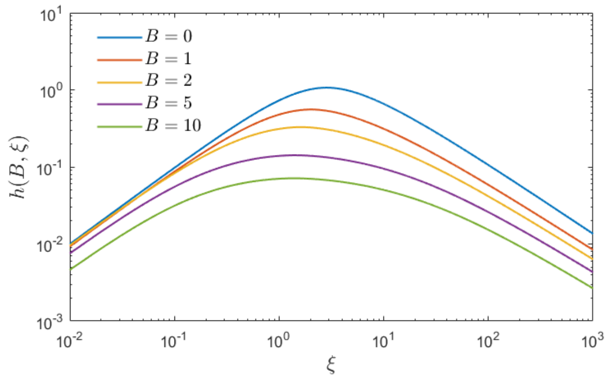

Figure 4.6.: Boyd-Kleinman factors $h(B, \xi)$ as a function of the focusing parameter ξ under conditions of optimal phase mismatch σ according to [30].

Figure 4.22 shows a strong dependence of the h-function with B. The highest value of $h = 1.068$ is obtained for $B = 0$ (no walk-off, $\rho = 0$). For higher values of B the Boyd-Kleinman factor is decreasing. Furthermore, one can see that the maxima of h are shifted to smaller ξ values for increasing values of B. This means that with increasing B, less focusing (smaller ξ) is needed to obtain the maximum possible value. This can be seed by using the expression for ξ in combination with (3.7) and obtaining $w_0 = \sqrt{\frac{l\lambda}{2\pi\xi}}$.

Combining the above equations, one obtains $B = \rho\sqrt{\frac{\pi l n}{2\lambda}}$, λ being the fundamental wavelength and n the refraction index of the LBO crystal. By taking the corresponding values for the LBO crystal from [31] and assuming that these values do not change much for the wavelengths used in this experiment, one obtains a value for B of 3.5. The Boyd-Kleinman factor from equation (4.22) has then a maximum value of $h(B, \xi)$ = 0.19 at $\xi = 1.47$. The length of the crystal is $l = 15\,\mathrm{mm}$. The obtimum waist for this specific case results to be $w_0 = 36\,\mu\mathrm{m}$. This is the same value for the tangential and sagittal waist seen in figure 3.6 for a curved mirror separation of $d_2 = 11.4\,\mathrm{cm}$.

4.5. SHG in a Bow-Tie Cavity

To achieve high conversion efficiencies in a SHG process, high powers of the fundamental wave are needed. Therefore, a large enhancement factor for the fundamental power can be obtained by using a bow-tie cavity and hence performing intra-cavity SHG. Even though all of the results from section 3.4 are true for standing wave cavities and travelling cavities, the latter are preferred due to their simplicity in SHG geometry. The reason for that is, that in a standing wave cavity the fundamental wave circulates into two directions which generates also the second harmonic in two directions [32].

4.5.1. Optimum intra-cavity SHG

The bow-tie cavity has an input coupler with transmissivity T_1 and intra-cavity losses L. This losses consist of intra-cavity losses due to reflection at the cavity mirrors (excluding the input coupler) and transmission through the nonlinear crystal as well as losses due to conversion from of the intra-cavity P_{circ} power into second harmonic power $P^{(2\omega)}$. The latter one is equal to

$$L_{\mathrm{NL}} = \frac{P^{(2\omega)}}{P_{\mathrm{circ}}} = K P_{\mathrm{Circ}} \tag{4.23}$$

where K is the nonlinear conversion coefficient from equation 4.22. The overall SHG conversion efficiency is defined as

$$\eta = \frac{P^{(2\omega)}}{P_{\mathrm{inc}}} \tag{4.24}$$

where P_{Inc} is the incoming power before entering the bow-tie cavity (see equation (3.19)) [32]. By means of equation (3.19) (at resonance, $\delta = 2m\pi$) and equation (4.23) it is easy to obtain

$$P_{\mathrm{circ}} = \frac{P_{\mathrm{inc}} T_1}{[1 - \sqrt{(1 - T_1)(1 - L_{\mathrm{Cav}})(1 - K P_{\mathrm{circ}})}]^2}. \tag{4.25}$$

In the above equation the factor $(1 - L_{\mathrm{Cav}}) = R_m$. The parameter R_m is equal to r_m^2, where r_m is defined by equation (3.18). Equation (4.25) represents a quadratic equation in P_{circ}. Therefore, the circulating power P_{circ} can be maximized by choosing an input coupler with transmission [31]

$$T_1 = \frac{L_{\mathrm{Cav}}}{2} + \sqrt{\frac{L_{\mathrm{Cav}}^2}{4} + KP_{\mathrm{inc}}}. \tag{4.26}$$

4.5.2. Locking the Cavity to the Laser

Optical resonators underlie many perturbations such as pressure changes, temperature changes and mechanical/acoustical resonances. To make an optical resonator work properly, the resonator must be kept on resonance with the incoming radiation. To achieve this, the probably most widespread methods are the Pound–Drever–Hall (PDH) scheme and the Hänsch-Couillaud (HC) scheme. The PDH scheme uses a frequency-modulated signal reflected from the cavity and is usually used for locking a laser to a cavity. The HC scheme instead, is used to lock the cavity to the laser. This method does not need a frequency-modulated signal, but a intra-cavity polarizing element. Since this element is already present by the nonlinear crystal, the HC scheme is the method of choice [21].

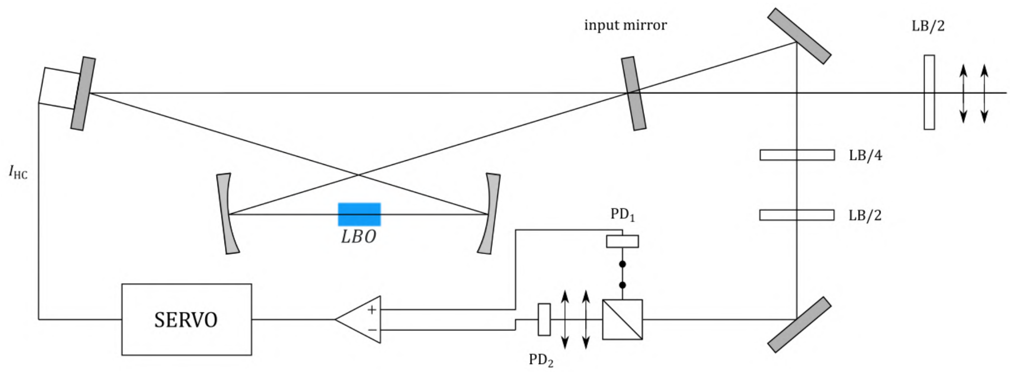

Figure 4.7.: Adapted Hänsch-Couillaud locking scheme.

The HC method was proposed in the 1980 [33] and is sometimes also known as passive polarization scheme. Figure 4.7 shows how the HC scheme can be implemented with a bow-tie cavity and a non linear crystal (LBO). Before the light enters the cavity, a $\lambda/2$ wave-plate is used to rotate the vertical polarization (parallel to the resonator axis) by a small angle θ. In the following we assume that the finesse of the cavity is very high for the vertical- (y) and very low for the horizontal (x) direction. This is justified due to the fact that the crystal inside the cavity does only support y-polarized light. Therefore, x polarized light is directly reflected at the input mirror and y-polarized light experiences a frequency dependant phase shift δ. After one round trip inside the resonator, y- and x-polarized components recombine again. If the resonance condition is fulfilled, then the y-polarized light does not experience any phase shift and both components combine again to linear polarized light. If, on the other hand, the resonance condition is not fulfilled and hence $\delta \neq 2\pi m$ (m any integer number), due to the phase shift both components combine to elliptically polarized light. By means of a $\lambda/4$ wave-plate (and a $\lambda/2$ wave-plate in order to have an additional degree of freedom) elliptically polarized light is converted to linear polarized light. A PBS is then used to separate x- and y- polarized components which have different amplitudes and sends them to a photo diode. The difference of these two signals is given by

$$I_{\mathrm{HC}} \propto 4E_0^2 r_{\mathrm{m}}^2 t^2 \cos\theta \sin\theta \frac{\sin\delta}{(1-r_{\mathrm{m}}^2)^2 + 4r_{\mathrm{m}} \sin^2\delta} \tag{4.27}$$

where t is the field transmission coefficient of the input mirror and r_{m} is given by (3.18). If the resonance condition is fulfilled, both photo diodes receive the same signal and equation (4.27) is equal to zero, otherwise it is different from zero. This signal is feed to a control electronics (see Appendix B.1) which holds the cavity on resonance. Figure 4.8 shows the error signal according to equation (4.27) for different angles of θ. For more detailed information see [21] or [33].

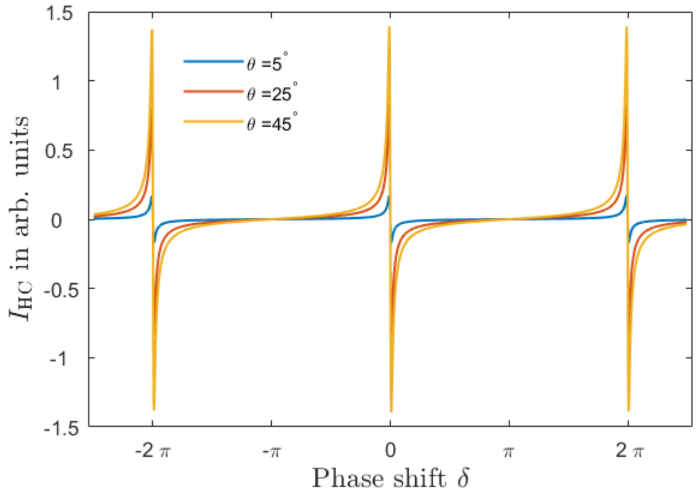

Figure 4.8.: Hänsch-Couillaud error signal for different angles θ as a function of phaseshift δ.

5. Experimental Setup

The purpose of this chapter is to give an insight in the experimental setup. When possible, it is avoided to introduce new equations and for more detailed explanation reference is made to the corresponding literature. A schematic layout is shown in figure 5.1. The setup consists mainly of four parts. The first part is an external-cavity diode laser (ECDL) (green dashed frame) in cat's eye design. The emitted light should have a wavelength of $\lambda_{\text{fund}} = 837.2\,\text{nm}$ with a possibly small bandwidth. The second part (red dashed frame) of the setup is a tapered amplifier (TPA). The optical power emitted from the ECDL will be amplified by a factor of 10 to 100. The third part (orange dashed frame) is a bow-tie cavity wit an nonlinear crystal inside. The cavity itself increases the optical power inside the cavity up to several Watts. When the light passes through the crystal, the desired wavelength of $\lambda_{\text{SHG}} = 418.6\,\text{nm}$ is generated due to SHG. The last part consists of an AOM in a double-pass configuration (blue dashed frame) and is used for pulse shaping. In the following these four parts are discussed in more detail. Figure 5.2 shows a picture of the entire setup.

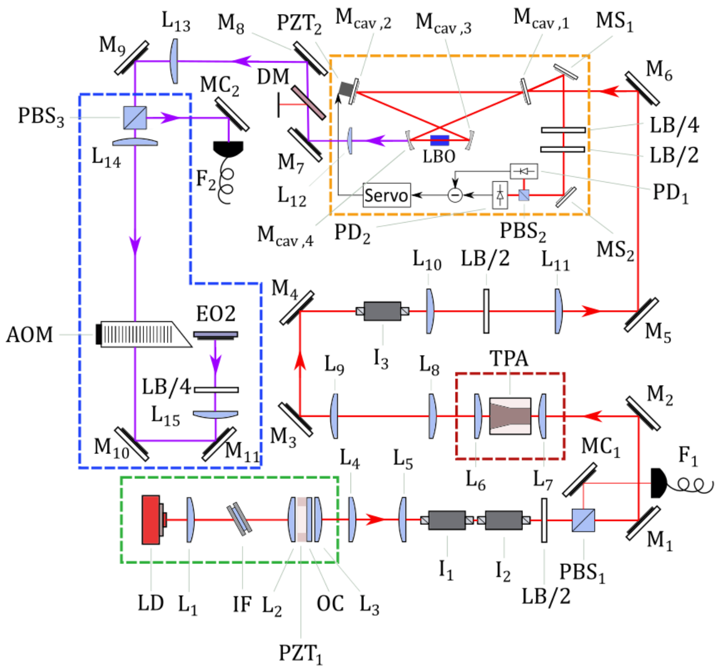

Figure 5.1.: Schematic Layout of the experimental setup which consists of four main parts: An external-cavity diode laser (ECDL) (green dashed frame) , an tapered amplifier (TPA) (red dashed frame) , a bow-tie cavity (orange dashed frame) and a double-pass AOM (blue dashed frame). For the abbreviations of the used components see table 5.1.

Table 5.1.: Summary of used devices.

Label	Device	Supplier	Product specification
LD	AR coated laser diode	eagleyard Photonics	EYP-RWE-0840-06010-1500-SOT02-0000
L_1	Aspheric lens	THORLABS	A230TM-B
L_2	Aspheric lens	THORLABS	A220TM-B
L_3	Aspheric lens	THORLABS	C260TMD-B
L_4	Spherical lens	Casix	–
L_5	Spherical lens	Casix	–
L_6	Aspheric lens	THORLABS	A230TM-B
L_7	Aspheric lens	THORLABS	A375TM-B
L_8	Cylindrical lens	THORLABS	LJ1695RM-B
L_9	Cylindrical lens	THORLABS	LK1753L1-B
L_{10}	Cylindrical lens	THORLABS	LJ1144L1-B
L_{11}	Cylindrical lens	THORLABS	LJ1363C1-B
L_{12}	Cylindrical lens	THORLABS	LJ1567L1-A
L_{13}	Cylindrical lens	THORLABS	LJ1363RM-A
L_{14}	Plano-convex lens	THORLABS	LA1433-A
L_{15}	Plano-convex lens	THORLABS	LA1433-A
M_1	Mirror	unknown	–
M_2	Mirror	unknown	–
M_3	Mirror	unknown	–
M_4	Mirror	unknown	–
M_5	Mirror	unknown	–
M_6	Mirror	unknown	–
M_7	Mirror	Casix	45° 425/626
M_8	Mirror	Casix	45° 425/626
M_9	Mirror	Casix	45° 425/626
M_{10}	Mirror	Casix	45° 425/626
M_{11}	Mirror	Casix	45° 425/626
$M_{cav,1}$	Mirror	Laseroptik	$r_{red} = 0.99$
$M_{cav,2}$	Mirror	Laseroptik	$r_{red} > 0.999$
$M_{cav,3}$	Mirror	Laseroptik	$r_{red} > 0.999$
$M_{cav,4}$	Mirror	Laseroptik	$r_{red} > 0.999$, $r_{blue} = 0.9$
MS_1	Mirror	Laseroptik	–
MS_2	Mirror	Laseroptik	–
MC_1	Mirror	unknown	–
MC_2	Mirror	Casix	45° 425/626
F_1	Fiber	THORLABS	P1-780PM-FC-1
F_2	Fiber	THORLABS	P1-405BPM-FC-1
I_1	Optical Isolator	THORLABS	IO-5-850-VLP
I_2	Optical Isolator	THORLABS	IO-5-850-VLP

I_3	Optical Isolator	unknown	–
PBS_1	Polarizing beam splitter	unknown	–
PBS_2	Polarizing beam splitter	unknown	–
PBS_3	Polarizing beam splitter	THORLABS	PBS101
PD_1	Photo diode	THORLABS	FDS100
PD_2	Photo diode	THORLABS	FDS100
PZT_1	Piezo electric actuator	THORLABS	PQ91JK
PZT_2	Piezo electric actuator	THORLABS	PQ91JK
LB/2	$\lambda/2$-waveplate	THORLABS	–
LB/4	$\lambda/4$-waveplate	THORLABS	–
IF	Interference filter	RADIANT DYES LASERS	custom made
OC	Outpout coupler	LAYERTEC	Output Coupler 108216
TPA	Tapered amplifier	eagleyard Photonics	EYP-TPA-0830-01000-4006-CMT04-0000
LBO	Lithium triborate crystal	RAICOL CRYSTALS	no specification
AOM	Acousto-optical modulator	Gooch & Housego	3100-125
E02	Broadband dielectric mirror	THORLABS	BB1-E02
DM	Dichroic mirror	THORLABS	DMSP550

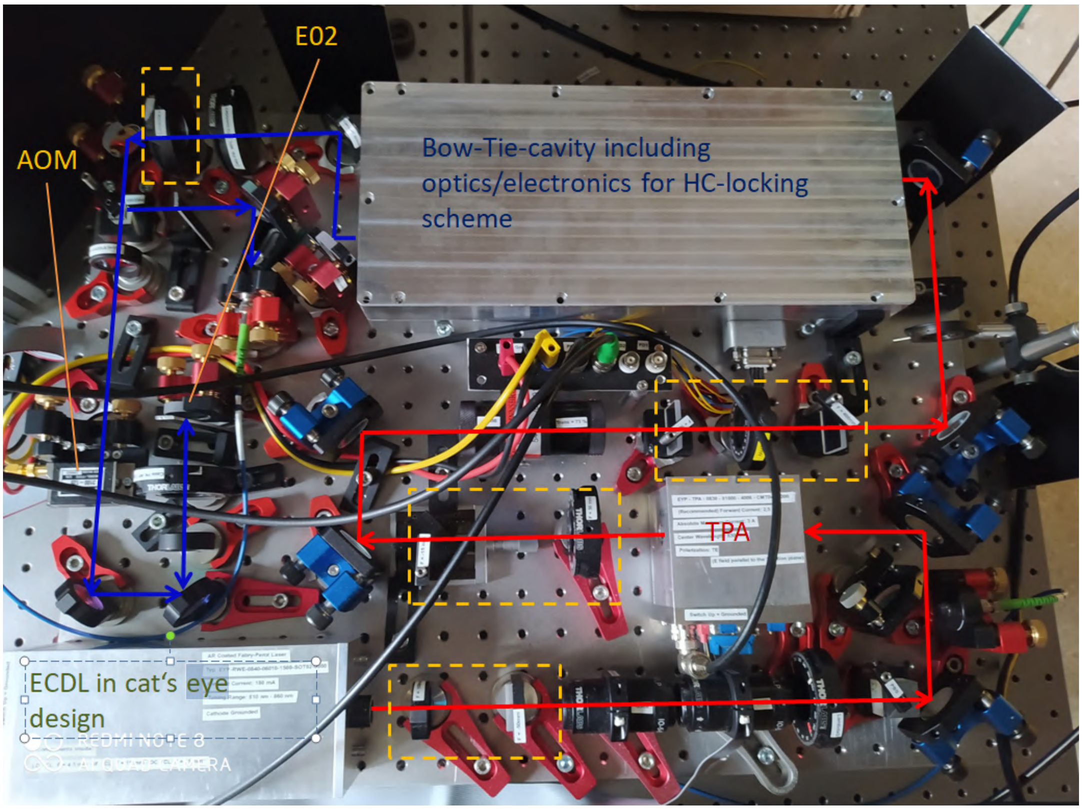

Figure 5.2.: Picture of the whole laser setup. Red arrows indicate the direction of the light before the SHG process. Blue arrows indicate the direction of the light after the SHG process. Orange dashed frames show the optics used for beam shaping.

5.1. ECDL in Cat's Eye Design

Laser diodes became one of the most important electro-optical devices in experimental physics. Applications range from atomic physics, metrology to telecommunication. Many of these areas of application, including this experiment, have one thing in common: they require single mode operation with a narrow line width and good tunability [34].

To provide single mode operation an external cavity is needed. In the common Littrow and Littman-Metcalf configurations diffraction gratings are used for wavelength selection. Both designs require a very precise alignment and are therefore sensitive to acoustic and mechanical disturbances [35]. A further disadvantage is that the direction of the output beam depends on the wavelength. Better robustness and wavelength independent output direction can be achieved by the use of narrow-band dielectric interference filters (IF) which can easily used in an external cavity [34].

Such a IF can easily be combined with a so called cat eye reflection geometry. This configuration is self-aligning and inherently mechanically robust. A sketch of the cat eye configuration is shown in figure 5.3.

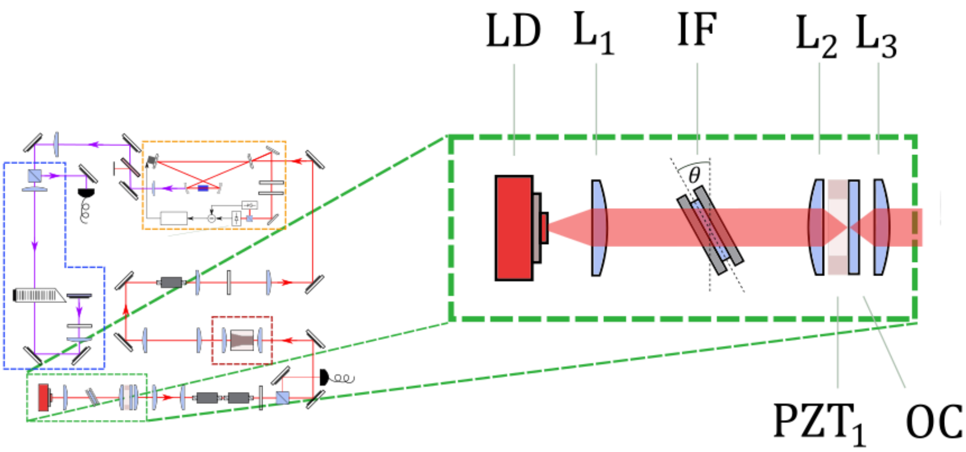

Figure 5.3.: Schematic layout of an external cavity diode laser with cateye geometry consisting of a laser diode (LD), a collimating lens (L_1), an interference filter (IF), an cat eye lens (L_2), a piezoelectric transducer (PZT_1), an output coupler (OC) and an re-collimating lens (L_3). Figure recreated from [35].

5.1.1. Laser Diode

The laser diode (LD) used here is an anti reflection (AR) coated Fabry-Perot laser gain chip [36]. The LD is cathode grounded, which means that the diode's metal case is connected to ground. Due to AR coating the bare LD is not able to lase and it is necessary to build an external cavity upon the diode. The central wavelength is $\lambda = 840\,\text{nm}$ with a tuning range from 810 nm to 860 nm. This allows enough tunability in order to adjust the required wavelength for this experiment. The emitted light of the laser diode is strongly divergent ($\Theta_\parallel = 10°$ and $\Theta_\perp = 23°$ are FWHM values) and hence the beam shows an elliptical profile.

5.1.2. Interference Filter

The wavelength selective element is an interference filter (IF) and is therefore the part of the setup which forces the laser to single mode operation and reduces the linewidth. An IF is made of many dielectric layers between two highly reflecting facets. To understand how an IF works, one can compare the working principle to that of a simple Farby-Perot interferometer (FPI). The transmittance T of an FPI is a function of the finesse $\mathcal{F}$ and the phase shift δ after a round trip within the interferometer. Furthermore, the path difference ΔS of a FPI is a function of the angle of incidence θ. Phase shift δ, path difference ΔS can be related to each other. This means, that by tilting the IF, the transmitted wavelength can be changed. A more detailed description can be found in [17].
Dielectric materials are preferred on metals, because metals have the absorption property,

which increases the temperature of the coating and leads to damage which decreases the reflectance and transmittance of the coating. Dielectric materials instead have very low absorption which do not affect the reflectance and transmittance of the coating [37]. Real IF consist of a multilayer structure instead of a single material. The transmittance spectrum of an IF is slightly temperature dependant. As temperature increases, all layer thicknesses increase. At the same time, all refractive indices change. These effects combine in such a way that the transmittance spectrum shifts slightly to longer wavelengths with increasing temperature [38].
In this setup an IF at a central wavelength of $\lambda = 852\,\mathrm{nm}$ at an rotation angle $\theta = 6°$ is used. By rotation of the IF a tuning range from 855 nm to 834 nm is possible. This allows us to adjust for the desired wavelength needed in the experiment. The IF has a small linewidth of $\Delta\lambda_{\mathrm{IF}} = 0.4\,\mathrm{nm}$ (FWHM) and a transmission from over 90 % for the different wavelengths [39].

5.1.3. Output Coupler and Piezo Electric Transducer

The output coupler (OC) is a mirror which provides the feedback and together with lens (L_2) forms the cat's eye. The OC used in this experiment is from the company LAYERTEC and has a wavelength range of 600 nm to 1000 nm at an angle of incidence of 0°. The OC is flat and round, made of fused silica, has a diameter of $(25.0 \pm 0.1)\,\mathrm{mm}$ and a thickness of $(1.0 \pm 0.1)\,\mathrm{mm}$. The partial reflectance for the specified wavelength range and angle of incidence is $PR = (20 \pm 4)\,\%$ [40]. The parameter PR is the one which determines the feedback. Higher values of PR lead to more feedback, higher values for the finesse and therefore narrower cavity modes but also less output. The vice versa is true for lower values of PR.
To have the possibility to vary the length of the external cavity, a piezo electric transducer (PZT) is attached to the OC.

5.1.4. Lenses

As shown in figure 5.3, three lenses are used for the whole cat's eye setup. As already mentioned, the light emitted by the LD is very divergent. Therefore, the aspheric lens L_1 acts as a collimating lens. This lens has a focal length of $f = 4.51\,\mathrm{mm}$ and a numerical aperture of $NA = 0.55$. This is necessary to collect as much light as possible emitted by the diode.
Lens L_2 and the OC together form the cat's eye. This configuration is supposed to be less sensitive to misalignment, especially if the OC is slightly tilted. Light reflected from a cat's eye will always be parallel to the incident direction. A requirement for this is that the lens-mirror distance has to match the focal length of the lens. In this setup the lens L_2 has a focal length of f = 11 mm. Therefore, the light is always reflected back to the LD.
The last lens of this part of the setup, L_3, is a re-collimation lens and is not part of the external cavity. The only purpose of this lens is to create a collimated laser beam which can be used further on [41]. Figure 5.4 shows a picture of the ECDL.

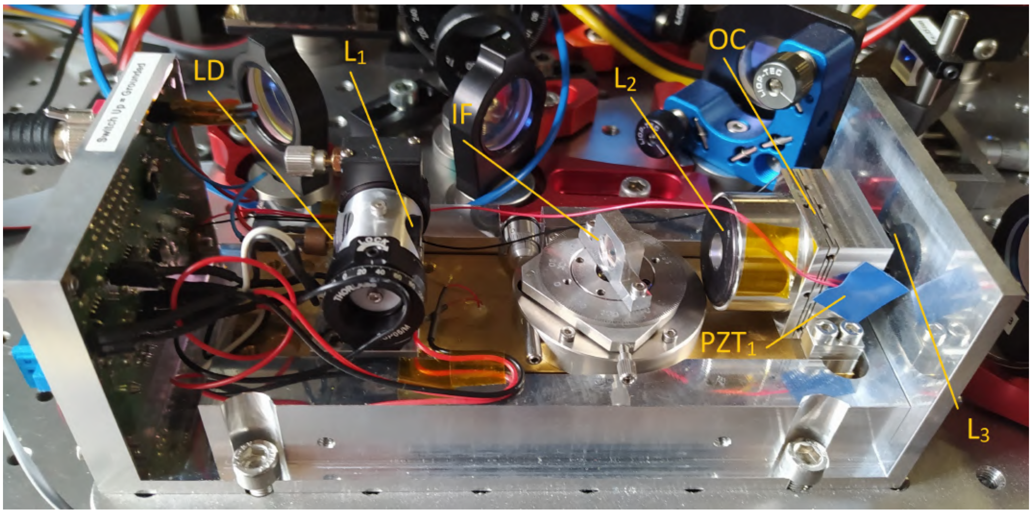

Figure 5.4.: Picture of the ECDL in cat's eye design. Optical elements: laser diode (LD), a collimating lens (L_1), an interference filter (IF), an cat eye lens (L_2), a piezoelectric transducer (PZT_1), an output coupler (OC) and an re-collimating lens (L_3).

5.2. Tapered Amplifier

The output power of an ECDL often lies in the range between 10 mW – 100 mW. A lot of applications in experimental physics, require a much higher laser output power. Furthermore, when performing SHG inside a cavity, only a small fraction of the incident light is converted to the second harmonic frequency. In this case, a tapered amplifier (TPA) can be used to directly amplify the ECDL power output up to approximately 1 W. Usually, the amplification takes place before the output beam goes through a non linear crystal to perform SHG. The reason for this is that most optical devices, such as diodes and amplifiers work fine in the range of red to near infrared radiation, but very badly in the blue regime of the electromagnetic spectrum.

The function principle of a TPA should be discussed only briefly here. For more information consider [42] and [21]. TPA's are in principle ordinary diode lasers with AR coatings on both ends. In ordinary laser diodes the output power is limited due to saturation of the active medium. A TPA overcomes this problem with a tapered gain region which is obtained by electronically pumping. The advantage of this kind of geometry is that the output power increases linearly with length. The difference between a linear and a tapered amplifier is quickly shown in appendix A. The relevant setup for the TPA is shown in 5.5.
The used TPA has a center wavelength of $\lambda_{\mathrm{TPA}} = 830\,\mathrm{nm}$. At an operational current of $I_{\mathrm{TPA}} = 2.5\,\mathrm{A}$ the output power should be $P_{\mathrm{out,TPA}} = 1\,\mathrm{W}$. The input power ranges from $P_{\mathrm{input}} = 10\,\mathrm{mW}$ - $50\,\mathrm{mW}$. If no power is seeded into the TPA while operation, the device can be damaged.
Lenses L_4 and L_5 together form a telescope and are used to shape the beam dimensions of the light emitted by the ECDL to those needed to perform an optimum coupling

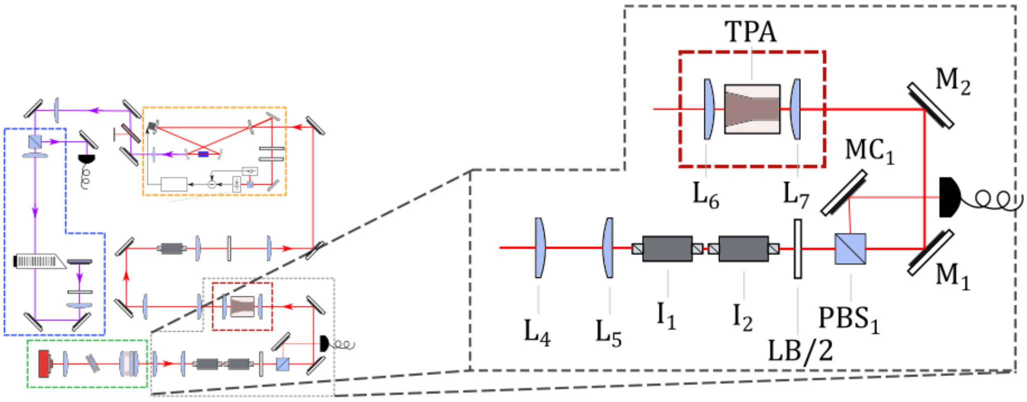

Figure 5.5.: Amplification setup. L_4 and L_5 are cylindrical lenses, I_1 and I_2 are optical isolators, LB/2 is a $\lambda/2$-waveplate, PBS_1 is a polarizing beam splitter, M_1 and M_2 are mirrors for a wavelength of 852 nm, TPA is the tapered amplifier, L_7 is an aspheric lens used to focus the light into the TPA and L_6 is an aspheric lens used to collimate the light after the TPA.

into the TPA. As mentioned in the previous section, the light emitted by a LD is rather elliptical than round. By observing the spontaneous emission of the TPA at the side where the light is coupled in, one can measure the needed beam dimensions. The optical isolators I_1 and I_2 avoid that TPA radiation due to spontaneous emission enters the ECDL. The used TPA requires that the polarization is parallel to the junction plane. To adjust this polarization a $\lambda/2$-waveplate (LB/2) is used. The polarizing beam splitter PBS_1 is used to couple some of the light into a fiber. This light can then be used for measuring the emitted wavelength of the ECDL. Mirrors M_1 and M_2 can simply be used to optimize the coupling of light into the TPA. Lens L_7 is focusing the light on the TPA chip and lens L_6 is used for a first collimation of the TPA output.

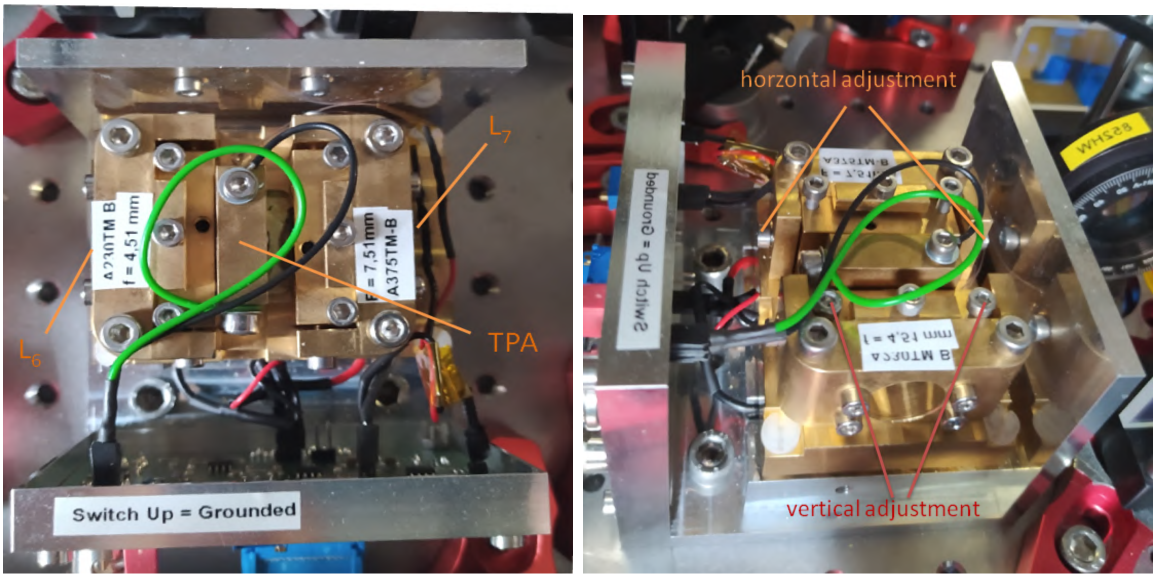

Figure 5.6.: Pictures of the TPA including housing for temperature stabilization. Left picture: TPA, focusing lens L_7 and re-collimating lens L_6. Right picture: Both lenses can be adjusted vertically and horizontally by a pair of screws. For the lens L_7 the screws for horizontal adjustment are marked and for lens L_6 the screws for vertical adjustment are marked.

5.3. Bow-Tie Cavity

This section deals with the heart of the setup, the bow-tie cavity. The bow-tie cavity and the locking setup is illustrated inside the orange frame od figure 5.7. In order make the bow-tie cavity work properly and hence obtaining a large amount of second harmonic generated power the beam coming directly from the TPA has to be mode matched to the cavity. All needed optical elements lie outside and before the orange frame. The cavity then has to be aligned carefully and the outgoing beam made circular so that it can be used for the realization of the double-pass AOM. The optical elements used for circularizing the beam lie outside and after the orange frame.

5.3.1. Mode Matching

In section 3.5 the consequence of the used curved mirrors, $M_{cav,3}$ and $M_{cav,3}$, and the associated astigmatism inside the cavity was explained. Figure 3.6 showed the effect of astigmatism of the bow-tie cavity resulting in different values for the tangential and sagittal waists. The used parameters (dimensions of the cavity and crystal, refraction index of the crystal and so on) already correspond to the real setup. The curved mirror separation is $d_2 = 11.4\,\text{cm}$. For this value figure 3.6 shows a beam waist for the sagittal plane of $w_S = 298\,\mu\text{m}$ and for the tangential plane of $w_T = 266\,\mu\text{m}$ in the middle of the two flat mirrors. To achieve good mode matching the beam arriving from the TPA has to be adjusted in such a way that its waist correspond to these values. Otherwise some portion of the light gets lost inside the cavity due to mode mismatch.

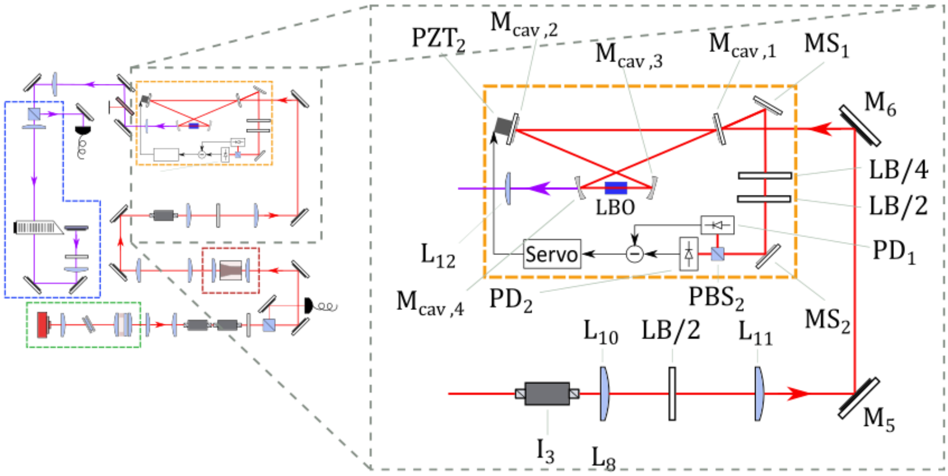

Figure 5.7.: Bow-tie cavity setup including mode matching and circularizing optics. Optics concerning the bow-tie cavity lie inside the orange frame. Optical elements L_8 - L_{11}, M_3 - M_6, I_3 as well as a LB/2 are used for mode matching and guiding the beam into the cavity. Optical elements L_{12} - L_{13}, M_7 - M_9 and DM are used for further beam adjustments.

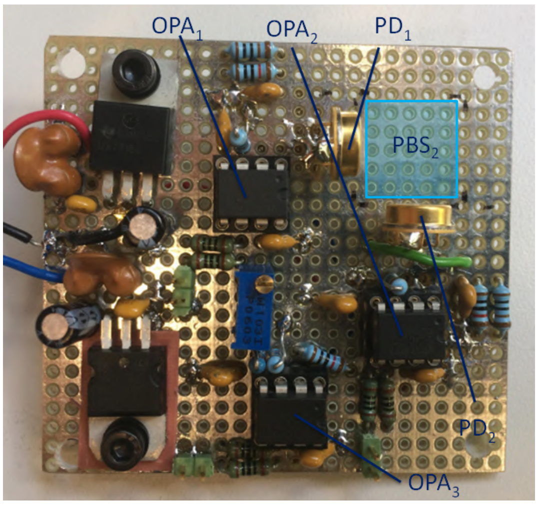

Figure 5.8.: Picture of the electronics employed in the Hänsch-Couillaud locking scheme. PBS_2 is separating the two different polarizations which are measured by the photodiodes PD_1 and PD_2. OPA_1 and OPA_2 are operational amplifiers in order to realize a low pass (each connected on of the diodes) and OPA_3 is used to realize a differential amplifier.

5.3.2. Bow-Tie Cavity Configuration

The whole bow-tie configuration, shown inside the orange frame of figure 5.7, consists of the cavity itself as well as a scheme for locking the cavity to the laser. Light is

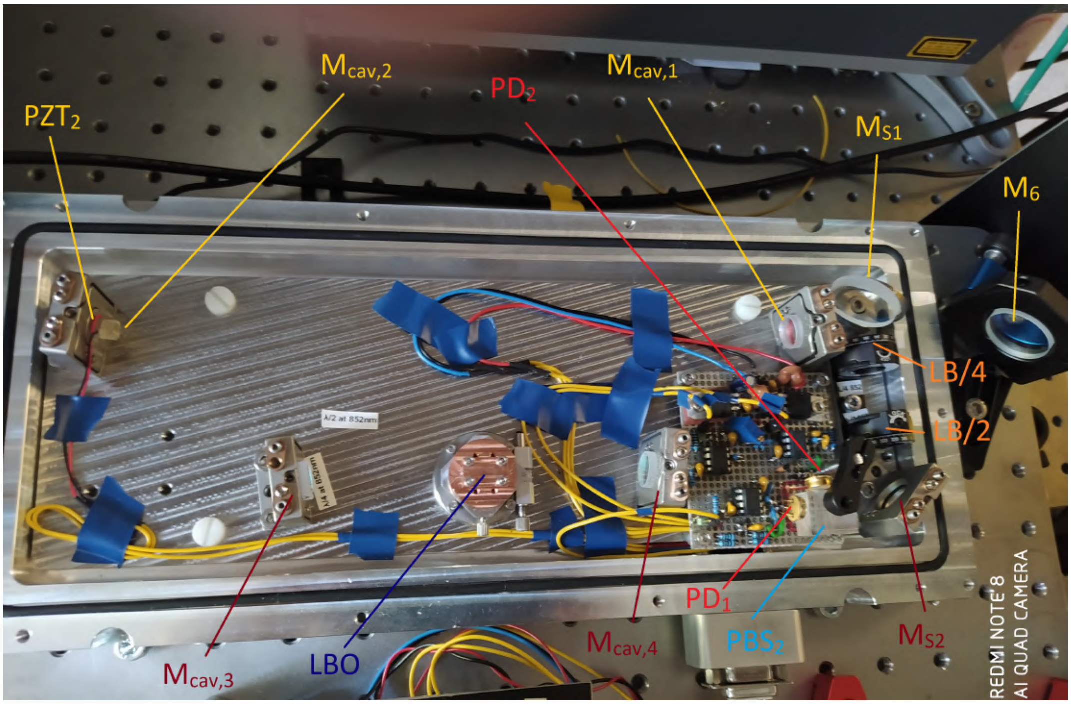

Figure 5.9.: Picture of the bow-tie cavity.

entering the cavity through the input coupler $M_{cav,1}$. It hits then mirror $M_{cav,2}$ which has a piezo electric transducer PST_2 attached. The mirror $M_{cav,3}$ guides the light through the LBO crystal where the SHG takes place. The LBO crystal is a birefringent crytsal and hence is able to separate the components of the incoming electric field into a parallel and perpendicular part with respect to the transmission axis. Thus, the LBO crystal takes the role of the polarizing element in the Couillard-Hänsch locking scheme explained in section 4.5.2. The dichroic mirror $M_{cav,4}$ is high reflective for the IR part of the spectrum but transmits most of the blue light. Therefore, the cavity is closed to achieve a high power enhancement for the incoming wavelength while the second harmonic generated light is able to leave the cavity.
Due to the very high powers inside the cavity (of the order of 20 W), some of the light is leaking through the input coupler. Figure 5.9 shows a picture of the bow-tie cavity.

5.3.3. Alignment of the Cavity

Adjusting a bow-tie cavity such that the beam inside overlaps after a round-trip is not so easy when doing it the first time. Therefore, a short instruction is given how to adjust the cavity. Doing so, it is also very easy to determine the power enhancement inside the cavity. The following steps can help to adjust the cavity:

- Remove the input mirror $M_{cav,1}$. This corresponds to the left situation of figure 5.10.

- Using mirrors M_5 and M_6 to make sure that the laser beam is travelling horizontally and hits mirror $M_{cav,2}$ in the center.

- Using $M_{cav,2}$ and $M_{cav,3}$ in order to make the beam passing through the center of the LBO crystal.

- If no blue light is visible, slightly rotate the crystal. When some light is detected by the photo detector (PD), the measured power P_0 (a few μW) should be optimized by adjusting mirrors $M_{cav,2}$ and $M_{cav,3}$.

- Once P_0 is optimized, mirrors $M_{cav,2}$ and $M_{cav,3}$ are no longer changed. The input mirror $M_{cav,1}$ is put back in place. This corresponds to the right situation of figure 5.10.

- Due to complete misalignment of the cavity no light is detected anymore.

- To make the beam overlap after one round trip only mirrors $M_{cav,1}$ and $M_{cav,4}$ are used.

- When the cavity is aligned, the bue light returns and P_1 should be in the mW range. By using all possible degrees of freedom (including M_5 and M_6) this power should be optimized as much as possible.

- It is necessary to use a blue-filter for the power measurements, because due to the high power of circulating light inside the cavity (several Watts), relatively much of it gets detected by the photo detector.

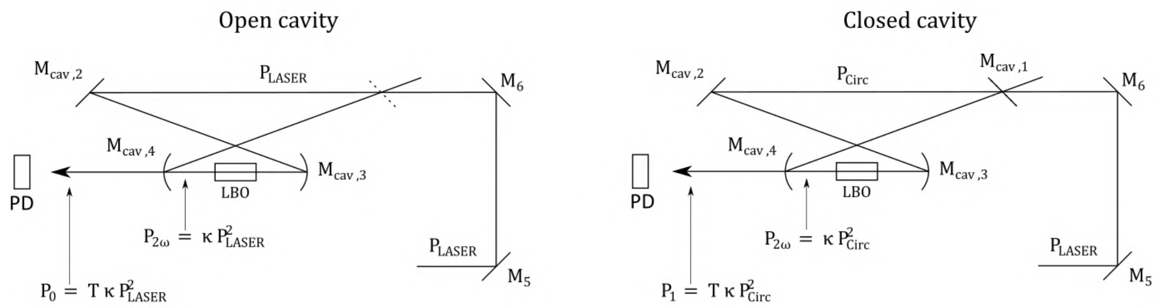

Figure 5.10.: Procedure to align the bow-tie cavity. First the input mirror $M_{cav,1}$ is removed which leaves the cavity open (left situation). The closed cavity consists of all four cavity mirrors $M_{cav,1}$, $M_{cav,2}$,$M_{cav,3}$ and $M_{cav,4}$ (right situation). M_5 and M_6 are mirrors outside the cavity (see figure 5.1), PD is a photo detector and LBO denotes used nonlinear crystal. P_{LASER} is the power entering the cavity, P_{Circ} is the circulating power in case of a closed and optimized cavity, $P_{2\omega}$ is the second harmonic generated power behind the crystal and P_0 and P_1 are the powers reaching the PD for the closed and the open cavity situation, respectively. T is the transmittance of the mirror $M_{cav,4}$ and κ is the second harmonic conversion coefficient.

With the two cavity configurations shown in figure 5.10 the circulating power inside the cavity can be estimated. In the case of an open cavity the second harmonic generated power corresponds to $P_{2\omega} = \kappa P_{\mathrm{LASER}}^2$. The transmittance of mirror $\mathrm{M}_{\mathrm{cav},4}$ is denoted with T so that $P_0 = T\kappa P_{\mathrm{LASER}}^2$ reaches the photo detector (PD). In a second step the cavity is closed by putting mirror $\mathrm{M}_{\mathrm{cav},1}$ back in place again. After the cavity is aligned the circulating power P_{Circ} goes through the crystal and the power reaching the PD is $P_1 = T\kappa P_{\mathrm{Circ}}^2$. The power enhancement inside the cavity is given by $E_{\mathrm{power}} = \frac{P_{\mathrm{Circ}}}{P_{\mathrm{LASER}}}$. By measuring the power P_0 and P_1 the enhancement factor can be calculated according to

$$E_{\mathrm{power}} = \sqrt{\frac{P_1}{P_0}}. \tag{5.1}$$

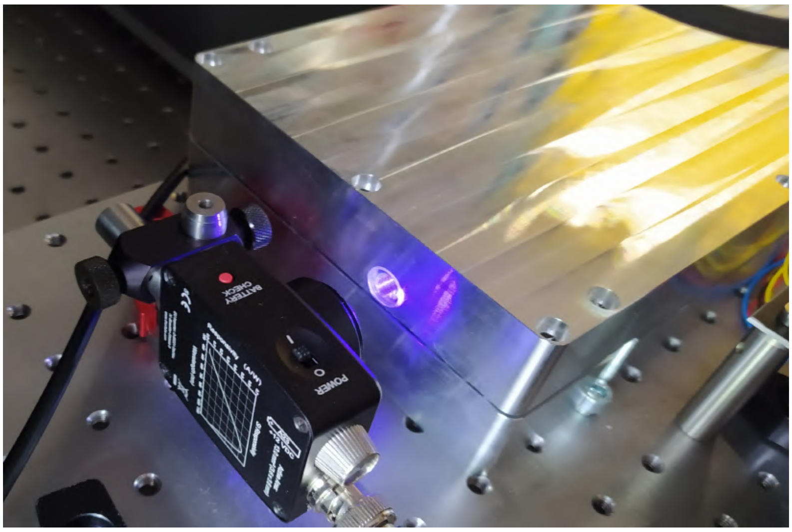

Figure 5.11.: Picture of bow-tie cavity and photodetector DET36A. After proper alignment of the bow-tie cavity, the non visible IR radiation is changed into visible radiation with twice of the fundamental frequency.

5.4. Double-Pass AOM

5.4.1. AOM Function Principle

The acousto optic modulator (AOM) is a device which allows to modulate the frequency, intensity and direction of optical beams by the amplitude of an electrical RF-signal. In our application, intensity modulation is requested to provide the STIRAP laser pulses. The AOM consists of a rectangular crystal bar with high refraction index. At the front side of the bar a piezo actuator is attached. With this electrically excited piezo actuator, sound waves are generated and are travelling across the crystal. A consequence of these sound waves is a refraction index modulation in the crystal. The back side of the crystal bar is slanted to avoid standing sound waves in the crystal.

The electrical AOM-input is impedance-matched to avoid electrical reflections on the RF-cable. The optical beam is crossing the crystal perpendicular to the sound waves. The interaction of sound and light can be explained in a classical wave picture as well as in an quantum mechanical picture [17, 43].
The quantum interpretation is more intuitive to understand. In an optical wave with frequency ω and wave vector $\mathbf{k}$, photons carry energy $\hbar\omega$ and momentum $\hbar\mathbf{k}$. In the same way, in an acoustic wave of frequency Ω and wave vector $\mathbf{K}$, the acoustic quanta called phonons, carry energy $\hbar\Omega$ and momentum $\hbar\mathbf{K}$. The interaction of light and sound results in a scattering processes and is described in first order by the energy momentum relations

$$\begin{aligned} \omega_{\mathrm{d}} &= \omega_{\mathrm{i}} \pm \Omega \\ k_{\mathrm{d}} &= k_{\mathrm{i}} \pm K \end{aligned} \tag{5.2}$$

where the subscripts d,i are indicating whether the corresponding photon is incident or diffracted. The relative orientations of the photon and phonon wave vectors decide if the sign is positive or negative. For optimum scattering into the $+1^{st}$ or -1^{st} order the Bragg condition

$$\sin\theta_{\mathrm{B}} = \frac{K}{2k_{\mathrm{i}}} \tag{5.3}$$

has to be fulfilled. The angle of the incident photon and the diffracted photon are equal to the Bragg angle in this optimum situation, hence $\theta_{\mathrm{B}} = \theta_{\mathrm{i}} = \theta_{\mathrm{d}}$. It is important to note that equation 5.3 does not includes boundary effects of the acousto-optic medium [43].
The used AOM is made for a wavelength of $\lambda_{\mathrm{AOM}} = 470\,\mathrm{nm}$ and modulates the frequency of the optical beam by an applied RF signal of 100 MHz. If operating in the Bragg regime, the interaction of the sound wave, generated by a RF driver connected to a piezo-electric transducer (incorporated in the AOM), with the optical wave causes Bragg diffraction. For the stated wavelength, the first order diffracted light is deflected by twice the Bragg angle $\theta_{\mathrm{d}} = 2\theta_{\mathrm{B}} = 11.2\,\mathrm{mr}$. With a beam diameter of 1 mm the AOM has a diffraction efficiency of 85 % and a rise time of 159 ns. Since the wavelength of the light entering the AOM is smaller than λ_{AOM}, we expect to loose a few percent of diffraction efficiency. Furthermore, to realize the STIRAP process efficiently, very fast pulses in the range of a few ten's of nanoseconds are needed. The rise time is defined as the time the signal needs to rise from 10 % to 90 % of it's maximum and depends on the beam diameter d according to

$$t_{\mathrm{R}} = 0.65\frac{d}{v_{\mathrm{S}}} \tag{5.4}$$

where v_{S} is the speed of sound in the acousto-optic medium. Equation (5.4) is only valid for a TEM_{00} beam and the appearance of the prefactor is explained in appendix C. To reduce the rise time to 16 ns, we have reduced the optical beam diameter to approximately to 0.1 mm. Equation (5.3) is based on the assumption of plane waves. This is true for the acoustic wave and for the optical wave in the neighbourhood of the beam waist. For a 1 mm diameter beam at a wavelength of 422 nm the rayleigh-length is 18 mm, for a 0.1 mm diameter beam the rayleigh-length is only 0.18 mm. That means that in a crystal with a width and highth of 2 to 4 mm the plane wave assumption is true only for 1 mm beams but by fare not for 0.1 mm beams. Therefore the AOM efficiency is much lower for smaller beam diameters.

5.4.2. Double-Pass Configuration

Next, the double-pass configuration shall be explained. The advantage of the AOM-double pass configuration against a single AOM is that the direction of the diffracted 1^{st} order beam is independent of the optical and sound-wave frequency. The disadvantage is the necessity of an additional beam-splitter, mirror and $\lambda/2$-wave plate. In addition the efficiency is reduced and the rise time will increase because the optical beam is passing the AOM twice. The configuration for this setup is shown in figure 5.12. After the beam is made circular by using cylindrical lenses L_{12} and L_{13} (figure 5.1) it enters the polarizing beam splitter PBS_3. To obtain a very short rise time, the AOM is placed in the focus of lens L_{14}.

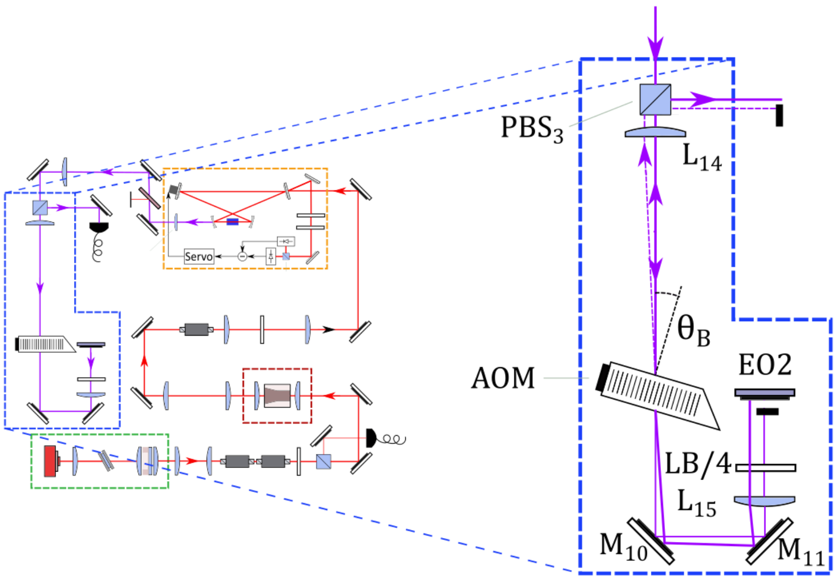

Figure 5.12.: AOM double-pass setup. The frequency doubled light passes through a polarizing beam splitter PBS_3 and is focused into an AOM by lens L_{14}. Optimum diffraction is obtained when the AOM is tilted by the Bragg angle θ_B with respect to the incoming optical beam. A second lens L_{15} is used for recollimation and a $\lambda/4$-waveplate for changing the polarization. A dielectric mirror E02 reflects the first order back which is extracted then by the PBS_3.

Behind the AOM, the incoming beam splits up in a zero order (not diffracted) and a first order diffracted beam. To keep the setup as compact as possible, two mirrors,

M_{10} and M_{11}, are place after the AOM to guide the beams. A second lens L_{15} is used to recollimate the beam. A $\lambda/4$-waveplate is used immediately after L_{15} to change the polarization from horizontal to vertical. The zero order beam is blocked so that only the first order diffracted beam is reflected by the broadband dielectric mirror E02 and passing twice through the AOM. The light which passes twice through the AOM splits up again in a refracted and not refracted portion. Both parts are reflected by the PBS_3, but the portion which is not refracted by the AOM (dashed line in figure 5.12) is blocked. Therefore, the remaining light is shifted in frequency by twice of the acoustic frequency Ω.

6. Characterization of the Setup

In this chapter some basic measurements of the different parts of the setup are shown. This should serve to record the performance at the beginning and as a reference for the future. Furthermore, it is important to check if the setup can deliver the requested power and duration of the laser pulses.
Starting with the cat's eye ECDL, the common power/current and current/voltage curve is measured. Furthermore, the influence of the angle of incidence of the IF is investigated. For the second part, the output power of the TPA against it's operation current is measured for two different seed powers. The biggest part of this chapter deals with the characterisation of the bow-tie cavity. The second harmonic generated light, the mode mismatch, the generated error signal as well as the circulating power inside the cavity and the conversion efficiency are determined. Finally, the double-pass configuration is discussed. AOM performance and rise time are measured.

6.1. Cat's Eye ECDL

We begin to show a few measurements of the Cat's Eye ECDL. The most common LD characteristic is the power/current diagram (left plot of figure 6.1) which plots the output power against the drive current. This curve determines the LD operating point and the current at which the device begins to lase (threshold current). Typically the threshold current increases with increasing temperature. Even for the small temperature range shown in figure 6.1, this behaviour can already be observed. Threshold currents for all three temperatures are shown in table 6.1. The right plot of figure 6.1 shows the current/voltage diagram. This curve is rather insensitive to a change in temperature.
To calculate the threshold current I_{th}, a linear regression $P = a + I \cdot b$ for all three temperatures was performed. The threshold current can be obtained by setting $P = 0$ and hence $I = -\frac{a}{b}$. For better visibility the corresponding linear regressions are not shown in figure 6.1, but all parameters are summarized in table 6.1.

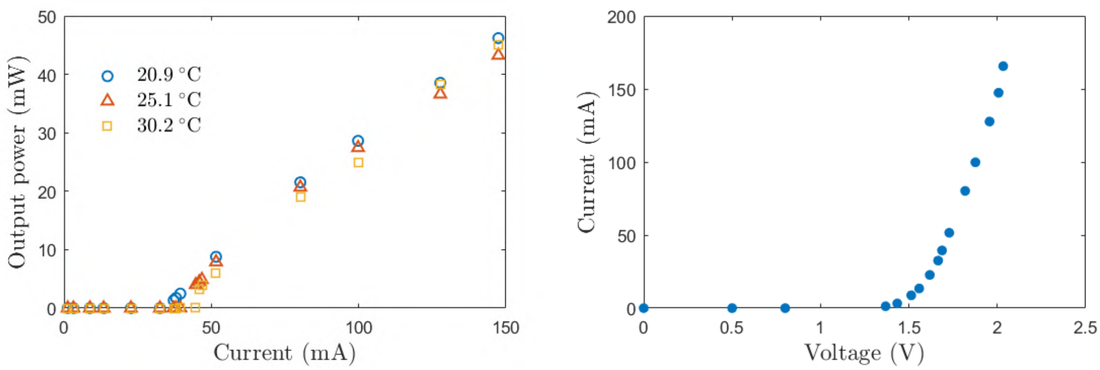

Figure 6.1.: Power/Current characteristics (left) and Current/Voltage characteristics (right). The power/current diagram was measured for different temperatures at a wavelength of λ = 838.4564 nm. The current/voltage diagram was measured at the same wavelength and a temperature of 20.9 °C. Current and Voltage was measured with a multimeter of type UT139B from Uni-Trend Technology. The uncertainty regarding the voltages is estimated to be ± 0.5 %+2 and regarding the current to be ± 1 %+3. The power measurement was performed with an PM100D powermeter and an the S120C power head from THORLABS. Therefore, the uncertainty regarding power is estimated to be ± 3 %. Due to poor visibility, no errorbars are shown.

The next two measurements show the influence of changing the IF incidence angle θ relative to the optical axis. The IF is the wavelength selective element and hence forces the resonator to lase on a single wavelength. The IF has a multilayer structure. By assigning the IF an effective refractive index n_{eff}, it can be modelled as a simple FPI. The left plot of figure 6.2 shows the emitted wavelength of the cat's eye at a certain incidence angle θ. Part of the light (10 μW) were coupled into to a fiber and send to WS6-600 Wavelength Meter to measure the wavelength. The fit function is shown in left plot of figure 6.2. From this the highest transmitted wavelength is obtained and determined to be $\lambda_{\mathrm{max}} = (854.4 \pm 0.4)$ nm. For the effective refractive index a value of $n_{\mathrm{eff}} = 1.75 \pm 0.02$ is obtained. According to [44] $n_{\mathrm{eff}} = 1.7$ is a common value.

Table 6.1.: Obtained fit parameters and calculated threshold current for different temperatures from the power/current diagram shown in figure 6.1. A linear regression $P = a + I \cdot b$ was performed. P is the output power, I the diode current, a the offset and b the slope of the linear regression. Specified errors for a and b resulted by performing a linear fit using MatLab. The specified errors for the threshold current I_{th} was calculated from error propagation. Temperature was obtained from the used temperature controller.

Temperature	Offset a	Slope b	Threshold Current I_{th}
20.9 °C	-13.0(8)	0.41(1)	32(2)
25.1 °C	-18.3(9)	0.49(2)	37(2)
30.2 °C	-18(2)	0.46(3)	39(9)

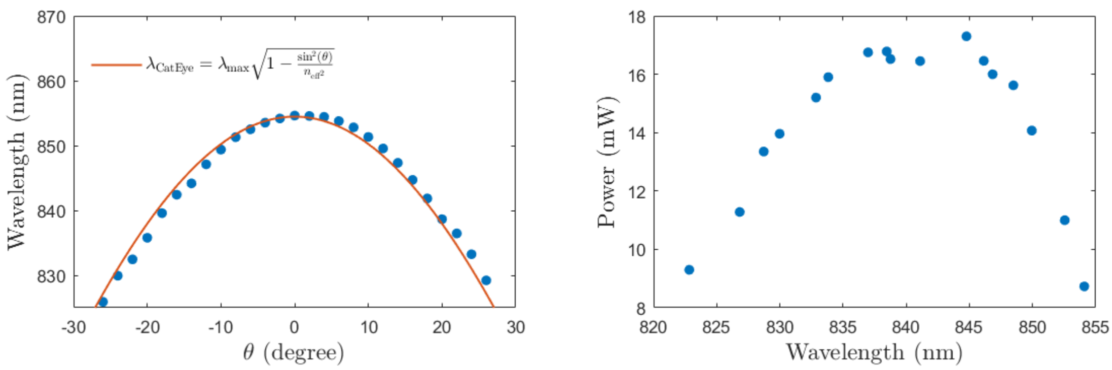

Figure 6.2.: Emitted wavelength against angle of incidence (left) and emitted power against wavelength. By simply rotating the IF the angle of incidence θ was changed by 2° for each measurement. The wavelength was measured by using a WS6-600 Wavelength Meter. The power measurement was performed by using a PM100D powermeter and an The S120C power head from THORLABS. The uncertainty of the angle of incidence is estimated to be ±0.5° due to reading inaccuracy. Power uncertainty is again estimated to be ± 3 %.

The right plot of figure 6.2 shows the output power of the Cat's Eye ECLD versus the corresponding wavelength. One can see that, around a wavelength of $\lambda = 840\,\mathrm{nm}$ the highest power values are emitted. For smaller wavelengths of $\lambda = 835\,\mathrm{nm}$ and for higher ones than $\lambda = 845\,\mathrm{nm}$ the emitted power decreases rapidly. This corresponds with the center wavelength of $\lambda = 840\,\mathrm{nm}$ of the used diode. The power fluctuations around this wavelength come from the measurement, which was performed by holding manually the power head into the laser beam.

6.2. Tapered Amplifier

To seed the TPA properly, the seed laser must be aligned with the TPA's input facet. A measurement of the beam dimensions directly after lens L_3 (figure 5.1) resulted in the following dimensions ($1/e^2$ diameter): $\Delta Y_{\mathrm{Laser}} = 4437\,\mu\mathrm{m}$ (vertical) and $\Delta X_{\mathrm{Laser}} = 2295\,\mu\mathrm{m}$ (horizontal). By operating the TPA without seed (and not exceeding 1 A of TPA current), it's spontaneous emission could be observed. The resulted beam dimensions of the TPA's spontaneous emission ($1/e^2$ diameter) are $\Delta Y_{\mathrm{TPA}} = 1949\,\mu\mathrm{m}$ (vertical) and $\Delta X_{\mathrm{TPA}} = 1055\,\mu\mathrm{m}$ (horizontal). From these values the ratios of $\frac{\Delta Y_{\mathrm{TPA}}}{\Delta Y_{\mathrm{Laser}}} \approx 1/2.3$ and $\frac{\Delta X_{\mathrm{TPA}}}{\Delta X_{\mathrm{Laser}}} \approx 1/2.2$ are determined. The results are summarized in table 6.2. Due to the obtained ratios, two spherical lenses with proper foci are used to shape the dimensions of the beam emitted from the ECDL: f(L_4) = 100 mm and f(L_5) = −50 mm. Lens L_5 is chosen to have a negative focal length to keep the telescope as compact as possible.
The absolute maximum operation current of the used TPA is 3 A. The recommended maximum operation current is 2.5 A. To extend the lifespan of the device, a maximum current of 2.35 A should never be exceeded. It is also very important to choose a fixed

Table 6.2.: Vertical (ΔY) and horizontal (ΔX) beam dimensions emitted from the ECDL and the TPA (spontaneous emission) and resulting ratios.

vertical	horizontal	ratio
$\Delta Y_{\text{Laser}} = 4437\,\mu\text{m}$	$\Delta Y_{\text{TPA}} = 1949\,\mu\text{m}$	$\frac{\Delta Y_{\text{TPA}}}{\Delta Y_{\text{Laser}}} \approx 1/2.3$
$\Delta X_{\text{Laser}} = 2295\,\mu\text{m}$	$\Delta X_{\text{TPA}} = 1055\,\mu\text{m}$	$\frac{\Delta X_{\text{TPA}}}{\Delta X_{\text{Laser}}} \approx 1/2.2$

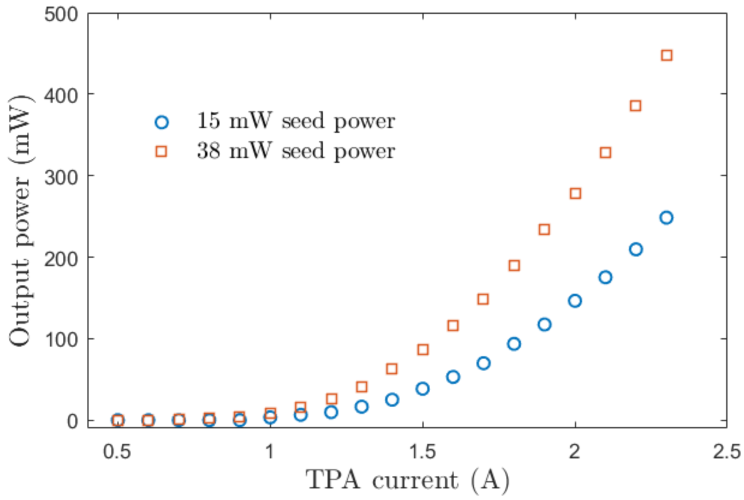

Figure 6.3.: Output power in mW against TPA current in A. Blue circles are measurements with a seed power of $P_{\text{seed}} = 15\,\text{mW}$ and red squares with $P_{\text{seed}} = 38\,\text{mW}$. This corresponds to a LD current of $I_{\text{LD}} = 66\,\text{mA}$ and $I_{\text{LD}} = 132\,\text{mA}$, respectively. The wavelength of the seed for this measurement is $\lambda = 838.4564\,\text{nm}$. Current measured was performed with a multimeter of type UNI-T UT139B and it's uncertainty is estimated to be $\pm$ 1 %+3. The power measurement was performed with an PM100D powermeter and an the S120C power head from THORLABS.

operation current for the device, because this has a decisive influence on the coupling efficiency of the seed. Increasing the current for a specific setting for coupling the seed into the TPA leads to an increase in temperature und therefore to deformations of the TPA chip. This property of the device makes it rather difficult to further increase the current. Once the TPA runs stable, neither it's current or it's coupling settings should be changed. To characterize the TPA, it's output power is measured as a function of the TPA current for two differend seed powers. The power/current diagram of the TPA is shown in figure 6.3. The minimum required seed power for this TPA is $P_{\text{min}} = 10\,\text{mW}$ and the maximum allowed seed power is $P_{\text{max}} = 50\,\text{mW}$. To be sure to stay within this range, the chosen seed powers for this measurement are $P_{\text{seed}} = 15\,\text{mW}$ (blue circles) and $P_{\text{seed}} = 38\,\text{mW}$ (red squares).
As expected figure 6.3 shows that higher values for the seed power leads to higher output powers. The last data point for both measurements was taken at a TPA current of $I_{\text{TPA}} = 2.30\,\text{A}$. For a seed power of $P_{\text{seed}} = 15\,\text{mW}$ (blue circles) an output

power of $P_{\text{out}} = 248.5\,\text{mW}$ resulted. For $P_{\text{seed}} = 38\,\text{mW}$ (red squares) a value of $P_{\text{out}} = 447.6\,\text{mW}$ was obtained. Furthermore, one can observe a linear behaviour between TPA current and output power. This linear relationship seems reasonable, because a TPA is a semiconductor device very similar to that of a laser diode (which is showing such a linear relatioship between current and output power too).
For the next steps the laser diode current is fixed to a value of $I_{\text{LD}} = 135\,\text{mA}$, which corresponds to a seed power of $P_{\text{seed}} = 45\,\text{mW}$ as shown in figure 6.3. The TPA current is fixed to $I_{\text{TPA}} = 2.35\,\text{A}$. It is important to fix these two values, because beam dimensions at the output side of the TPA depend on them. With these settings the TPA delivers a output power of $P_{\text{out}} = 530\,\text{mW}$.

6.3. Bow-Tie Cavity

As explained in section 5.3.3, the bow-tie cavity is optimized in order to obtain as much as possible second harmonic generated power. As explained in section 5.3 and shown in figure 5.7, two photo diodes (PD_1 and PD_2) are used to measure the reflected light from the cavity. From this two photo diodes three signals can be obtained: two polarization dependent reflections signals and the error signal obtained by subtracting PD_1 - PD_2. A fourth signal can be measured by placing an additional photo detector right behind mirror $M_{cav,3}$ as shown in figure 5.10. This signal corresponds to the transmitted second harmonic generated light. To obtain a chronological sequence of these four signals, a frequency generator and a DCDC converter are connected to the piezo electric transducer PZT_2 to scan the length of the cavity. Such a scan is shown in figure 6.4.

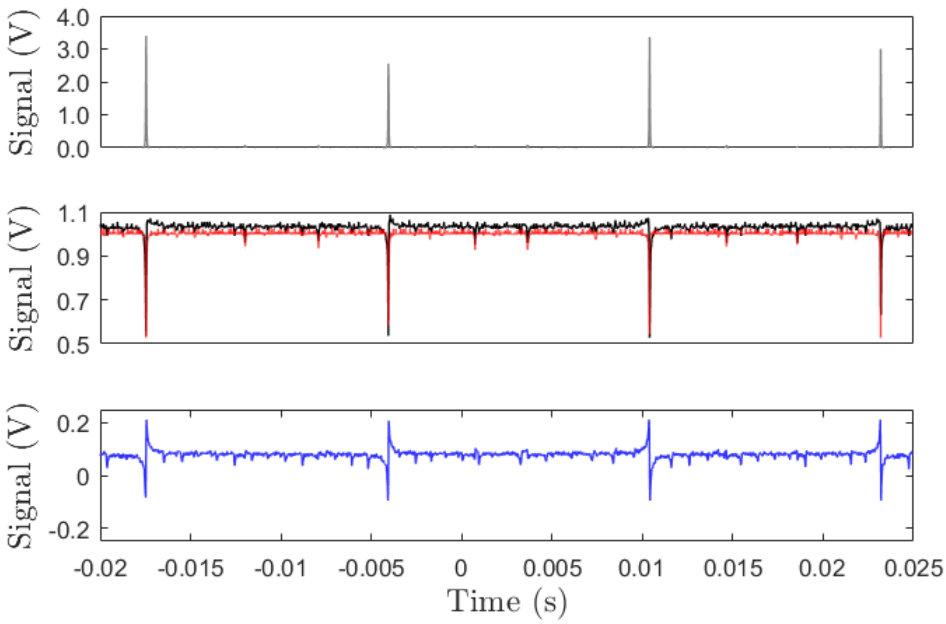

Figure 6.4.: Scan of the bow-tie cavity. Upper plot shows the peaks of second harmonic generated light every time the cavity fulfills the resonance condition. Middle plot shows both photo diode signals that are used to generate the error signal. Lower plot shows the error signal that is feed into a PID controller.

Figure 6.4 shows signals in units of voltage obtained by connecting the photo diodes to an oscilloscope. To achieve this chronological sequence, the cavity was scanned with a frequency of $f_{\text{scan}} = 18\,\text{Hz}$ within a voltage range from $40\,\text{V}$ to $60\,\text{V}$. The upper plot shows the signal of second harmonic generated power. Every time the resonance condition is fulfilled, the circulating intensity inside the cavity is at it's maximum and the most second harmonic generated power is produced. The middle plot shows the the signals corresponding to the reflected light of the bow-tie cavity detected by the photo diodes PD_1 and PD_2. According to the HC locking method, discussed in section 4.5.2, these two signals are then used to create an error signal for locking the cavity to the laser. The error signal, shown in the bottom plot, is then magnified by the control electronics.

6.3.1. Finesse and Second Harmonic Generated Light

By looking closer to the transmission peaks of the bow-tie cavity shown in the upper plot of figure 6.4 it is possible to calculate the finesse and to estimate the obtained second harmonic generated power. Figure 6.5 shows the transmission peaks in more detail.

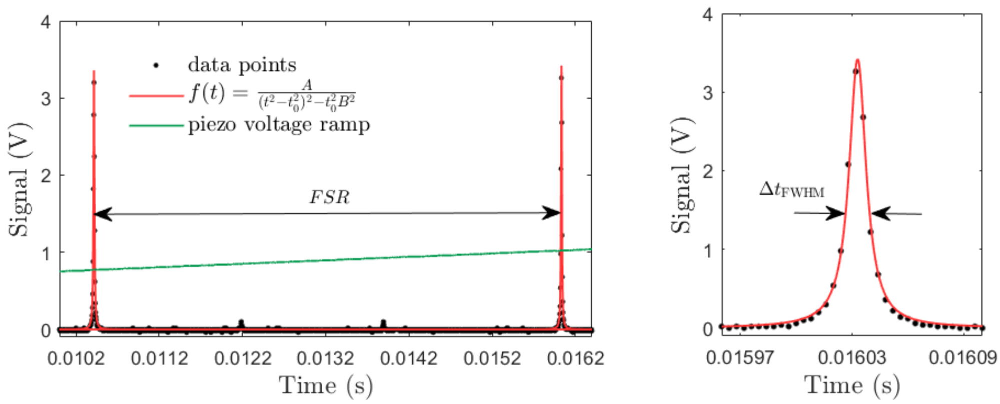

Figure 6.5.: Free spectral range and FWHM of the bow-tie cavity. Left plot: Two consecutive peaks , hence one free spectral range, including the piezo voltage ramp (green line) is shown. Right plot: FWHM of one of the transmission peaks. A Lorentzian function is fitted to the data points (black dots). The function is given inside the left plot, whereas A is a multiplicative constant, B is known as the width and t_0 gives the peak position of the curve.

The left plot shows two consecutive transmission peaks including the piezo voltage ramp which is also used as a trigger signal. To determine the peak positions and hence the free spectral range FSR in units of time a Lorentzian function is fitted to the data points. For the free spectral range in units of time a value of $FSR = 5.6\,\text{ms}$ is obtained. The errors for the peak positions estimated by MatLab lie in the range of 10^{-22} ms for which reason the error for the free spectral range is neglected. The FWHM Δt_{FWHM} in units of time, shown in the right plot, is evaluated for both transmission peaks. This gives values of $t_{0,L} = 1.11 \times 10^{-2}$ ms and $t_{0,R} = 1.33 \times 10^{-2}$ ms for left and right peak, respectively. Again, uncertainties given by MatLab are in the range of 10^{-21} ms. To estimated the FSR properly (which means measuring the time distance of two adjacent peaks) and giving reasonable uncertainties, this measurement is repeated five times. From this $\Delta t_{\text{mean}} = (1.1800 \pm 0.0007) \times 10^{-2}$ ms and $FSR_{\text{mean}} = (5.9 \pm 0.2) \times 10^{-2}$ ms is obtained. The given values consist of mean value and the corresponding standard error. Finally, according to (3.24), a finesse of $\mathcal{F} = 496 \pm 33$ is obtained.
From the maximum value of such a transmission peak it is possible to estimate the

second harmonic generated power.The device to measure the transmission peaks was a DET36A – Si Detector from THORLABS. From the DET36A data sheet we can estimate a responsivity of $Resp = (0.10 \pm 0.02)\,\mathrm{A/W}$ for the blue wavelength at 418.6 nm. To make the detector fast enough to measure the transmission peaks, a $1\,\mathrm{k\Omega}$ resistor is connected in parallel to the input impedance of the oscilloscope. From ten transmission peak values (highest measured data point) an average value of $U_{\mathrm{peak}} = (3.36 \pm 0.12)\,\mathrm{V}$ is obtained. The value consists again of mean value and corresponding standard error. The responsivity of the photo detector gives the produced photo current for a specific incident radiation power.Therefore, the expected second harmonic generated power can be calculated to be

$$P = \frac{U_{\mathrm{peak}}}{R \cdot Resp} = (34 \pm 7)\,\mathrm{mW}, \tag{6.1}$$

where for the resistance R an uncertainty of 5 % was assumed. To verify this result the cavity is locked to the laser according the HC method explained in section 4.5.2. By placing a THORLABS S120C power head behind the bow-tie cavity, a power of $(33 \pm 2)\,\mathrm{mW}$ can be measured which is consistent with the above estimation. The uncertainty of the measured value is due to the uncertainty of the measurement device at the corresponding wavelength.

6.3.2. Reflected Light

The middle plot of figure 6.4 corresponds to the amount of reflected light by the cavity. By looking more closely to one of the photodiode signals that measure x- or y-polarized components, one can estimate how well the mode matching was performed. Figure 6.6 shows one of this signals in more detail.

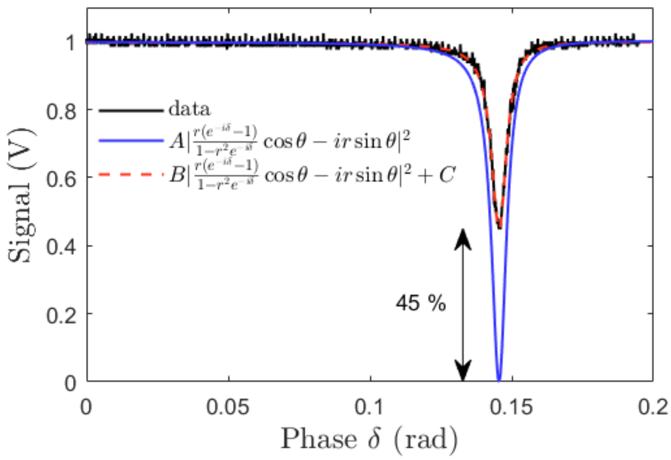

Figure 6.6.: Reflected light from the cavity. The black line shows the real data. The blue line corresponds to the theoretical expectation under impeadance and mode matched conditions [21]. The dashed orange line accounts for the mode mismatch by including an offset C to the fit functions shown inside the plot.

If the cavity is perfectly impeadance matched, one would expected the reflected signal to be zero. However, it is important to note, that a non-zero reflected signal at resonance does not mean that the cavity is not impeadance matched. A finite reflection signal from the cavity can arise when the mode matching was not well performed. In this case not all of the incident power is coupled into the single cavity mode. The portion which is not coupled will be reflected at the input mirror, no matter the cavity is impeadance matched or not. Under impeadance matched and mode matched conditions, the blue line shown in figure 6.6 results. To account for mode mismatch, an offset is added this curve. By fitting the orange dashed line to the data for this offset a value of $C = (44.7 \pm 0.2)\,\%$ is obtained. This means $(55.3 \pm 0.2)\,\%$ of the light is coupled into the cavity. The errors are obtained by a fitting program written with MatLab. The reason that not more light is coupled into the cavity is because the TPA output beam has a very high astigmatism which makes mode matching difficult.

6.3.3. Error Signal

According to the HC locking scheme a dispersive signal is generated which is then amplified by the control electronics and feed to a PID controller. To produce the error signal, a triangle shaped voltage generator, integrated in the Advanced Laser PID electronics (see appendix B.1) is used to find the free spectral range of the bow-tie cavity. This triangle shaped signal is then feed into the modulation input of the HV-DCDC converter. The triangle signal is then superimposed with an offset from the HV-DCDC converter (see appendix B.2) and sent to the piezo electric trancducer mounted on the $M_{\mathrm{cav},2}$ mirror (see figure 5.1) of the bow-tie cavity. This signal is shown in figure 6.7.

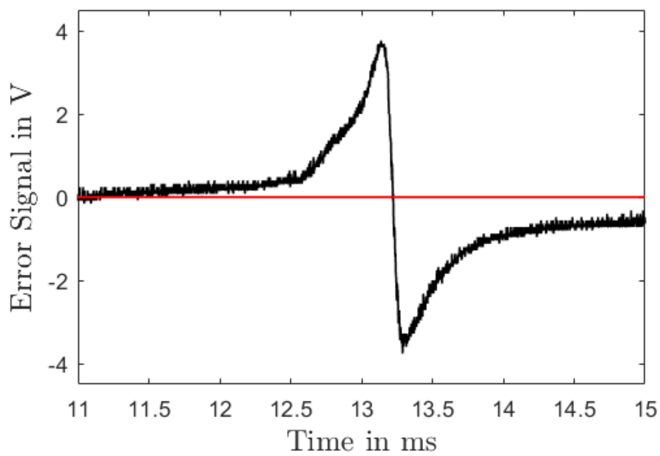

Figure 6.7.: Error signal (black line) after the Advanced Laser PID electronics. The horizontal red line corresponds to 0 V.

The shown signal is qualitative the same as the theoretical error signal from figure 4.8 and the control electronics can be switched from scanning to locking mode. When the

cavity is locked to the laser, the transmission signal is maximal and apart from small deviations the error signal is hold to 0 V.
The ability of the control electronics to keep the cavity locked to the laser can be judged by analyzing the closed loop error signal. A Fourier analysis of this signal gives information of how well the feedback loop is suppressing detected fluctuations at various Fourier frequencies. By using an SR1 Audio Analyzer Stanford Research Systems, the Fourier transformation of the error signal can be performed directly and is shown in figure 6.8.

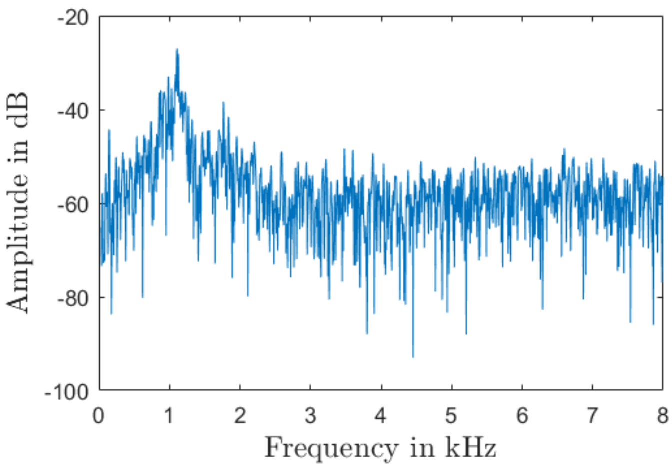

Figure 6.8.: Noise Spectral density of the closed loop system consisting of control electronics and bow-tie cavity.

Figure 6.8 shows that starting from 0 kHz, the ability of the control electronics to suppress fluctuations is getting worse, reaching a maximum around 1 kHz. For higher frequencies the amplitude has a mean value around -60 dB.
When the cavity is locked to the laser, one can see some oscillation of the error signal when making some noise. This oscillation comes from acoustical resonances of the cavity. An example is shown in figure 6.9 which was produced by whistling while the whole apparatus was on. Performing a fit to the data gave a frequency of $\omega = (6234 \pm 3)$ Hz.

6.3.4. Circulating Power inside the Cavity and Conversion Efficiency

Now we will estimate the circulating power inside the bow-tie cavity. This can be done as explained in section 5.3.3 by measuring the transmitted power in an open and closed cavity configuration. The laser beam hitting the cavity coming from the TPA has a power of $P_{\mathrm{inc}} = (350 \pm 11)$ mW. In the open cavity configuration a value of $P_0 = (5.0 \pm 0.3)\,\mu$W for the transmitted power is obtained. In order to not detect also some additional leaking power of red wavelength, a blue filter is positioned in front of the power meter. When the cavity is closed, a tansmitted power $P_1 = (30 \pm 2)$ mW

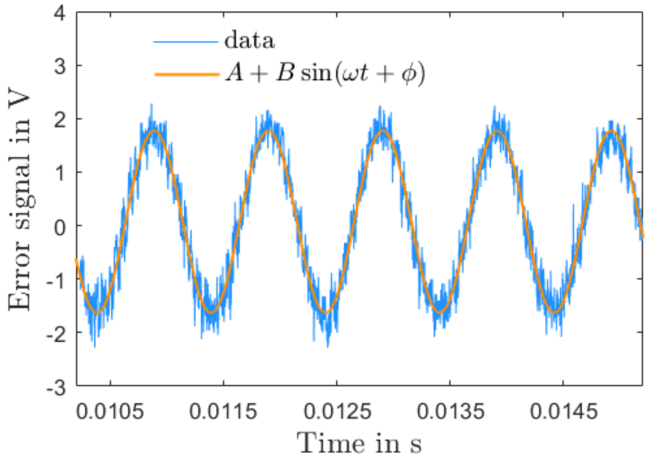

Figure 6.9.: Oscillation of the error signal when making some noise. The fitted function is shown inside the figure: A is an offset, B is the amplitude of the oscillation, ω is the frequency and ϕ some phase.

is measured. Uncertainties arise from the used power meter. According to equation (5.1) a power enhancement of $E_{\mathrm{power}} = 77 \pm 3$ arises. This is already quiet close to the maximum power enhancement shown in figure 3.3 for an impeadance matched cavity. For $P_{\mathrm{inc}} = (350 \pm 11)\,\mathrm{mW}$ this leads to a circulating power inside the cavity of $P_{\mathrm{circ}} = (27 \pm 1)\,\mathrm{W}$.
Next, the dependence of the SHG power as a function of the input power is shown. To calculate the circulating power inside the cavity for different incoming powers, equation (4.25) has to be solved numerically. The nonlinear conversion coefficient from equation (4.23) can be estimated by measuring the single pass conversion efficiency (open cavity configuration) and for the stated values (P_{inc} and P_0) above K is equal to $(4.1 \pm 0.3) \times 10^{-8}\,\mathrm{mW}^{-1}$. Due to mode matching issues not all of incoming light is coupled into the cavity and hence P_{inc} has to be replaced by $\eta_{\mathrm{mode}} P_{\mathrm{inc}}$ where η_{mode} is the mode matching efficiency. From section 6.3.2, η_{mode} is known to be $(55.3 \pm 0.2)\,\%$. Assuming the reflectivity of mirrors $\mathrm{M}_{\mathrm{cav},2}$, $\mathrm{M}_{\mathrm{cav},3}$ and $\mathrm{M}_{\mathrm{cav},4}$ to be $r_{1,2,3} = 0.9990 \pm 0.0005$ and the transmissivity to be $t_{\mathrm{cryst}} = 0.9990 \pm 0.0005$, the theoretical losses inside the cavity are $l_{\mathrm{cav}} = (4.0 \pm 0.8) \times 10^{-3}$. The transmittance of the input coupler is assumed to be $T_1 = 0.010 \pm 0.002$. Figure 6.10 shows measured values of the SHG power output for different input powers and the corresponding theoretical curve.

As one can clearly see, the theoretical curve does not fit with the measured data. By varying the parameters of equation (4.25) it appears that changing l_{cav} has the biggest influence. Therefore, it can be assumed that the losses inside the cavity are different than stated above. A much better result can be achieved by changing the value of l_{cav} from the theoretical one of 4×10^{-3} to 6×10^{-3}. This behaviour is shown in figure 6.11.

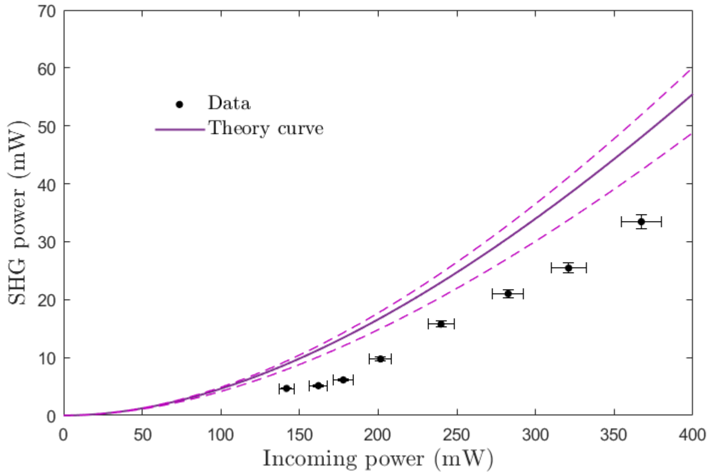

Figure 6.10.: Measured values and theory curve of the SHG inside the bow-tie cavity for the following parameters: $K = (4.1 \pm 0.3) \times 10^{-8}\,\mathrm{mW}^{-1}$, $\eta_{\mathrm{mode}} = (55.3 \pm 0.2)\,\%$, $r_{2,3,4} = 0.9990 \pm 0.0005$, $t_{\mathrm{cryst}} = = 0.9990 \pm 0.0005$ and $T_1 = 0.010 \pm 0.002$.

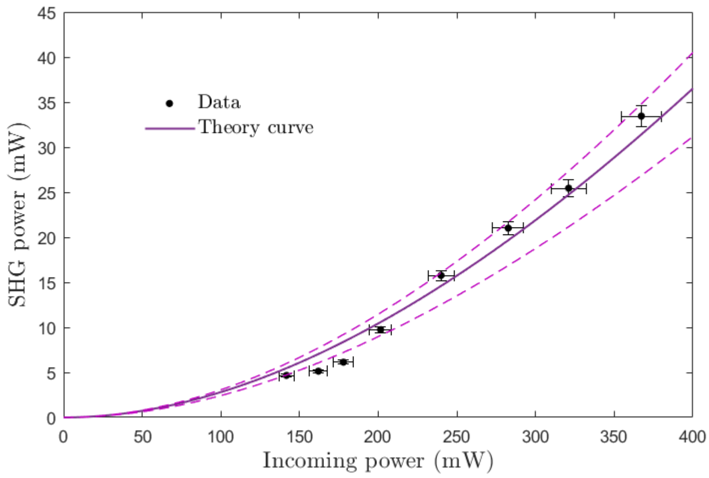

Figure 6.11.: Measured values and theory curve of the SHG inside the bow-tie cavity for the same parameters as used in figure 6.10. The dashed lines correspond to an upper and lower uncertainty of the theoretical curve taking into account the stated uncertainties of the used parameters.

During the time this setup was built, the cavity box has been opened for readjusting the bow-tie configuration several times. When adjusting the cavity, the cavity elements are exposed to the environment and dust deposition on mirrors and on the nonlinear crystal may happen. Especially on the crystal this can lead to sever damage of the AR coating. Furthermore, it cannot be ruled out that the surfaces of the devices have been damaged while placing them in the cavity ord during adjustments. Because of this, it seems reasonable to change l_{cav} to a higher value to make the theoretical curve fit with the measured data. Figure 6.11 shows a conversion efficiency of $(16 \pm 1)\,\%$ at an input power of $(367 \pm 12)\,\mathrm{mW}$.

6.4. Double Pass AOM

6.4.1. Beam Shaping for AOM

To use the laser beam coming from the bow-tie cavity, it is important to shape it circular first. Figure 6.12 shows the beam dimensions (left: horizontal, right: vertical) behind the bow-tie cavity (top), behind lens L_{13} (middle) and after a distance of 50 cm (bottom) from lens L_{13} (bottom).

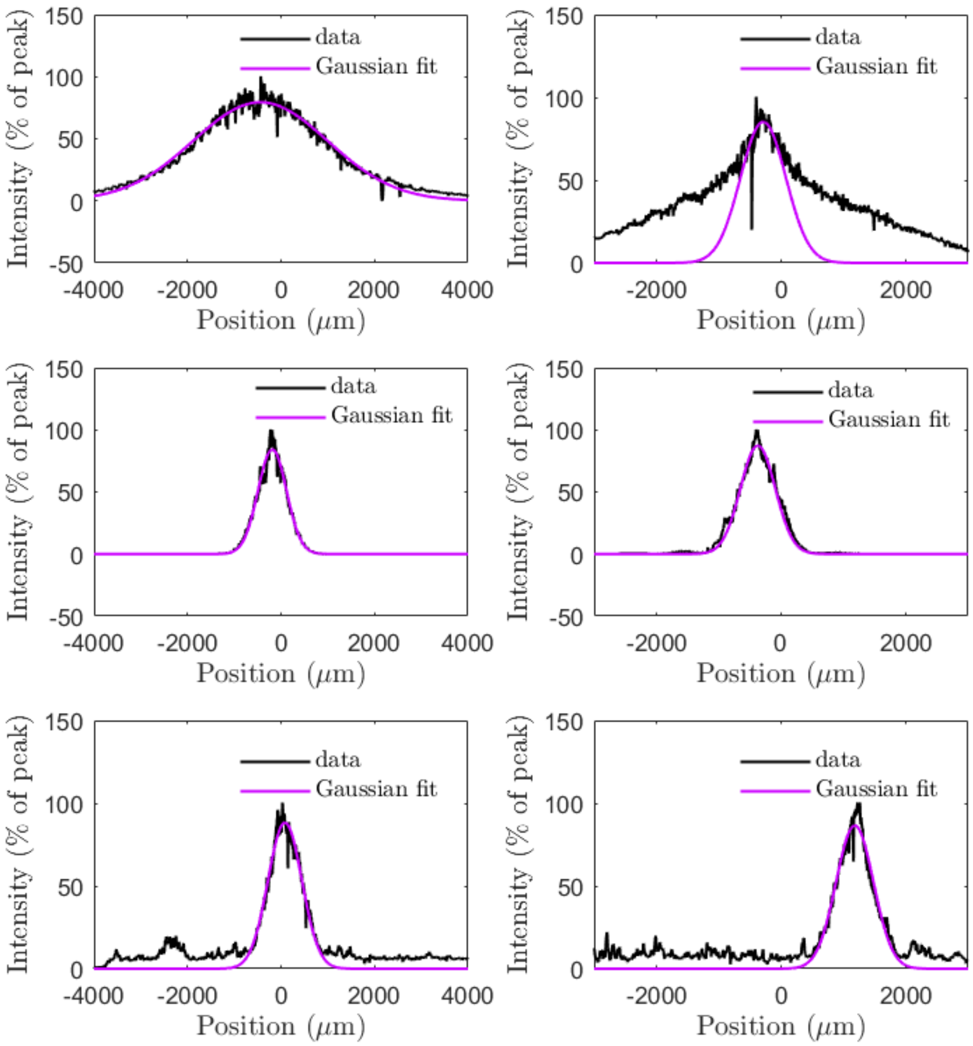

Figure 6.12.: Laser beam dimensions (left column: horizontal, right column: vertical) right after the bow-tie cavity (top), right after lens L_{13} (middle) and after 50 cm from lens L_{13} (bottom).

As one can see from the top two plots, the beam dimensions right after the bow-tie cavity are far away from being circular. The upper left plot shows a nice Gaussian behaviour. The intensity profile for the vertical dimension, shown in the upper right plot, shows a different behaviour. Around the maximum it looks like a Gaussian distribution but then starts to flatten. For the range where the intensity profile looks Gaussian a fit was performed. From fitting both intensity profiles a ratio of 1/3.97 is obtained. This justifies the values of the focal lengths of lenses L_{12} (f = 100 mm) and L_{13} (f = 400 mm).
The middle to plots show the intensity profiles right after lens L_{13}. Again from fitting Gaussian functions to both profiles, a ration of 1/1.09 is obtained which can be considered as a circular beam. The Gaussian beam diameter after L_{13} is approximately 1.3 mm.
To check if the beam stays approximately circular, the intensity profile of both dimensions is measured after a distance of 50 cm from lens L_{13}. This is shown in the two bottom plots of figure 6.12. From the Gaussian beam diameters obtained by fitting, a ration of 1/1.21 is obtained. This shows that beam dimensions change a bit with increasing distance from lens L_{13}, but stay rather circular.

6.4.2. AOM Performance and Rise Time

For the STIRAP transition very short pulses in the sub-hundred nanosecond range are needed. To achieve such short pulses, the rise time, defined in section 5.4.2, needs to be considerable fast. Therefore, lens L_{14} is used to focus the circularized beam to a smaller spot size, such that the beam diameter inside the AOM is smaller than 1 mm which then reduces the rise time given by equation (5.4).
Lens L_{14} has a focus of f = 150 mm which results in beam dimensions of $d_{\mathrm{x}} = 120\,\mu\mathrm{m}$ for the x- and $d_{\mathrm{y}} = 100\,\mu\mathrm{m}$ for the y-direction. This very strong focusing of the beam into the AOM causes diffraction losses, so that the first order diffraction efficiency is far away from the supplier specification. With a power of $P_{\mathrm{inc}} = 23.3\,\mathrm{mW}$, only $P^{1st}_{\mathrm{single}} = 11.6\,\mathrm{mW}$ are diffracted into the first order. This corresponds to an diffraction efficiency of 48.9 %. With the same input power the power in the first order after passing through the double pass is $P^{1st}_{\mathrm{double}} = 5.9\,\mathrm{mW}$. This corresponds to a diffraction efficiency of 26.4 %. Due to limited space it was not possible to implement an additional beam shaping optics to increase fiber coupling efficiency.
Due to this sharp focusing, the beam dimensions behind the double pass change again from circular to elliptic. So after PBS_3 the beam dimensions are $d_{\mathrm{x}} = 629\,\mu\mathrm{m}$ for the x- and $d_{\mathrm{y}} = 1280\,\mu\mathrm{m}$ for the y-direction. Due this elliptical shape of the beam only 55 % could be coupled into a fiber which results than in 3.2 mW power available for the STIRAP transition.
To measure the rise time of the double-pass configuration, the AOM is switched on and off very fast. This switching can be seen in the left plot of figure 6.13. The slightly delay of approximately 180 ns between the RF driver signal (green) and the photodiode signal (black) comes from the time the acoustic wave needs to arrive at the position where the beam travels through the AOM twice.

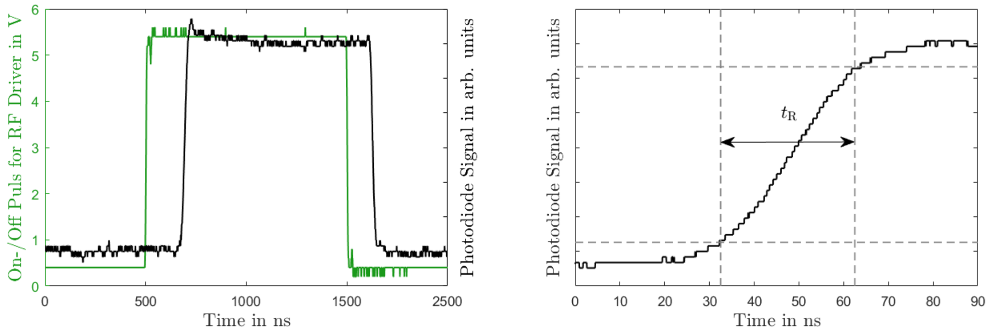

Figure 6.13.: Rise time meaurement of the AOM double-pass configuration. Left plot: RF signal and photodiode signal. Left plot: Photodiode signal on a stretched time scale to make the rise time visible.

The rise time t_{R} can than be measured by a fast photodetector (in this case a 2 GHz photodetector from THORLABS). The measured signal is shown in the right plot of figure 6.13. The horizontal gray dashed lines represent the 10 % and 90 % threshold of the signal. The vertical gray lines are placed at the crossing points of the horizontal ones with the actual signal (black curve). The rise time is estimated to be approximately 30 ns.

6.5. Summary

In this section the whole setup was characterized. The goal of the setup is to produce a reasonable short lasber pulse with enough power for the STIRAP transition from the Dysprosium ground state to the intermediate state at 23 877.75 cm^{-1}.
The first part of the setup is the ECDL in cat's eye design. It could be shown that by rotating the interference filter inside the cavity the desired wavelength of 837.2 nm could be obtained. Furthermore, the ECDL is able to provide the TPA with the required seed power of 10 - 50 mW.
The TPA is the used to amplify this power. It could be shown that the TPA is able to produce easily a power of around 500 mW while not exceeding the maximum TPA current of $I_{\mathrm{TPA,max}} = 2.5\,\mathrm{A}$. Staying below this value might increase the life time of the TPA.
The SHG takes place inside the bow-tie cavity which is needed to build up enough power to make the process more efficient. The mode matching and impeadance matching of the cavity were performed in such a way that $(53.3 \pm 0.2)\,\%$ of the incoming power could be coupled in the cavity. An error signal with an amplitude of approximately 8 V could be produced which is able to lock the laser to the cavity. When the cavity is locked to the laser a total output power of $(33 \pm 2)\,\mathrm{mW}$ could be achieved.
The last part of the setup is the formed by the AOM in a double-pass configuration which is used to shape pulses from the continuous wave laser provided by the bow-tie

cavity. Due to the very sharp focusing into the AOM to achieve fast rise times, the diffraction efficiency dropped to approximately 26.4 %. Another consequence of the focusing is that after the beam passes though the AOM it's not circular any more. The beam dimensions of the beam after the double-pass have a ration of approximately 1:2 which reduces the amount of light that can be coupled into a fiber. At the end of the double-pass configuration a laser pulse with total power of approximately 3 mW and a rise time of 30 ns is available.

7. Transfer Efficiency Simulations for Dysprosium

To get a better feeling what transfer efficiencies one could expect and what pulse parameters (pulse width, pulse delay, peak rabi frequency...) are needed, simulations have been performed. Due to the fact that the STIRAP transition for populating the state $|b\rangle$ at $17\,514.50\,\mathrm{cm}^{-1}$ which involves the intermediate state at $23\,877.75\,\mathrm{cm}^{-1}$ has highly unequal decay rates within the Λ system, the simulations rely on section 2.3.

7.1. Analytical Solution

The STIRAP transition for this experiment connects the Dysprosium ground state and the opposite parity state $|b\rangle$ with an intermediate at $23\,877.75\,\mathrm{cm}^{-1}$. The life time of the intermediate state is $\gamma = 7.9\,\mathrm{ns}$. If we assume that the decay from this intermediate state will mostly occur to the ground state, the decay rate can be assumed to be approximately $\Gamma_1 = 2\pi \times 20\,\mathrm{MHz}$. The reduced dipole moment for the transition from the intermediate state to state $|b\rangle$ is estimated to be $\langle b||\hat{d}||23\,877.75\,\mathrm{cm}^{-1}\rangle = 0.3\,\mathrm{a\,u}$ [45]. Converting this value into SI units and using equation (1.4), a decay rate of $\Gamma_2 = 2\pi \times 0.8\,\mathrm{kHz}$ results. Due to the fact that Γ_1 is several orders of magnitude bigger that Γ_2, a population of the intermediate level would return the population back to the Dysprosium ground state rather than to the target state. In order to simulate this problem the coupled differential equations (2.21) are solved numerically using MatLab. The left plot of figure 7.1 shows the final populations ρ_{33} as a function of time for different pulse widths T. To fulfill the adiabatic criteria (2.14) the pulse area of the Gaussian pulse is kept to a constant value of $A = 50$. The pulse delay in figure 7.1 is set to $\tau = 50\,\mathrm{ns}$ for all pulse widths. For this specific pulse parameters one can see that population transfer efficiencies over 90 % are possible reaching a value close to 100 % for pulses with T = 50 ns.This high transfer efficiencies can be explained due to the fact that in the adiabatic regime the intermediate state is almost not populated and hence spontaneous decay from this state has no big influence on the process. The right plot shows the Gaussian pulses for a pulse width of $T = 100\,\mathrm{ns}$.

Figure 7.2 shows a simulation for different pulse delays τ. The pulse area is again set to $A = 50$ and the pulse width is equal to $T = 100\,\mathrm{ns}$. The simulation then shows that increasing the pulse delay from $\tau = 20\,\mathrm{ns}$ to $\tau = 100\,\mathrm{ns}$ increases the transfer efficiency from about 70 % close to 100 %. Increasing the pulse delay the further more will result in a decrease of transfer efficiency. This is due to the fact that for bigger pulse delays the STIRAP pulses do not overlap well. However, a large overlap of pulses is required

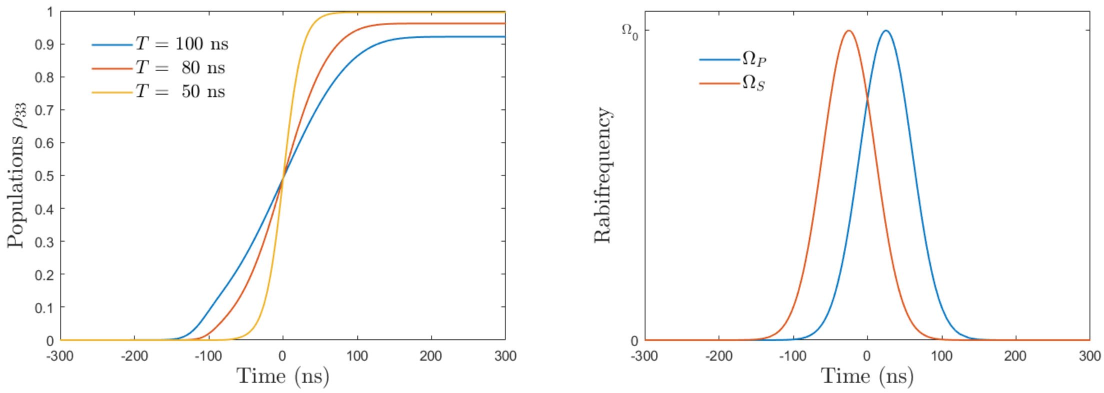

Figure 7.1.: Transfer efficiency for different pulse widths. Left plot: Population ρ_{33} as a function of time for pulse widths T of 50 ns, 80 ns and 100 ns. The pulse are of the Gaussian pulses is kept to $A = 50$ and the pulse delay is set to
$tau = 50$ ns. Right plot: Gaussian pulses as a function of time for pulse width $T = 50$ ns and pulse delay $\tau = 50$ ns.

because the mixing angle $\theta(t)$ stays nearly constant during the overlap. This leads to $\dot{\theta}(t) \approx 0$ and the nonadiabatic couplings during the process do not play a big role. This observation is consistent to the criteria of optimum pulse delays $\tau \gtrsim T$ [13].

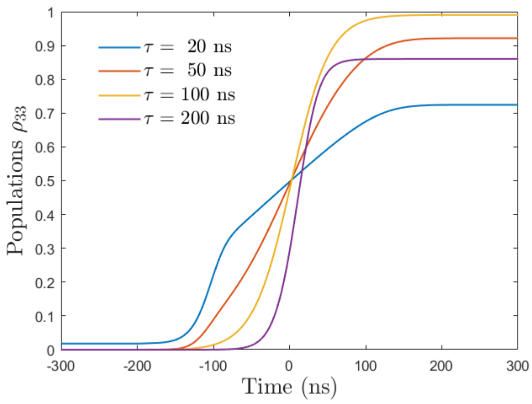

Figure 7.2.: Transfer efficiency for different pulse delays of $\tau = 20$ ns, 50 ns, 100 ns and 200 ns. Pulse area is set to $A = 50$ and the pulse width is $T = 100$ ns.

Lowering the pulse area to $A = 10$ will weaken the adiabatic evolution. The intermediate state gets populate and the spontaneous decay will affect the transfer efficiency. Due to the fact that Γ_1 is much bigger than Γ_2, atoms in the intermediate state will decay more likely to the ground state rather than to the final state and hence this will decrease the transfer efficiency. This is shown in figure 7.3. The situation is quiet the same as in the left plot of figure 7.1 just that the pulse delay is set to be $\tau = T$. The condition for optimum pulse delay is therefore fulfilled and one can see that it is favourable to apply short pulses rather than long pulses to achieve high population values of the final state. Due to decoherence effects that arise during the population transfer shorter pulses are better suited as longer pulses for STIRAP. For this specific example only about 60 % of the initial population is transferred to the final state when the pulse has a width and a delay of of $T = \tau = 50\,\mathrm{ns}$. For longer pulses this value decreases even more and the process becomes very inefficient.

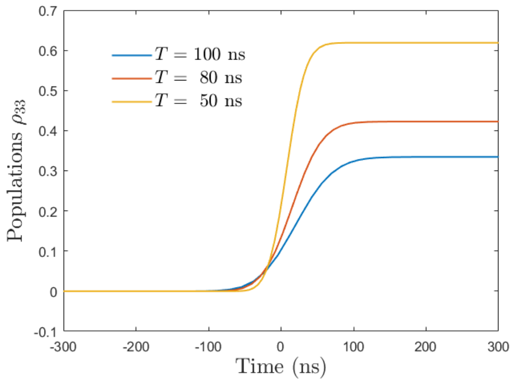

Figure 7.3.: Transfer efficiency for the condition $\tau = T$. Pulse area is set to $A = 10$.

8. Summary and Outlook

The motivation of this thesis is to build and to characterize a laser setup which can be used in a STIRAP process for populating opposite parity states in Dysprosium.
Chapter 2 presented an introduction to stimulated Raman adiabatic passage (STIRAP). STIRAP is an efficient and selective method to transfer the population from an initially populated state to a target state by coupling them with two radiations fields via an intermediate state. The time evolution of such a system is given by the time dependent Schrödinger equation. The instantaneous eigenstates of the Hamiltonian are linear superpositions of the unperturbed states. STIRAP relies on the so called dark state which is a coherent superposition of the initial and target state only. The dark state does not contain the intermediate state, and hence spontaneous emission from this level does not play a role. If it is possible to stay in the dark state during the whole transfer process, then all the population can be transferred from the initial to the target state.
To build a laser with enough power for the STIRAP transition, an enhancement cavity for the second harmonic generation (SHG) process is needed. Chapter 3 deals with the physics of optical resonators. Starting from the basic properties of Gaussian beams, the ABCD-matrix method is developed and the self-consistent method, which implies a confinement condition for optical resonators, are reported. Using a plane wave model, which is applicable for both standing wave resonators and ring cavities, expressions for the circulating and reflected intensities (as a function of the incoming intensity) are motivated. These expressions can be used to derive the so called impeadance-matching condition. This condition basically says that the Transmittance of the cavity's input coupler has to be equal to the losses inside the cavity. Finally, the special case of a bow-tie cavity consisting of two flat and two curved mirrors is discussed.
Chapter 4, probably the biggest topic, is describing the second harmonic generation process. At the beginning some basic terms concerning optics in crystals are reviewed. Then, an introduction to nonlinear optics is given. The process of second harmonic generation without depleted input and with depleted input is examined. In the depleted input case, the second harmonic generated power exhibits a $\sin^2(\delta)$ behaviour where δ describes the phase mismatch. In the case without a depleting input the second harmonic generated power is proportional to $\tanh^2(\kappa A_1(0)z)$, where κ is a factor depending on the crystal properties and $A_1(0)$ can be brought into relation with the electric field amplitude $E_1(0)$ at the position $z = 0$. Next, the Boyd-Kleinman analysis for SHG, which deals with Gaussian beams rather than with plane waves, is introduced briefly. The last section in this chapter combines the SHG process with the resonator optics from the previous chapter.
The setup presented in chapter 5 consists mainly of four parts . The first part is an

external-cavity diode laser (ECDL) in cat's eye design which acts as a light source. The emitted light should have a wavelength of $\lambda_{\mathrm{fund}} = 837.2\,\mathrm{nm}$ with a possibly small bandwidth. The second part of this setup is a tapered amplifier (TPA). The optical power emitted from the ECDL will be amplified by a factor 10 to 100. The part behind the TPA is a bow-tie cavity wit an nonlinear crystal inside. The cavity itself increases the optical power inside up to several Watts. When the light passes through the crystal, the desired wavelength of $\lambda_{\mathrm{SHG}} = 418.6\,\mathrm{nm}$ is generated due to SHG. The last part consists of an AOM in a double-pass configuration and is used for pulse shaping.
Chapter 6 characterizes the entire setup. This is not only important to see if the required goals could be achieved, but also for performance documentation of the setup as a reference for the future. The cat's eye ECDL shows the well known power/current and current/voltage characterisics. By rotating the interference filter the wavelength and the power of emitted from the ECDL can be changed. The TPA shows the expected output power/ TPA current characteristic. By measuring the output power of blue light from the bow-tie cavity a maximum value of $(33 \pm 2)\,\mathrm{mW}$ could be achieved. Looking at the reflected light, it has been determined that only $(55.3 \pm 0.2)\,\%$ of the light is coupled into the cavity due to mode mismatching. The obtained error signal looks qualitatively like the theoretical one and can be used to lock the laser to the cavity. The power inside the cavity is estimated to be $(27 \pm 1)\,\mathrm{mW}$. The double-pass AOM could be realized with a rise time of approximately 30 ns. At the end of the whole apparatus approximately 3 mW of light in the desired wavelength is available.
In chapter 7, based on [12], a simulation has been performed which accounts for the very unequal decay rates from the intermediate state to the inital and target state, respectively. This simulation should help to find the right settings for the pulse duration as well as for the pulse delay in the STIRAP process. Due to coherence effects pulses in the range of 100 ns are preferred.

The next step would be to test this laser setup on the Dysprosium atoms and doing spectroscopy. Once the state positioned at $23\,877.75\,\mathrm{cm}^{-1}$ has been found the second STIRAP branch can be engineered. For the second branch one may use an extended cavity diode laser using a standard optical diode centered at 1625 nm. Both lasers need to be phase locked to a high finesse ultra low expansion cavity in vacuum using Pound-Drever-Hall technique to ensure frequency noise on a kHz level. After the desired opposite parity state is populated, one then reverses the STIRAP in order to image the atoms in the ground state using standard absorption imaging. Once the STIRAP populates efficiently the opposite parity state which requires the two lasers to be in σ^+ and π configuration, a π-microwave pulse is driven to mix it with the other opposite parity state. The microwave source will be a phase-locked loop based on a VCO, operating in the range up to 10 GHz locked to a 10 MHz reference, doubled and amplified in two stages. Once the opposite parity states are mixed, the simplest manner of the dipole-dipole interaction (DDI), namely the expansion dynamics of a bosonic sample or the deformation of the Fermi surface due to DDI can be diagnosed.

Appendices

A. Tapered vs non-tapered Amplifiers

It is very difficult to obtain high output powers in the range of 1 W or more from ordinary laser diodes. Output powers of ≈ 100 mW can damage the small output facets of laser diodes. One of the best solutions to get higher output powers with a narrow frequency spectrum is to use semiconductor traveling wave amplifiers with a tapered geometry. The equation of such a travelling wave amplifier in terms of power P is given by

$$\frac{dP}{dz} = \left(\frac{g_0}{1 + \frac{P}{P_{s0}(1+k_t z)}} - a\right)P. \tag{A.1}$$

In equation (A.1) P_{s0} is known as saturation power at the input end ($z = 0$), k_t (taper ratio) describes the tapered geometry, g_0 is called unsaturated gain and a is the absorption coefficient due to losses in the active medium. For a detailed derivation consider [21]. To see the behaviour of the tapered gain region, equation (A.1) can easily be integrated with MatLab. The solution is shown in figure A.1.

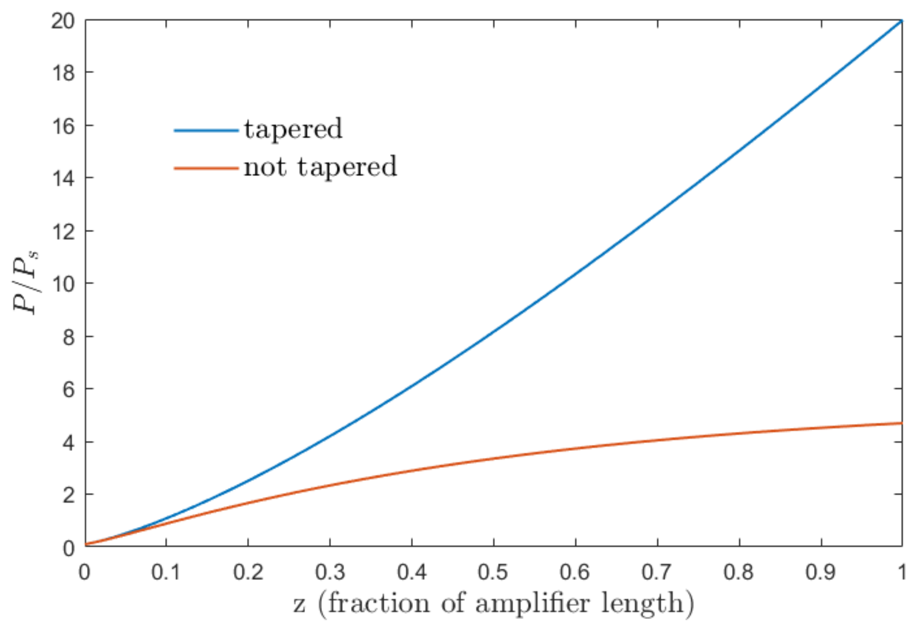

Figure A.1.: Power as a function position in a tapered and a non-tapered amplifier with the following parameters: $g_0/a = 56$, $k_t = 5$ and input = 0.1 $\mathrm{P_S}$, $\mathrm{P_S}$ being the saturating power at the amplifier input. Figure created according to [21].

B. Electronic Circuits

B.1. Advanced Laser PID

For most experiments in atomic physics a frequency stabilized laser beam is required. The frequency stability is disturbed by various influences such as temperature change, vibration, sound, noise from the laser diode, etc. and must therefore be stabilized by a control loop. The used control electronics is rather complicated and unfortunately no circuit description exists. To make the life of a future master student easier it is tried to describe the circuit here in greater detail.
The HC method is used for frequency stabilization. The difference signal from two photo diodes, which are illuminated from a polarization beam splitter, serves as the measurement variable. The difference signal of the two photodiodes is guided and amplified via a $50\,\Omega$ coaxial cable to the controller circuit boards (frontboard and mainboard V5.4 PID fast). The desired value of the difference signal of the two photo diodes is $0\,\mathrm{V}$. In this case the intensities of the horizontal and vertical polarization directions are equal. For interference signals with low frequencies, the difference signal is amplified by a PI controller and transformed by a DC-DC converter from the +/- 12 V voltage range to a range of +/- 150 V. This relatively high voltage controls a mirror position in the bow-tie resonator by means of a piezo electric tranducer. As a result, the phase position in the resonator is kept constant within a free spectral range. For interference signals with high frequencies, the difference signal is amplified by a fast PID controller and thus regulates the frequency of a laser diode.
To work with the control electronics it is essential to know what the operating elements are doing. Therefore, a detailed description of the operating elements and plug connections follows now. Mainboard and Frontboard circuit diagrams are shown in figures **??** and **??**, respectively.
Switch-S3 Mainboard - Fast PID Prop On/Off There are two different names for the switch S3, "PID off" and "PID IO", of the signal line. The switch itself is mounted on the front plate, but is defined in the "Mainboard" circuit diagram. The electronic switch "U13" is controlled with the signal line. If the signal line "PID off" for "S3" is connected to + 5V, then the connection between pin 1 and pin 8 is conductive and the PID-Fast signal is sent to the BNC connector via OPA "U14" P4 forwarded. If the "PID off" signal line on "S3" is connected to GND, the connection between Pin-1 and Pin-8 is non-conductive and the PID-Fast signal is interrupted.

S5 Mainboard - Fast PID Int On / Off There are also two different names for the S5 switch, "I-fast" and "I-fast IO", on the signal line. The switch itself is mounted on the

Figure B.1.: Laser PID advanced.

front plate, but is defined in the "Mainboard" circuit diagram. The electronic switches "U11" and "U12" are controlled with the signal line "I-fast". If the signal line "I-fast" on the switch "S5" is connected to GND, then the connections between pin 1 and pin 8 of the IC's "U11" and "U12" are non-conductive. OPA "U2" and OPA "U3" work as P and I control loop amplifiers. If the signal line "I-fast" is connected to + 5V, the capacitor "C16" and the resistor "R26" connected to the OPA "U2" are bridged. Regarding the OPA "U3", capacitors "C9" to "C15" and the resistor "R22" are bridged. Now the P-loop amplifier has a lower gain and a smaller time constant, the ID-loop amplifier is now only a D-loop amplifier. The PID controller now has a lower gain and only the fast-reacting D component.

Error Signal - P9 Frontboard The "Error Signal" represents the difference between the two diode signals at the "BNC" plugs "P2" and "P3". When the control circuit is steady, the "Error Signal" should show approximately 0 V and over 50 Ω it can be measured on the oscilloscope.

-Input - P2 Frontboard Diode input signal D1 at the "BNC" connector "P2".

+Input - P3 Frontboard Diode input signal D2 at the "BNC" connector "P3".

Offset - R18 frontboard The potentiometer "R18" enables an effective offset voltage of +/- 12.5 mV via the OPA "U10". The potentiometer "R62" can theoretically reduce the effectiveness of the offset, but only in the range of approximately +/- 0.25 mV. The relationship $U_{\text{offset}} = UD2 - R37 \cdot (UD2 - U10)/(R37 + R40 + R69 + R62)$ and $U10 = +/-5V \cdot R13/(R13 + R19)$ applies to the offset voltage.

PiezoProp On / Off - S1 mainboard The switch mounted on the front panel, designated "S1" in the "Mainboard" circuit diagram, is designated as a signal with "I-slow IO". It bridges the capacitors "C12" and "C42" of the I-controller when the switch "S1" is closed. This situation corresponds to the position "PiezoProp Off". The capacitor "C12" also bridges the "R54" resistor on the "Frontboard" circuit diagram. The outputs of the OPA's "U5A", "U5B" and "U5C" are at GND potential and the influence on the adding OPA "U6" is prevented. In the "Prop On" position, switch "S1" is open, the OPA's "U5A" and "U5B" form a PI controller. The OPA "U5C" is required in order the phase shift matches the OPA "U5D".

PiezoInt On/Off - S4 Mainboard The switch mounted on the front panel, designated "S4" in the "Mainboard" circuit diagram, is referred to as a signal with "P-slow IO". It bridges capacitor "C41" and capacitors"C80" and "C25" to "C31" on the "Frontboard" circuit diagram when the switch is closed. This corresponds to the "PiezoInt Off" position. The output of the OPA "U5D" is then at GND potential, the influence on the adding OPA "U6" is prevented. In the "PiezoInt On" position, switch "S4" is open, the OPA "U5D" is a pure I controller.

LED Power +/- 5V LED D8 / D9 light up if +/- 5V are present.

Piezo Out - P7 frontboard "P7" is the output from the summing amplifier "U6" which is supplied by the PI controllers or by the delta voltage generator and is to be connected to the DC-DC converter so that a mirror of the resonator can then be adjusted with a piezo electric transducer.

Piezo Out-Inverted - S5 Frontboard The connector to the switch "S5" is located in the circuit diagram "Frontboard" and changes the phase of the "Piezo Out" signal by 180 deg with the help of the OPA "U6".

Piezo Out Attenu - R57 Frontboard Resistor "R57" is located in the "Frontboard" circuit diagram next to connector "P7" and can weaken the output signal of OPA "U6" in the "Mainboard" circuit diagram and is forwarded to the front board as a "Piezo out" signal.

Piezo Out Gain - R48 Frontboard Resistor "R48" is located on the "Frontboard" circuit diagram at the output of inverter OPA "U6" and can weaken the output signal of OPV "U6" in the "Frontboard" circuit diagram and is forwarded to the P and I controller in the "Mainboard" circuit diagram.

Piezo Out Prop - R54 Frontboard The resistor "R54" is on the "Frontboard" circuit diagram, but is part of the wiring of the OPA "U5A". The OPA "U5A" is the P amplifier of the PI controller in the "Mainboard" circuit diagram.

Piezo Offset - R56 Frontboard The resistor ”R56” is located on the ”Frontboard” circuit diagram and acts as an adjustable voltage divider between the voltages + Uref and –Uref which are equal to ± 5 V. With the resistor ”R56” the output of the OPA ”U5” can be trimmed to 0 V and is therefore probably called ”Piezo Offset”.

Piezo Monitor - P6 Frontboard Oscilloscope connection for measuring the voltage which is proportional to the voltage at the HC-DCDC converter. Together with connection ”P9” and connection ”P8” = Sweep Trigger Out, the free spectral range of the resonator can be measured.

Piezo Monitor BW Int - S4 Frontboard ”S4”is a series of switches with which the capacitors ”C8 ”and ”C25” to”C31” can be connected in parallel to ”C41”. The capacitor ”C41” is on the circuit diagram ”Mainboard”, ”C8” and ”C25” to ”C31” are on the circuit diagram ”Frontboard”. If all switches ”S4” are open, only ”C41” is effective. The capacitance value decreases from left to right. The capacitors act as integrator capacitance on the I-controller OPA ”U5D”.

Fast PID Gain D sec - R17 Frontboard The resistor ”R17” is located on the ”Frontboard” circuit diagram and is an adjustable resistor. Together with the resistor ”R15”, ”R17” is connected in series with the capacitors of the D controller and determines the effect of the D component of the PID controller. The smaller the set value of R17, the greater the effect of the D component.

Fast PID Gain I sec - R22 Frontboard The resistor ”R22” is located on the ”Frontboard” circuit diagram and is an adjustable resistor. Together with the resistor ”R26”, ”R22” determines the static amplification of the OPA ”U3”, i.e. the DI controller, to a range from 0.1 to 10 (essentially limited by the resistors ”R25” and ”R29”).

Fast PID Attenuation - R31 Frontboard The resistor ”R31” is located on the ”Frontboard” circuit diagram at the output of the ”Fast PID controller” and is an adjustable resistor with which the gain of the PID controller can be weakened.

Fast PID Offset - R72 Frontboard The resistor ”R72” is located on the ”Frontboard” circuit diagram and is used to compensate for the offset of the ”U14” OPA. The setting range is 0 V to +20 V, based on the output of ”U14”.

Fast PID Attenu DC - S1 Frontboard The series of switches ”S1” is located on the ”Frontboard” circuit diagram and is used to digitally set the attenuation of the photodiode difference signal from the OPA ”U1”. The switch ”S1-1/16” is on the far left and makes the largest contribution from the input signal, the switches further to the right make increasingly smaller contributions. When all switches are closed, the attenuation is lowest.

Fast PID AC BW Diff - S2 Frontboard The series of switches ”S2” is located on the

"Frontboard" circuit diagram and is used to digitally set the capacitor value of the D controller. The switch "S2-1/16" is on the far left and brings the largest contribution ("C8" = 1 nF), the switch "S2-8/9", on the far right brings the smallest contribution ("C1" = 4.7 pF).

Fast PID AC BW Int - S3 Frontboard The series of switches "S3" is located on the "Frontboard" circuit diagram and is used to digitally set the capacitor value of the I controller. The switch "S3-1/16" is on the far left and brings the largest contribution ("C15" = 22 nF), the switch "S3-8/9", on the far right brings the smallest contribution ("C9" = 220 pF).

LED D3 - D3 Frontboard The LED "D3" is located on the "Frontboard" circuit diagram and lights up when the voltage at "P5" is greater than approximately 2 V.

Sweep On/Off - S2 Mainboard The switch "S2" is located in the"Mainboard" circuit diagram. In the "Sweep Off" position, the capacitor "C28" of the integrator "U12B" is bridged with a resistor, thereby preventing the generation of the triangular voltage. In addition,"R14" and "R10" are connected to GND, which enables the AND operation of the output signals from "Sweep", "U5D" and "P3 Second Int". The triangular voltage generator is used to search for the "free spectral range" in the bow-tie resonator.

Sweep Amplitude - R10 Mainboard The potentiometer "R10" is located on the "Frontboard" circuit diagram and is used to weaken the amplitude of the triangular voltage if the piezo actuator hub allows too many resonance frequencies. The setting range is from 0 % to 100 %.

Fast PID Monitor - P5 Frontboard Oscilloscope connection for monitoring the Fast PID controller output. The LED "D3" lights up when the voltage at "P5" is greater than approximately 2 V.

Fast PID out - P4 Frontboard The output of the Fast PID controller "P4" may need to be connected to the current modulation input on the laser to reduce fast phase modulations.

B.2. HV-DCDC Converter

The used high voltage (HV) DCDC-converter is a crucial element for locking the laser to the cavity. By changing the position of the potentiometer "R15" and hence the voltge in figure **??**, an offset up to 150 V can be adjusted. The BNC output "P7" (Piezo-Out) from the advanced laser PID circuit (**??**) is connected to the modulation input of the HV-DCDC converter "P3A". The HV-DCDC output "P3B" is then connected to the piezo electric actuator of the bow-tie cavity to close the feedback loop.

C. AOM Rise Time Equation

The rise time is defined as the time the first order diffraction needs to rise from 10 % to 90 % of it's maximum and is given by

$$t_{\mathrm{R}} = 0.65 \frac{d}{v_{\mathrm{S}}} \tag{C.1}$$

where d is the 1/e^2 beam diameter and v_{S} is the speed of sound in the acousto-optic medium. It is not immediately apparent where the prefactor of 0.65 comes from. Equation C.1 is only valid for a Gaussian beam in the TEM$_{00}$ mode. The intensity distribution of such a beam propagating in z-direction is given by

$$I(r,z) = I_0 \left(\frac{w(z)}{w_0}\right)^2 e^{\frac{-2r^2}{w(z)^2}} \tag{C.2}$$

where $w(z)$ is the 1/e radius according to equation (3.4), $w(z=0) = w_0$ is the waist or minimum spot size and $r = \sqrt{x^2+y^2}$ is the radial distance measured from the intensity maximum. I_0 is the maximum intensity located at $x = 0$ and $y = 0$. When the AOM is switched on, the sound wave is propagating through the optical beam such that, at the beginning not the whole optical beam gets diffracted. This situation is equivalent by cutting the beam in one direction (here we chose x-direction) and measuring the remaining power. By choosing $z = 0$ and integrating equation (C.2) one obtains

$$\begin{aligned} P(x') &= \int_{-\infty}^{x'} \int_{-\infty}^{+\infty} e^{\frac{-2(x^2+y^2)}{w_0^2}} dxdy \\ &= I_0 \frac{w_0^2}{2} \int_{-\infty}^{\frac{\sqrt{2}x'}{w_0}} e^{-\tilde{x}^2} d\tilde{x} \int_{-\infty}^{+\infty} e^{-\tilde{y}^2} d\tilde{y} \\ &= \frac{P_0}{2} \left[1 + \mathrm{erf}\left(\frac{\sqrt{2}\mathrm{x}'}{\mathrm{w}_0}\right)\right] \end{aligned} \tag{C.3}$$

where x' is the starting point where the beam is cut. In equation (C.3) the substitutions $\frac{\sqrt{2}x}{w_0} = \tilde{x}$ and $\frac{\sqrt{2}y}{w_0} = \tilde{y}$ and the relationship $I_0 = \frac{2P_0}{\pi w_0^2}$ with P_0 as the total power are used. erf(x) is the well known error function. The relationship between I_0 and P_0 can easily be obtained by integrating equation (C.2) from $-\infty$ to $+\infty$ instead to a specific $x = x'$.

Considering now the final result of equation (C.3), 10 % of the total power P_0 are measured when the beam is cut at x_1' = -0.65 w_0 and 90 % for cutting the beam at x_1' = +0.65 w_0. Equation (C.1) deals with the diameter of the beam which explains the appearance of the prefactor 0.65. The situation is shown graphically in figure C.1.

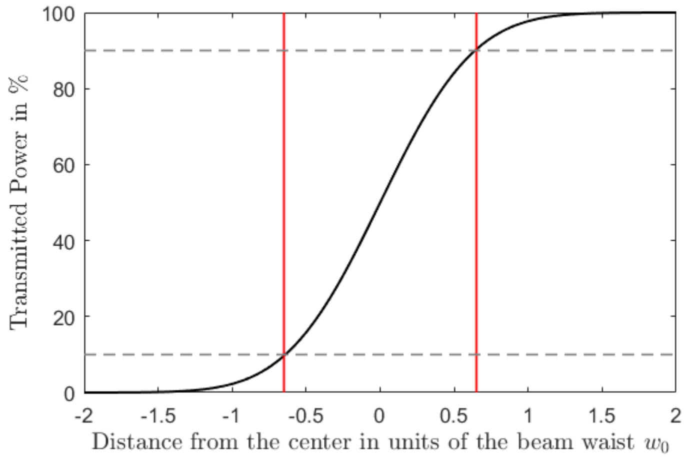

Figure C.1.: Measured power when cutting a Gaussian beam located at $x = 0$ and $y = 0$ along the x-direction. Black curve shows equation (C.3). Red vertical lines correspond to $\pm$ 0.65 w_0 cutting positions. Grey horizontal dashed lines indicate 10 % and 90 % thresholds of the transmitted power.

Bibliography

[1] M. A. Baranov, M. Dalmonte, G. Pupillo, and P. Zoller. Condensed Matter Theory of Dipolar Quantum Gases. *Chem. Rev.*, 112, 9, 2012.

[2] A. Griesmaier, J. Werner, S. Hensler, J. Stuhler, and T. Pfau. Bose-Einstein Condensation of Chromium. *Phys. Rev. Lett.*, 94, 16, 2005.

[3] M. Lu, N. Q. Burdick, S. H. Youn, and B. L. Lev. Strongly Dipolar Bose-Einstein Condensate of Dysprosium. *Phys. Rev. Lett.*, 107, 19, 2011.

[4] K. Aikawa, A. Frisch, M. Mark, S. Baier, A. Rietzler, R. Grimm, and F. Ferlaino. Bose-Einstein Condensation of Erbium. *Phys. Rev. Lett.*, 108, 21, 2012.

[5] M. Lepers, H. Li, J. F. Wyart, G. Quéméner, and O. Dulieu. Ultracold Rare-Earth Magnetic Atoms with an Electric Dipole Moment. *Phys. Rev. Lett.*, 121, 6, 2018.

[6] W. C. Martin, R. Zalubas, and L. Hagan. *Atomic Energy Levels - The Rare-Earth Elements*. National Bureau of Standards, 1978.

[7] J. J. Curry, E. A. Den Hartog, and J. E. Lawler. Radiative lifetimes of Dy I and Dy II. *J. Opt. Soc. Am. B*, 14, 11, 1997.

[8] B. W. Shore. *Manipulating Quantum Structures Using Laser Pulses*. Cambridge University Press, 2011.

[9] U. Gaubatz, P. Rudecki, S. Schiemann, and K. Bergmann. Population transfer between molecular vibrational levels by stimulated Raman scattering with partially overlapping laser fields. A new concept and experimental results. *J. Chem. Phys.*, 92, 9, 1990.

[10] K. Bergmann et al. Roadmap on STIRAP applications. *J. Phys. B: At. Mol. Opt. Phys.*, 52, 20, 2019.

[11] P. A. Ivanov, N. V. Vitanov, and K. Bergmann. Effect of dephasing on stimulated raman adiabatic passage. *Phys. Rev. A*, 70, 6, 2004.

[12] P.A. Ivanov, N. V. Vitanov, and K. Bergmann. Spontaneous emission in stimulated Raman adiabatic passage. *Phys. Rev. A*, 72, 5, 2005.

[13] N. V. Vitanov, A. A. Rangelov, B. W. Shore, and K. Bergmann. Stimulated Raman adiabatic passage in physics, chemistry, and beyond. *Rev. Mod. Phys.*, 89, 1, 2017.

[14] V. I. Romanenko and L. P. Yatsenko. Adiabatic population transfer in the three-level Λ-system: two-photon lineshape. *Opt. Comm.*, 140, 4, 1997.

[15] B. W. Shore. Picturing stimulated Raman adiabatic passage: a STIRAP tutorial. *Adv. Opt. Photonics*, 9, 3, 2017.

[16] K. Bergmann, H. Theuer, and B. W. Shore. Coherent population transfer among quantum states of atoms and molecules. *Rev. Mod. Phys.*, 70, 3, 1998.

[17] B. E. A. Saleh and M. C. Teich. *Fundamentals of Photonics.* John Wiley & Sons Inc, Hoboken, New Jersey, second edition, 2007.

[18] A. E. Siegman. *LASERS.* University Science Books, first edition, 1986.

[19] F. Pedrotti, L. Pedrotti, W. Bausch, and H. Schmidt. *Optik für Ingenieure.* Springer-Verlag Heidelberg, third edition, 2002.

[20] A. Yariv. *QUANTUM ELECTRONICS.* John Wiley & Sons Inc, Hoboken, Inc, third edition, 1989.

[21] W. Nagourney. *Quantum Electronics for Atomic Physics.* Oxford University Press Inc., New York, first edition, 2010.

[22] R. Lechner. Photoionisation of ^{40}Ca with a frequency-doubled 422 nm laser and a 377 nm laser diode. Master's thesis, University of Innsbruck, 2010.

[23] G. S. Monk. *LIGHT: Principles and Experiments.* McGRAW-HILL BOOK COMPANY, first edition, 1937.

[24] D. Meschede. *Optics, Light, and Lasers.* Wiley-VCH, first edition, 2017.

[25] P. E. Powers and J. W. Haus. *Fundamentals of Nonlinear Optics.* CRC Press, second edition, 2017.

[26] T. Pascal, A. Usman, and J. C. Ododo. The phenomenon of nonlinear optical birefringence in uniaxial crystals. *Lat. Am. J. Phys. Educ.*, 5, 2011.

[27] A. Yariv and P. Yeh. *Optical Waves in Crystals.* John Wiley & Sons, first edition, 1984.

[28] R. W. Boyd. *Nonlinear Optics.* Elsevier Science Publishing Co Inc, third edition, 2008.

[29] W. P. Risk, T. R. Gosnell, and A. V. Nurmikko. *Compact Blue-Green Lasers.* Cambridge University Press, first edition, 2003.

[30] Y. Chen and Y. Chen. Analytical functions for the optimization of second-harmonic generation and parametric generation by focused gaussian beams. *Appl. Phys. B*, 76, 6, 2003.

[31] M. Pizzocaro, D. Calonico, P. C. Pastor, J. Catani, G. A. Costanzo, F. Levi, and L. Lorini. Efficient Frequency Doubling at 399 nm. *Appl. Opt.*, 53, 16, 2014.

[32] Z. J. J. Ou. *Quantum Optics for Experimentalists*. World Scientific Publishin g Co. Pte. Ltd., third edition, 2017.

[33] T. W. Hänsch and B. Couillaud. Laser Frequency Stabilization by Polarization Spectroscopy of a Reflecting Reference Cavity. *Opt. Comm.*, 35, 3, 1980.

[34] X. Baillard, A. Gauguet, S. Bize, P. Lemonde, Ph. Laurent, A. Clairon, and P. Rosenbusch. Interference-filter-stabilized external-cavity diode lasers. *Opt. Comm.*, 166, 2, 2006.

[35] Daniel J. Thompson and Robert E. Scholten. Narrow linewidth tunable external cavity diode laser using wide bandwidth filter. *Rev. Sci. Instrum.*, 83, 2, 2012.

[36] eagleyard Photonics GmbH. *DATA SHEET: EYP-RWE-0840-06010-1500-SOT02-0000*, 01 2018. Rev. 1.10.

[37] M. F. Jamal, H. A. Faisal, and M. A. Shireen. Ultra-Narrow Bandpass Interference Filter for Infrared Application. *Int. J. Emerg. Trends Sci. Technol.*, 5, 2, 2016.

[38] CVI LASER OPTICS. *Interference Filter Coatings - CVI Melles Griot Technical Guide*.

[39] Radiant dyes lasers acc. gmbh. https://radiant-dyes.com/index.php/products/laser/diode-laser/187-interference-filter%20data%20sheet.

[40] Layertec gmbh: Datasheet - output coupler 108216. https://www.layertec.de/en/shop/datasheet-108216/?cur=USD.

[41] Matthias Scholl. Laboratory rebort: Interference filter stabilized external cavity diode laser, 2018.

[42] J. N. Walpole. Semiconductor amplifiers and lasers with tapered gain regions. *Opt. Quant. Electron.*, 28, 1996.

[43] E. A. Donley, T. P. Heavner, F. Levi, M. O. Tataw, and S. R. Jefferts. Double-pass acousto-optic modulator system. *Rev. Sci. Instrum.*, 76, 6, 2005.

[44] Australia University St, Carlton VIC 3053. *External Cavity Diode Laser: CEL and CEF Cateye*. MOG Laboratories Pty Ltd, 2019.

[45] Internal communication with Maxence Lepers.